University of Nottingham
UK | CHINA | MALAYSIA

Graphene grown on hBN by MBE and the deposition of hexacontane on hBN

Juan Diez Albar

Supervised by Professor Peter H. Beton

Thesis submitted to the University of Nottingham
for the degree of Doctor of Philosophy

October 2019

Abstract

This thesis discusses the growth of graphene on hexagonal boron nitride (hBN) by high temperature molecular beam epitaxy (MBE) with three different carbon sources: a carbon filament, an atomic carbon source consisting of a thin Ta cylinder and an e-beam source. The flakes were transferred into sapphire wafers previously to graphene growth in order to serve as a refractory support. Graphene layers grown with the different sources present common features but also significant differences which are discussed.

Full graphene monolayers are investigated using atomic force microscopy (AFM), Raman spectroscopy, X-ray photoelectron spectroscopy (XPS) and conductive AFM. Samples exhibit hexagonal Moiré patterns with periods that tend to increase with the substrate growth temperature from ~14 nm, corresponding to rotationally aligned graphene on hBN, to much larger periods ~75 nm. Shifted Raman peaks, obtained from these areas indicate that the graphene is under tensile strain.

Moreover, at the highest temperatures ~1700 ºC, we observe domains where graphene and hBN are lattice matched and the hexagonal boundaries of the Moiré patterns become Frenkel-Kontorova walls that run along principal crystal axes and terminate at lattice defects. Previous theoretical studies indicate that graphene lattice matched to hBN exhibits a small ~50 mV gap due to inversion symmetry breaking of the two atoms in the unit cell of graphene. Conductive AFM measurements obtained at these Frenkel-Kontorova walls and at the areas between them, which we presume are lattice matched, show a lower conductance at the latter compared to the former which is consistent with the opening of a small bandgap.

These results represent new approaches to the introduction of strain in graphene as well as the possibility of local modification of its electronic properties which may be useful for the fabrication of graphene devices.

The deposition of hexacontane ($C_{60}H_{122}$) on hBN is also studied in chapter 7. We observed lamellar structures similar to that formed by alkanes on graphite. The orientation of the molecule with respect to the hBN lattice was also studied by obtaining high resolution AFM images and computer simulations.

List of publications

- **Juan D. Albar**, A. Summerfield, T. S. Cheng, A. Davies, E. F. Smith, A. N. Khlobystov, C. J. Mellor, T. Taniguchi, K. Watanabe, C. T. Foxon, L. Eaves, P. H. Beton and S. V. Novikov. "*An atomic carbon source for high temperature molecular beam epitaxy of graphene*". Scientific Reports, 7, 6598 (2017)
- Andrew Davies, **Juan D. Albar**, Alex Summerfield, James C. Thomas, Tin S. Cheng, Vladimir V. Korolkov, Emily Stapleton, James Wrigley, Nathan L. Goodey, Christopher J. Mellor, Andrei N. Khlobystov, Kenji Watanabe, Takashi Taniguchi, C. Thomas Foxon, Laurence Eaves, Sergei V. Novikov and Peter H. Beton. "*Lattice-Matched Epitaxial Graphene Grown on Boron Nitride*". Nano Lett. (2018), 18, 498-504
- **Juan D. Albar**, Vladimir V. Korolkov, Matteo Baldoni, Kenji Watanabe, Takashi Taniguchi, Elena Besley and Peter H. Beton. "*Adsorption of Hexacontane on Hexagonal Boron Nitride*". J. Phys. Chem. C 2018, 122, 27575−27581.
- **Juan D. Albar**, Mariano D. Jiménez-Sánchez and José M. Gómez-Rodríguez. "*Nanowriting with Clusters on Graphene on Ru(0001)*". J. Phys. Chem. C 2019, 123,9, 5525-5530.

Acknowledgements

Writing this thesis is probably the most difficult endeavour that I have ever attempted. I would like to mention the people that helped me over these last four years.

Firstly, I would like to thank my supervisor Professor Peter Beton for giving me the opportunity to pursue a PhD in this amazing and beautiful field that is nanoscience. His support, guidance and otherworldly patience were key in the developing of this thesis.

Thanks to the following colleagues for their guidance, their contribution to the discoveries we made through these years or for just listening and cheering me up when things got difficult: Professor Sergei Novikov, Dr Tin Cheng, Dr Alex Summerfield, Dr James Kerfoot, Dr Simon Svatek, Dr Vladimir Korolkov, Dr Abigail Browning, Manal Alkhamisi, James Thomas, James Wrigley, Dr Andrew Davies, Dr Jake Greener, Professor Amalia Patane, Professor Laurence Eaves, Professor Tom Foxon, Professor Christopher Mellor, Dr Manon Bourbousson, Dr Zakhar Kudrynskyi, Dr Mahabub Bhuiyan and Dr Deborah Varley. I will always remember you as well as the experiences we had.

Thanks to the Engineering and Physical Sciences Research Council for funding my PhD.

I would also like to thank my family for their support, specially to my mother Isabel and my brother Javier.

Professor José Maria Gómez, Dr Ana Martín-Recio, Dr Bruno De La Torre and Mariano Jiménez from the módulo 3 at the Universidad Autónoma de Madrid also deserve their recognition considering that they helped me during my first steps in science research.

Finally, thank you Araceli for your love and patience during these long months. I feel very fortunate to have you in my life. I will make it up to you as soon as I can.

Contents

1. Introduction

1.1 Introduction

In 2004, Geim and Novoselov isolated and identified graphene for the first time using a tape exfoliation process[1]. Subsequently performed transport measurements on this material. Since then, the remarkable properties[2] and potential applications of graphene have attracted much interest[3]. Examples of interesting phenomena that have been studied in graphene are: ambipolar field effect[1]; room temperature Quantum Hall effect[4,5] ; Klein tunneling[6]. Also, the one atom thickness of graphene allows its electronic properties to be modified through the interaction with molecules[7,8] or other crystals on which graphene can be deposited or grown. For example, a gate electrode can be used to shift up or down the Fermi level[1] or growth on Ni can disrupt the Dirac cones opening a band gap[9]. In addition, graphene has stimulated interest in the study of other 2D materials and the heterostructures that can be formed by stacking these crystals[10]. Previous to the work by Geim and Novoselov, Landau and Peierls had argued that 2D crystals were thermodynamically unstable at any finite temperatures[11,12].

In this section, the most widely used fabrication techniques of graphene are discussed. A significant effort has been made in developing high quality large scale synthetic methods to grow graphene[13,14] as required for industrial applications. These methods can be grouped into two main categories: top-down approaches and bottom-up approaches. In general, the top down approaches consist of separating layers of graphene from the bulk of graphite by overcoming the van-der-Waals forces that hold them together, while bottom up approaches focus on forming graphene layers from precursor molecules or individual carbon atoms. The most commonly used top down approaches are mechanical exfoliation, electrochemical exfoliation and reduction of graphite oxide. On the other hand, bottom up approaches like SiC annealing, growth from metal-carbon melts and chemical vapour deposition (CVD) are the most common methods to produce large area graphene.

The process of mechanical exfoliation begins by sticking a piece of adhesive tape onto a block of graphite. Careful removal leaves several layers on the tape. By folding and unfolding the tape several times the graphite crystals are split into increasingly thinner flakes. Then the tape is put in contact with a SiO_2/ Si wafer and carefully peeled off. A few layers will stick on the surface where they can be observed with an optical microscope[15]. However, this method is extremely time consuming and is difficult to scale up for industrial production. A variation of this method uses a three roll mill machine with a polymer adhesive[16]. Instead of scotch tape, Polyvinyl chloride (PVC) dissolved in dioctyl phthalate (DOP) is used as the adhesive. The surfaces of the moving rolls are in contact with each other, so exfoliation occurs every time that the flakes pass between rolls. The graphite flakes run in an inverted S curve from the feed roll to the apron roll, then turn back towards the feed roll, leading to continuous exfoliation. The material from the rolls is collected afterwards, submerged in alcohol and introduced in a furnace for 3h at 500 °C in order to remove the adhesive mix. Another variation of mechanical exfoliation is ball milling. This method has been used in particle size reduction for long time. In 2010 Knieke et al.[17] and Zhao et al.[18] applied this technique to produce graphene in carefully selected solvents: de-ionized water and sodium dodecyl sulphate (SDS) in the case of Knieke and N,N-dimethylformamide (DMF) in the case of Zhao. Steel balls are used to exert a shear forces on graphene layers which is consider as an excellent route for exfoliation of large-size graphene flakes. Nevertheless, normal impacts applied by the balls can result in fragmentation of large flakes which is an undesirable effect that should be minimized.

Electrochemical exfoliation is a more sophisticated process that uses ionic species to intercalate between graphene layers where they react to form gases that through expansion exfoliate graphene layers. Graphite flakes and platinum wires are introduced into a H_2SO_4 aqueous solution[19]. These play the role of anode, cathode and electrolyte respectively. Then, a positive voltage of 10 V is applied between the graphite flakes and the platinum wire. This bias results in the oxidation of water, producing hydroxyl (OH-) and oxygen radicals (O-) initially at edge sites and grain boundaries of the graphite electrode. Oxidation leads to opening of defective sites or grain boundaries where intercalation of SO_4^{2-} anions occurs. These anions then react to form gaseous SO_2 causing the separation of the layers.

Graphite oxide can be produced from graphite by exposure to strong oxidants. Hummers and Offeman developed the most widely applied synthesis method in 1958[20] by using a mixture of sulfuric acid (H_2SO_4), sodium nitrate ($NaNO_3$) and potassium permanganate ($KMnO_4$). A significant fraction of the sp^2-bonded carbon network of graphite is disrupted forming bonds with hydroxyl groups or participating in epoxide groups[21]. Since graphite oxide is strongly hydrophilic, sonication in water is enough to produce a colloidal suspension. Subsequent reduction can be performed by chemical, thermal or ultraviolet assisted methods[22,23]. Nevertheless, reduced graphene oxide (rGO) contains residual oxygen as well as structural defects which hinder carrier mobility. Full reduction of this layers, which is still a challenge[24], is therefore an essential requirement to retrieve the carrier mobility of pristine graphene.

The growth of graphene on SiC can be achieved by annealing at 1200° C. Due to the higher vapour pressure of silicon compared to carbon, sublimation of Si atoms on the SiC (0001) surface results in a higher concentration of carbon atoms in the surface[25]. Initially, a covalently bound carbon interface layer in the form of a ($6\sqrt{3}$ x $6\sqrt{3}$ R30°) reconstruction is formed[26,27] which serves as a buffer layer for the epitaxial growth of subsequent graphene layers. The number of graphene layers grown onto this reconstruction can be precisely monitored by angle resolved photoemission spectroscopy (ARPES) measurements. The interfacial layer, though responsible for establishing epitaxial order between graphene and the substrate, also generates a strong doping n~ 10^{13} cm^{-2} shifting the Fermi level 420mV above the Dirac point[28,29]. However, the intrinsic n-doping of the pristine graphene layers can be compensated by depositing a molecular overlayer of a p-type dopant like F4-TCNQ [30]. It is also possible to decouple the graphene from this interfacial layer by hydrogen intercalation[31].

Single or multiple graphene layers can be grown from a molten phase of a metal. A piece of graphite or powder is added to molten metal like nickel, copper or silver[32,33]. This results in dissolution and saturation of carbon atoms in the melt. Then the temperature is lowered which decreases the solubility of carbon. The excess amount of carbon then precipitates on top of the melt. The floating layer can be skimmed or removed after cooling by etching the metal. The sizes and thicknesses of graphene

layers formed can be roughly tuned by adjusting the times of dissolution and carbon formation.

Graphene grown by CVD was first reported on Ni and Cu substrates[34–38] . Soon after, the use of this technique was applied to a variety of metal substrates[39–43]. The properties of graphene can be altered depending on the strength of the interaction with these substrates[44]. In the CVD process gaseous hydrocarbon species like ethylene or methane are introduced into a chamber where they decompose into carbon radicals by catalytic action of the metal substrate at temperatures ~1000 °C. Depending on the solubility of carbon in the substrate, the radicals may be absorbed into the crystal and segregate later towards the surface when the temperature is lowered, as it is the case for Ni. Due to this process, multiple layers are typically formed on Ni. Also, since Ni (111) has a hexagonal structure with a similar lattice constant to graphene, the two crystals are lattice matched. On the other hand, Cu has a low solubility of carbon, so the carbon radicals remain mostly in the surface. Therefore, after the first graphene layer is formed, covering the Cu surface, there is no catalyst exposed to decompose the hydrocarbons. This means that in this case, the growth is self-limiting, which allows an easier growth of large areas of single layer graphene. In addition graphene on Cu (111) forms multiple oriented Moiré patterns with different misorientation angles indicating that graphene on Cu (111) is a weakly bound system.

In recent years Molecular beam epitaxy (MBE) has emerged as promising alternative for wafer-scale production of graphene since it provides exact deposition rates and a high control on the stoichiometry of the species involved. In addition, MBE does not require the use of catalytic surfaces, which allows direct growth on a dielectric substrate. The growth of graphene on hexagonal Boron Nitride (hBN) appears particularly desirable given that hBN can act as a featureless dielectric substrate which is useful in the study of the intrinsic physics of graphene, or under certain circumstances can modify its mechanical and electronical properties. These heterostructures are discussed with more detail in the section 2.3: Graphene on hBN heterostructures.

1.2 Overview

Large area MBE growth of graphene on hBN had not been demonstrated until the graphene Nottingham group started exploring growth temperatures above 1500ºC. Their earlier results showed complete coverage graphene layers with ~14 nm Moiré patterns as previously observed by CVD. Moreover, in some cases graphene layers displayed Moiré patterns of ~25 nm correspondent to tensile stresses up to 0.8% which could be relaxed post growth raising the possibility of using hBN to control the strain on graphene.

This thesis investigates further the growth of graphene on hBN flakes on Sapphire by MBE at temperatures up to ~1800ºC and provides evidence of the presence of tensile stresses up to 1.8% in graphene. This enables both lattices to match and open a small band gap in the electronic structure of graphene due to the inversion symmetry breaking.

Samples were characterized with AFM although other techniques as Raman spectroscopy or X-ray photoelectron spectroscopy (XPS) provide additional evidence. Different carbon sources were used generating subtle differences between the layers observed. The results are organized by growth sources starting with a filament source in chapter 4 and following with an atomic carbon source and an e-beam source in chapters 5 and 6 respectively.

The deposition of hexacontane, a long chain alkane, on hBN was also studied and is included in chapter 7. In principle we considered hexacontane as a good candidate for its use as protective layer during the transfer process of the hBN flakes covered in graphene from Sapphire to SiO_2. The use of Sapphire wafers as support material is required given the high substrate temperatures used during MBE growth. Unfortunately, this approach was not successful, and we focused on studying the deposition of this molecule on hBN with AFM which had not been done previously. Our images indicate that the molecules are oriented in parallel to the zig-zag direction with their molecular axis parallel to the surface. We also describe other phenomena as de-wetting of the molecules by applying heat post deposition or switching of the molecules orientation during AFM scan.

2. Background

2.1 Electronic structure of graphene

Graphene is a two-dimensional sheet of carbon atoms arranged in a honeycomb structure, with two atoms in a rhomboid unit cell (Fig 2.1). It can be considered as an atomic plane extracted from graphene, as an infinite radius fullerene or as an unrolled nanotube.

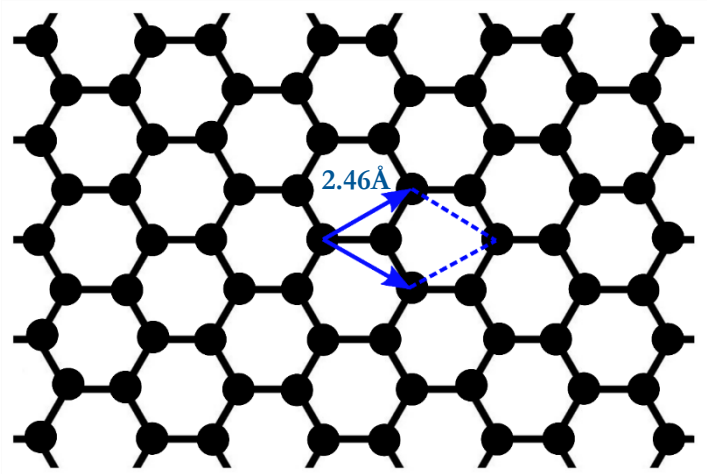

Figure 2.1: Top view of graphene crystal structure. The unit cell vectors are is indicated by the blue arrows. Lattice constant is 2.46Å.

Each carbon atom is covalently bound with three nearest neighbours through σ bonds formed by sp^2hybridized orbitals, separated by a distance of 1.42 Å. These bonds are extremely strong giving graphene remarkable structural properties such as a Young modulus of ~1 TPa[45] or the capability of sustaining reversible tensile strains up to 25% while silicon typically breaks at 1.5%. The orientations of these orbitals are mirror imaged between the two atoms in the unit cell. This means that the two atoms in the unit cell belong to two different hexagonal sublattices A and B.

Carbon atoms, which contain six electrons in the following electron configuration: $(1s)^2(2s)^2(2p)^2$ have two unpaired electrons in the outer 2p shell, but the energy difference between the 2s and the 2p states is sufficiently small to allow an additional electron to be excited from the 2s into the 2p shell. Hybrid states, consisting of a superposition of s and p orbitals can then be formed with energies between the 2s and

the 2p states. A different number of hybrid orbitals can be formed. For example, in diamond carbon forms 4 hybrid orbitals by using one s and three p orbitals, p_x, p_y and p_z. These are sp^3 orbitals and have 25% s and 75% p character. These four orbitals form covalent bonds with four neighbouring atoms allowing carbon to fill its outer shell. In contrast, carbon forms two sp orbitals in acetylene (C_2H_2), with 50% s and 50% p character. One of these hybrid orbitals forms a covalent bond with hydrogen while the other forms another covalent bond with the other carbon atom. The remaining 2p orbitals form two additional covalent π bonds. In the case of graphene or graphite, three sp^2orbitals are formed, from one s, one p_x and one p_y orbitals with 33% s and 66% p character. On the other hand, on each atom, an unhybridized half filled p_z orbital extends perpendicularly to the plane of atoms, overlapping with the p_z orbitals of the three neighbouring atoms. This delocalized orbital forms the π bands which give graphene its interesting electronic properties.

The electronic structure of graphene, was described by Wallace in 1947 using a tight binding model[46]. At that time, his studies of graphene were solely a starting point to study the electronic properties of graphite given that graphene was considered a thermodynamically unstable material.

From the unit cell vectors in real space we can obtain the Brillouin zone in k space using the relationships:

$$\boldsymbol{b_1} = 2\pi \frac{\boldsymbol{a_2}\times\boldsymbol{n}}{\boldsymbol{a_1}\cdot(\boldsymbol{a_2}\times\boldsymbol{n})} \quad ; \quad \boldsymbol{b_2} = 2\pi \frac{\boldsymbol{n}\times\boldsymbol{a_1}}{\boldsymbol{a_2}\cdot(\boldsymbol{n}\times\boldsymbol{a_1})}$$

where $\boldsymbol{a_1}$ and $\boldsymbol{a_2}$ are the unit cell vectors of graphene and $\boldsymbol{n}$ is a unit vector perpendicular to the graphene plane. With these two vectors we can construct the Brillouin zone of graphene, shown in Fig 2.2.

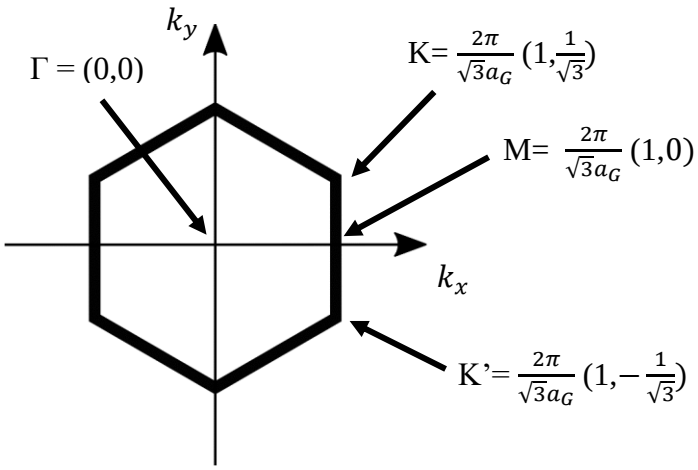

Figure 2.2: Brillouin zone of graphene, showing the main symmetry points.

Graphene has two-atoms in its unit cell so the wave-function has to be represented as a linear combination of two wavefunctions, $u_A(\boldsymbol{k},\boldsymbol{r})$ and $u_B(\boldsymbol{k},\boldsymbol{r})$, corresponding to sublattices A and B with amplitudes represented respectively by the $A(\boldsymbol{k})$ and $B(\boldsymbol{k})$ coefficients:

$$\Psi_k(\boldsymbol{r}) = A(\boldsymbol{k})u_A(\boldsymbol{k},\boldsymbol{r}) + B(\boldsymbol{k})u_B(\boldsymbol{k},\boldsymbol{r}) \qquad (2.1)$$

The wave functions corresponding to each of the two sublattices, are in turn composed by a superposition of atomic wave functions φ_A and φ_B, centred on atoms belonging respectively to the A and B sublattices:

$$u_A(\boldsymbol{k},\boldsymbol{r}) = \frac{1}{\sqrt{N}}\sum_{i=1}^{N} e^{i\boldsymbol{k}\boldsymbol{R_i}}\,\varphi_A(\boldsymbol{r}-\boldsymbol{R}_i)$$

$$u_B(\boldsymbol{k},\boldsymbol{r}) = \frac{1}{\sqrt{N}}\sum_{i=1}^{N} e^{i\boldsymbol{k}(\boldsymbol{R_i}+\boldsymbol{\delta})}\,\varphi_B(\boldsymbol{r}-\boldsymbol{R}_i-\boldsymbol{\delta})$$

where $\boldsymbol{\delta} = (\frac{a_G}{\sqrt{3}}, 0)$ is the displacement between the two carbon atoms in the unit cell and N the total number of unit cells.

If we introduce these two expressions into the Hamiltonian we obtain an expression for the energy $E(\boldsymbol{k})$:

$$E(\boldsymbol{k}) = \int \Psi_k{}^* \hat{H}\, \Psi_k d\boldsymbol{r}$$

$$E(\boldsymbol{k}) = \frac{1}{N}\sum_{i,j=1}^{N,N} e^{i\boldsymbol{k}(\boldsymbol{R_i}-\boldsymbol{R_j})} \int \left(A^* \varphi_{Aj}^* + B^* e^{-i\boldsymbol{k}\boldsymbol{\delta}} \varphi_{Bj}^*\right) \hat{H} \left(A\varphi_{Ai} + B e^{i\boldsymbol{k}\boldsymbol{\delta}} \varphi_{Bi}\right) d\boldsymbol{r} \qquad (2.2)$$

with $\varphi_{Ai} = \varphi_A(\boldsymbol{r} - \boldsymbol{R_i})$, $\varphi_{Bi} = \varphi_B(\boldsymbol{r} - \boldsymbol{R_i} - \boldsymbol{\delta})$ and similarly for j.

Since the size of the layer is considered infinite when can extract the first sum in Eq 2.2. In addition, we can make the change of variable $\boldsymbol{\rho_j} = \boldsymbol{R_j} - \boldsymbol{R_i}$. With this we obtain:

$$E(\boldsymbol{k}) = \sum_{j=1}^{N} e^{i\boldsymbol{k}\boldsymbol{\rho}_j} \int \left(A^* \varphi_{Aj}^* + B^* e^{-i\boldsymbol{k}\boldsymbol{\delta}} \varphi_{Bj}^*\right) \hat{H} \left(A\varphi_{Ai} + B e^{i\boldsymbol{k}\boldsymbol{\delta}} \varphi_{Bi}\right) d\boldsymbol{r} \qquad (2.3)$$

We can write this expression as a matrix:

$$E(\boldsymbol{k}) = (A^*(\boldsymbol{k}), B^*(\boldsymbol{k})) \begin{pmatrix} H_{AA} & H_{AB} \\ H_{BA} & H_{BB} \end{pmatrix} \begin{pmatrix} A(\boldsymbol{k}) \\ B(\boldsymbol{k}) \end{pmatrix} \qquad (2.4)$$

For the diagonal terms we have:

$$H_{AA} = \sum_{j=1}^{N} e^{-i\boldsymbol{k}\boldsymbol{\rho}_j} \int \varphi_A^* (\boldsymbol{r} - \boldsymbol{\rho_j}) \hat{H} (\varphi_A(\boldsymbol{r}) d\boldsymbol{r}$$

Since we consider only nearest neighbors, $\boldsymbol{\rho_j} = 0$:

$$H_{AA} = \sum_{\boldsymbol{n.n}} e^{-i\boldsymbol{k}\boldsymbol{\rho}_j} \int \varphi_A^* (\boldsymbol{r} - \boldsymbol{\rho_j}) \hat{H} (\varphi_A(\boldsymbol{r}) d\boldsymbol{r} = \int \varphi_A^* (\boldsymbol{r}) \hat{H} (\varphi_A(\boldsymbol{r}) d\boldsymbol{r}$$

We can represent the Hamiltonian $\hat{H}$ as a sum of the Hamiltonian of a single atom $\hat{H}_{\text{Atomic}}$ and the perturbation from neighboring atoms ΔV:

$$H_{AA} = \int \varphi_A^* (\boldsymbol{r}) \hat{H} (\varphi_A(\boldsymbol{r}) d\boldsymbol{r} = \int \varphi_A^* (\boldsymbol{r}) \hat{H}_{Atomic} (\varphi_A(\boldsymbol{r}) d\boldsymbol{r} + \int \varphi_A^* (\boldsymbol{r}) \Delta V (\varphi_A(\boldsymbol{r}) d\boldsymbol{r}$$

$$H_{AA} = E_{pz} + \alpha = E_0 \qquad (2.5)$$

Similarly for H_{BB}:

$$H_{BB} = E_{pz} + \alpha = E_0 \tag{2.6}$$

For the off diagonal terms we have:

$$H_{AB} = \sum_{n.n} e^{-i\boldsymbol{k}(\boldsymbol{\rho_j}-\boldsymbol{\delta})} \int \varphi_A^* \left(\boldsymbol{r}-\boldsymbol{\rho_j}\right)\widehat{H}\, e^{i\boldsymbol{k}\boldsymbol{\delta}}\varphi_B\,(\boldsymbol{r}-\boldsymbol{\delta})d\boldsymbol{r}$$

$$= f\,(\boldsymbol{k})\int \varphi_A^*\,(\boldsymbol{r})\Delta V\,\varphi_B\,(\boldsymbol{r}-\boldsymbol{\delta})d\boldsymbol{r} = -\,f\,(\boldsymbol{k})\,t$$

Since the contribution from $\widehat{H}_{Atomic}$ in this case is equal to zero.

In order to calculate $f\,(\boldsymbol{k})$ we can use Fig 2.3 which indicates the position of the neighbouring atoms: $(\boldsymbol{\rho_j}-\boldsymbol{\delta})$

a

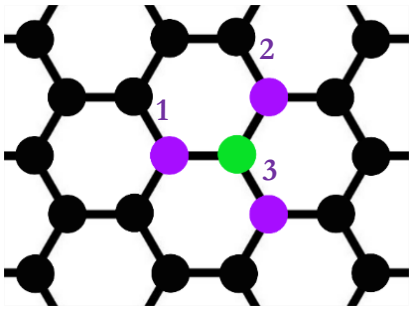

b

Site	$\boldsymbol{\rho_j}-\boldsymbol{\delta}$
1	$\left(-\frac{a_G}{\sqrt{3}},0\right)$
2	$\left(\frac{a_G}{2\sqrt{3}},\frac{a_G}{2}\right)$
3	$\left(\frac{a_G}{2\sqrt{3}},-\frac{a_G}{\sqrt{3}}\right)$

Figure 2.3: a) Schematic of nearest neighbours of atom B. b) Table indicating the position of nearest neighbours.

With this we have:

$$f\,(\boldsymbol{k}) = \sum_{n.n} e^{-i\boldsymbol{k}(\boldsymbol{\rho_j}-\boldsymbol{\delta})} = e^{\frac{ik_x a_G}{\sqrt{3}}} + e^{-i\left(\frac{k_x a_G}{2\sqrt{3}}+\frac{k_y a_G}{2}\right)} + e^{-i\left(\frac{k_x a_G}{2\sqrt{3}}-\frac{k_y a_G}{2}\right)}$$

$$= e^{\frac{ik_x a_G}{\sqrt{3}}} + 2e^{-i\left(\frac{\sqrt{3}k_x a_G}{2}\right)}\cos\left(\frac{k_y a_G}{2}\right) \tag{2.7}$$

where a_G is the module of the unit cell vector.

Similarly, for H_{BA}:

$$H_{BA} = -t\ f(\boldsymbol{k})^* = {H_{AB}}^*$$

The Hamiltonian matrix then is:

$$H = \begin{pmatrix} E_0 & -tf(\boldsymbol{k}) \\ -tf(\boldsymbol{k})^* & E_0 \end{pmatrix} \tag{2.8}$$

Solving the eigenvalue equation of the Hamiltonian:

$$E = E_0 \pm t\sqrt{f(\boldsymbol{k})^*\, f(\boldsymbol{k})} = E_0 \pm t|f(\boldsymbol{k})|$$

We can set E_0 as a reference energy. Therefore $E_0 = 0$ and the previous expression results in:

$$E = \pm\, t|f(\boldsymbol{k})| \tag{2.9}$$

Given that:

$$f(\boldsymbol{k})^*\, f(\boldsymbol{k}) = 1+4cos\left(\frac{k_y a_G}{2}\right) cos\left(\frac{\sqrt{3}k_x a_G}{2}\right)+4cos^2\left(\frac{k_y a_G}{2}\right)$$

we can substitute this into equation 2.9 to obtain:

$$E(k) = \pm t\sqrt{1 + 4cos\left(\frac{\sqrt{3}k_x a_G}{2}\right) cos\left(\frac{k_y a_G}{2}\right) + 4cos^2\left(\frac{k_y a_G}{2}\right)} \tag{2.10}$$

This expression indicates that there is a gap between the two bands except at the points where $f(\mathbf{k}) = 0$. For this, the conditions are:

$$\frac{\sqrt{3}k_x a_G}{2} = 2n\pi, \qquad \cos\left(\frac{k_y a_G}{2}\right) = -1/2$$

or $$\frac{\sqrt{3}k_x a_G}{2} = (2n+1)\pi, \quad \cos\left(\frac{k_y a_G}{2}\right) = 1/2 \quad \text{with } n = 0,1,2,3\ldots$$

The first choice is outside of the first Brillouin zone but the second falls exactly at the K and K' points. We can expand $f(\mathbf{k})$ to first order around K and K' points by defining **q** = **k** - **K** around q ≈ 0. Omitting phase factors that do not affect any physical result, we obtain:

$$f_K(\mathbf{q}) \approx \frac{\sqrt{3}a_G}{2}(iq_x - q_y) \quad ; \quad f_{K'}(\mathbf{q}) \approx \frac{\sqrt{3}a_G}{2}(iq_x + q_y)$$

With this, we have that the eigenenergies are:

$$E = \pm \frac{\sqrt{3}ta_G}{2} q = \pm \hbar q v_F \tag{2.11}$$

with $\mathrm{q} = \sqrt{\mathrm{q_x}^2 + \mathrm{q_y}^2}$, $v_F = \frac{\sqrt{3}ta_G}{2\hbar} \approx \frac{10^6 m}{s}$

The $\pm$ signs correspond to the eigenenergies at the conduction (+) and valence (-) bands. As equation 2.11 shows, the energy dispersion near the K and K' points is linear. Due to this linearity, charge carriers behave as massless Dirac fermions with velocities $v_F = \frac{\sqrt{3}ta_G}{2\hbar} \approx \frac{10^6 m}{s}$. The K and K' points where this linear dispersion occurs receive the name of Dirac points. In the vicinity of these points, the Hamiltonian takes the form of the Dirac equation for relativistic fermions:

$$\hat{H}\Psi = -i\hbar v_F(\boldsymbol{\sigma} \cdot \nabla)\Psi = \hbar v_F \begin{pmatrix} 0 & q_x - iq_y \\ q_x + iq_y & 0 \end{pmatrix} \Psi = E\Psi \tag{2.12}$$

where $v_F$is the Fermi velocity and the pseudospin $\boldsymbol{\sigma} = \sigma_x + \sigma_y$ is a vector of Pauli matrices. The components of this pseudospin correspond to the amplitudes of the wavefunction on each sublattice. In graphene the direction of motion is coupled with this pseudospin. The eigenfunctions of this Hamiltonian are:

$$\Psi_{\pm} = \frac{1}{\sqrt{2}} \begin{pmatrix} e^{-\frac{i\varphi}{2}} \\ \pm e^{\frac{i\varphi}{2}} \end{pmatrix} \tag{2.13}$$

with $\varphi = \arctan\left(\frac{q_y}{q_x}\right)$

Figure 2.4 shows the band structure of graphene. As previously discussed, the valence and conduction bands are separated by an energy gap all along the Brillouin zone except at the K and K' points where they form Dirac cones that touch each other exactly at the Fermi level (for undoped graphene), known as the Dirac point.

The pseudospin in graphene is restricted to the x-y plane since the two carbon sites experience the same potential[47]. Introducing a potential that is different on the A sublattice than in the B sublattice generates diagonal terms in the Hamiltonian which can result in a bandgap. This can be done by growing or mechanically placing graphene on hexagonal boron nitride.

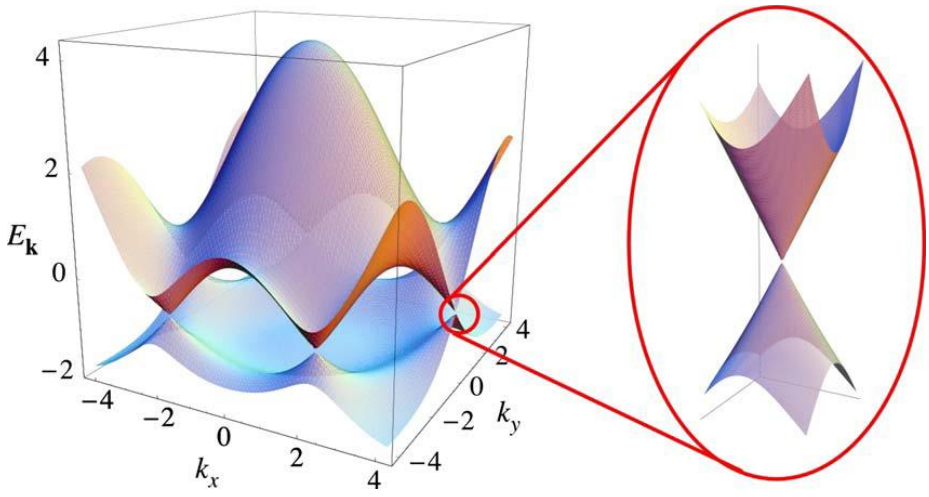

Figure 2.4: Electronic structure of Graphene. Inset shows one of the Dirac points with linear dispersion. Extracted from [2].

2.2 Hexagonal Boron Nitride

Boron nitride (BN) is an insulator with a ~5.97eV band gap[48] composed of boron and nitrogen atoms, which occupy respectively the first period of groups III and V in the periodic table. In combination, boron and nitrogen have the same number of electrons in the outer shell as carbon i.e. is isoelectronic to carbon. Therefore, BN can form crystal structures analogous to those formed by carbon: Hexagonal BN (hBN) has σ bonds derived from sp^2 hybridized orbitals from both nitrogen and boron atoms, while cubic BN (cBN) and the rare wurtzite BN (wBN) contain sp^3 hybridized bonds. As opposed to graphene, in hBN π bonding between the full $2p_z$ orbital of boron and the empty $2p_z$ orbital of nitrogen does not occur since their orbital energies are too dissimilar for an energy gain. This leaves no delocalized electrons and makes hBN an insulator.

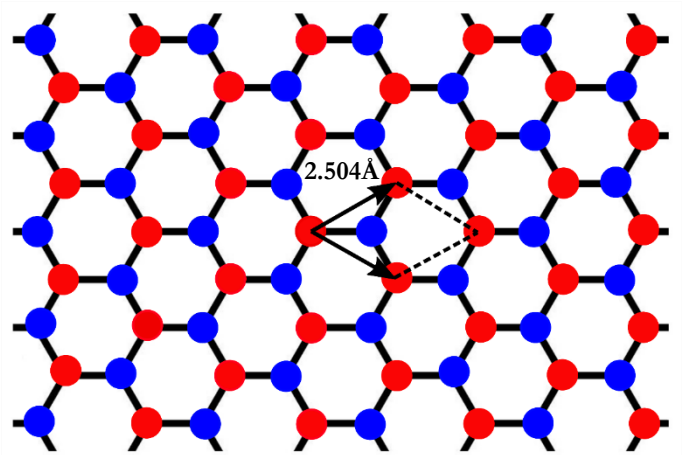

Figure 2.5: Top view of the hexagonal boron nitride crystal structure. The unit cell vectors are indicated by the black arrows. Lattice constant is 2.504Å.

Hexagonal BN has a honeycomb structure similar to graphite, where atoms in the same plane are held to three neighbours by covalent bonds. The angles between bonds are also 120°.

The fact that boron, nitrogen and carbon are so close in the periodic table is also responsible for the small lattice mismatch between graphene and hBN. The hBN lattice constant is a_{hBN}= 2.504 Å[49], which gives a relative mismatch δ = $(a_{hBN} - a_G)/\, a_G \approx$ 0.018 . As in graphite, the planes of atoms are held together by weak van der Waals forces that allow mechanical exfoliation of the crystal. It is worth noting that the stacking of planes shown in Fig 2.6, although having the same AB order as in graphite

Bernal stacking, is slightly different. In graphite, half of the atoms in each ring lie on top or below the center of the rings of the neighboring planes while the other half is on top or below atoms in the neighboring planes. In the case of hBN, each N (B) atom has a B (N) atom directly above and below in the neighboring planes. Hexagonal boron nitride is highly thermally conductive, highly thermally stable (melting point 2973 °C), chemically inert and free of dangling bonds and surface charge traps, which make it an attractive substrate for molecular deposition and crystal growth[50–52]. For comparison, the thermal conductivities along its basal plane[53] at room temperature are about 400 $W(mK)^{-1}$ similar to copper and silver. In addition, hBN has a high relative permittivity[54] ($\varepsilon_{\text{in plane}} \sim 6.9$ and $\varepsilon_{\text{out of plane}} \sim 3.8$) and a breakdown voltage (0.7 Vm^{-1}) which make it an ideal alternative dielectric substrate to SiO_2.

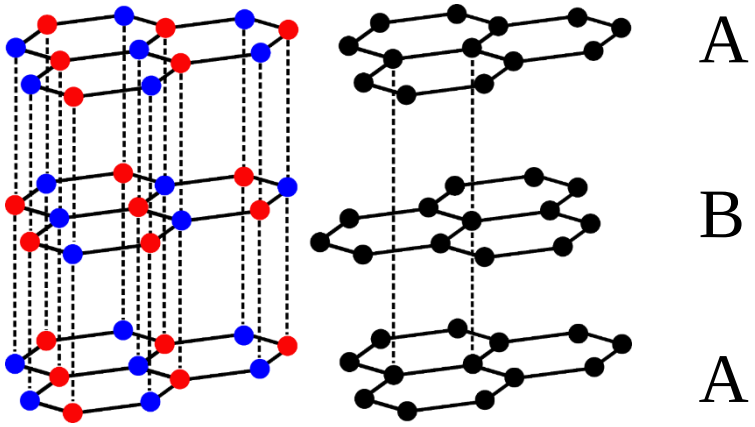

Figure 2.6: Side view of the crystal structures of hBN (left) and graphite (right) showing the stacking of the different planes of atoms.

2.3 Graphene/hBN heterostructures

Hexagonal boron nitride was initially used in graphene-based devices as a low interaction alternative dielectric to SiO_2[55], which is amorphous. Surface disorder breaks the 2D electron gas in graphene on SiO_2 at the Dirac points into an inhomogeneous network of electron and hole puddles, charge carrier mobilities remain below 15000 $cm^2\,V^{-1}s^{-1}$ at RT. Randomly stacked graphene on hBN devices show charge carrier mobilities of 60000 $cm^2\,V^{-1}s^{-1}$ at RT[50] or even 100000 $cm^2\,V^{-1}s^{-1}$ when

graphene is encapsulated between two hBN crystals. This is almost an order of magnitude higher than SiO_2.

Scanning tunnelling microscopy (STM) images of the surface of graphene on hBN revealed topographical long wave hexagonal modulations [51,52,56]. These superstructures, known as Moiré patterns, emerge when lattices with different lattice constant and/or alignment are placed on top of each other. A few examples of Moiré patterns are shown in Fig 2.7.

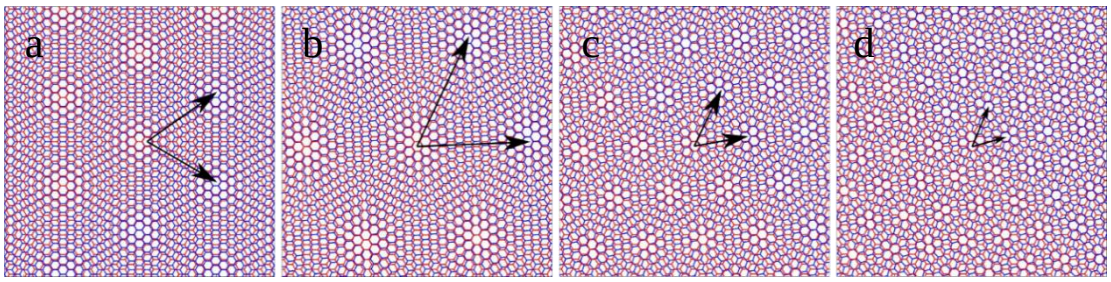

Figure 2.7: Moiré patterns formed by two superimposed hexagonal lattices. In (a) lattices aligned with a 10% lattice constant mismatch. In the rest of the images the lattices have the same lattice constant but are rotated (b) 5°, (c) 10° and (d) 15°. Moiré vectors are indicated with black arrows.

The large period of the Moiré formed when graphene and hBN lattices are perfectly aligned, ~14 nm, is due to the small fractional lattice mismatch between the two crystals ($\delta = (a_{hBN} - a_G)/a_G \approx 0.018$). The Moiré period reduces very fast as the rotation angle φ between the lattices is increased.

The Moiré period λ depends on the rotational angle ϕ between the two lattices and the fractional mismatch δ as follows[56]:

$$\lambda = \frac{(1+\delta)a_G}{(2(1+\delta)(1-cos\phi)+\delta^2)^{\frac{1}{2}}} \tag{2.12}$$

The rotation angle θ between the Moiré pattern and the graphene lattice depends as well on φ and δ as follows:

$$tan\,\theta = \frac{sin\,(\phi)}{(1+\delta)-cos(\phi)} \tag{2.13}$$

Examples of G/hBN Moiré patters obtained by STM with different rotation angles extracted from [56] are shown in Fig 2.8. A graph showing the dependence of the Moiré period with the rotation angle between the two lattices can be found on Fig 2.8.d.

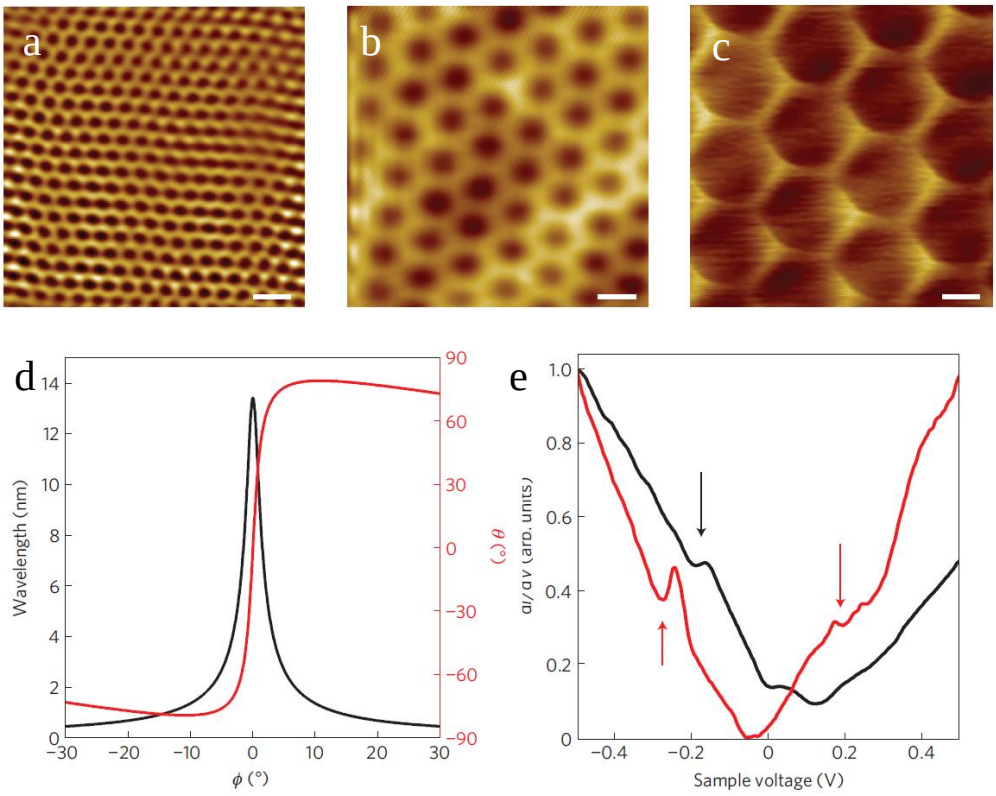

Figure 2.8: a-c) STM topographic images showing 2.4 nm (a), 6.0 nm (b) and 11.5 nm (c) Moiré patterns. Scale bars 5 nm. d), Superlattice wavelength λ (black line) and rotation θ (red line) as a function of the angle ϕ between the graphene and hBN lattices. e) Experimental STM dI/dV curves for two different Moiré wavelengths, 9.0 nm (black) and 13.4 nm (red). The dips in the dI/dV curves are marked by arrows. Figure adapted from [56].

Graphene forms Moiré patterns on other crystalline substrates such as HOPG[57], SiC[58], and a series of transition metals[44] with different periodicities and orientation. On most of these transition metal substrates more than one configuration has been reported. In general, the number of possible configurations decreases with the strength of the interaction between graphene and the metal. Extreme examples of this trend are Ir, where graphene interacts only through weak van der Waals forces and six different Moiré orientations are found[59], and Ru, where the strong interaction between the two lattices, with partial interfacial C-Ru bonds, allows only one configuration, with both lattices aligned[60].

The effects produced by the Moiré pattern on the electronic structure of graphene on hBN are twofold. Firstly, the Moiré generates an associated periodic superlattice potential which leads to the formation of six secondary Dirac points (sDP) in the valence and in the conduction band, symmetrically placed around each original Dirac point. The energies at which these sDP develop increase with decreasing Moiré period. Fig 2.8 shows two dI/dV curves obtained by STM spectroscopy performed on two different graphene on hBN heterostructures. These curves are proportional to the Local Density of States (LDOS). The black line corresponds to a heterostructure with a 9.0 nm Moiré period while the red line corresponds to a 13.4 nm (red) Moiré. The sDP generate dips in the curves which are indicated with arrows. The superlattice potential also generates a splitting of the Landau levels of the 2D electron gas in the presence of a perpendicular magnetic field. When the relation between the magnetic flux per unit cell and the magnetic flux quantum is a rational number, the degeneracy of the electrons in cyclotron orbits is lifted. The spectra of these Landau levels forms one of the rare fractal structures found in physics known as the Hofstadter butterfly[61]. The experimental realization of this phenomena is difficult. A typical lattice periodicity of the order of 1Å needs a magnetic field of 10kT which is impossible to reach nowadays. The large Moiré pattern formed by aligned graphene on hBN and its associated potential allow the observation of the splitting of these Landau levels at experimentally accessible magnetic fields thanks to the comparable sizes of the cyclotron orbits and the superlattice potential[62].

Secondly, the Moiré pattern can break locally the sublattice A-B symmetry of the two atoms in the graphene unit cell, which protects the opening of a bandgap. The difference in potential between nitrogen and boron atoms provides a chemical environment for the two graphene atoms in the unit cell that gradually changes as we move along the layer. But the effect could be compensated after spatial averaging, which would prevent the formation of a band gap.

Woods et al. proposed that a commensurate−incommensurate transition occurs when the lattices are aligned[63]. Under this condition, the van der Waals potential is strong enough to overcome locally the elastic energy of the graphene layer, displacing graphene atoms from their equilibrium positions.

Lattice resolution STM images show a small variation of the graphene lattice constant across the Moiré unit cell (Fig 2.9a-b), approximating to the value for hBN in the flat central areas while remaining closer to free standing graphene at the few pico-meters high domain walls. The graphene layer has an extra row of atoms, with respect to hBN, running parallel to the domain wall (Fig 2.9c). In this scenario, the unit cell symmetry could be broken locally at the centre of the Moiré pattern where the graphene is strained. In this case, the local strain is compensated by this extra row of atoms at the domain walls in a way that the overall strain averaged over the Moiré unit cell is negligible.

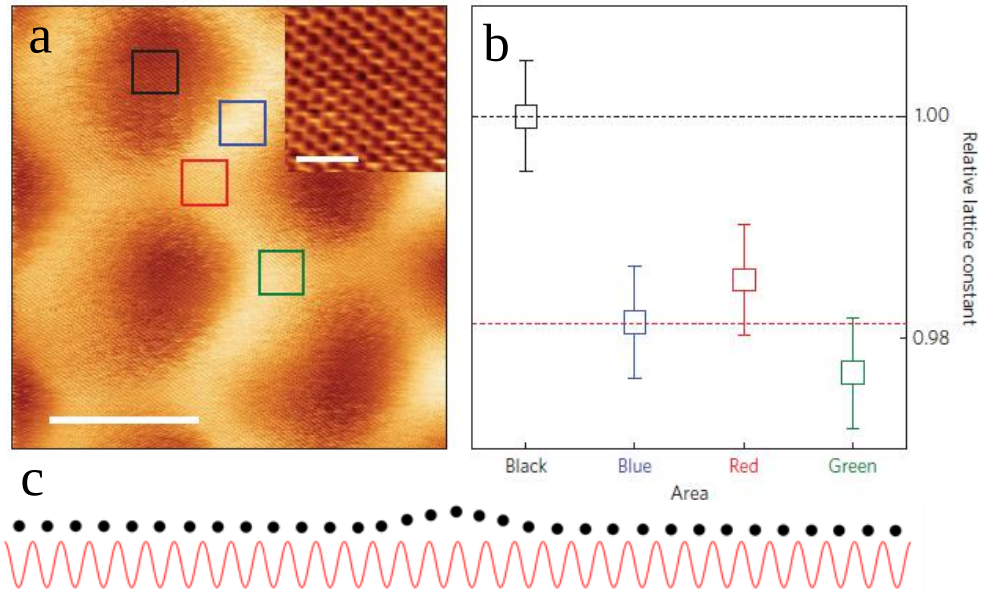

Figure 2.9: a) STM image of an aligned graphene/hBN structure showing both the Moiré pattern and the atomic structure (inset with 1 nm scale bar). Lattice resolution images like the one on the inset where used to determine the lattice constant of graphene through a Fourier transform. Scale bar 10 nm. b) Ratio of the lattice constants between graphene and hBN at the positions indicated by the coloured boxes in a. Adapted from [63].c) Schematic vertical (and perpendicular to the domain wall) cut of the graphene lattice (black dots) with the potential generated by the hBN lattice (red line). The graphene is strained and matches the hBN lattice on each side of the dislocation line.

In contrast, high temperature MBE grown graphene on hBN by Summerfield et al[64] showed Moiré periodicities up to ~ 30 nm, which can only be generated by a significant ~ 1% overall strain. We can approximate the average strain of the graphene layer as a function of the Moiré size. For this we shall consider,

Unstrained graphene

$$\lambda_0 = \frac{(1+\delta)a_G}{\delta} \text{ with } \delta = \frac{a_{hBN} - a_G}{a_G}$$

Strained graphene

$$\lambda_S = \frac{(1+\delta')a'_G}{\delta'} \text{ with } a'_G = a_G + \Delta a_G \text{ and } \delta' = \frac{a_{hBN} - a'_G}{a'_G} = \frac{a_{hBN} - a_G - \Delta a_G}{a_G + \Delta a_G}$$

Taking the ratio between these expressions and rearranging gives,

$$\frac{\Delta a_G}{a_G} = \delta \frac{\lambda_S - \lambda_0}{\lambda_S} \tag{2.14}$$

Notice that in the limit $\lambda_s \to \infty$, $\frac{\Delta a_G}{a_G} = \delta$. This means that the Moiré period diverges as the strain of the graphene layer approximates to the lattice mismatch between the two lattices.

Figure 2.10 shows a few of these large periodicity Moiré patterns. Authors propose that the strain could be generated during post-growth cooling due to a difference in thermal expansion coefficients between the two crystals and maintained through pinning by irregular carbon deposits formed at defects in the hBN substrate.

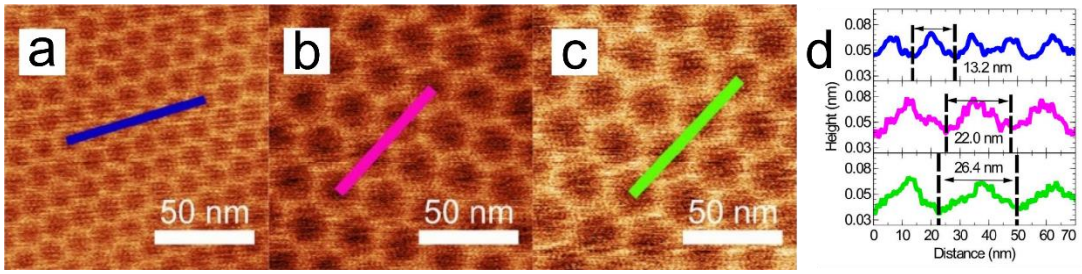

Figure 2.10: AFM images of Moiré patterns of graphene grow on hBN by MBE by Summerfield et al. with sizes ranging from 13.2 nm to 26.4 nm. The percentages of overall strain calculated from the Moiré periodicities are a) 0% b) 0.66% and c) 0.84%. Adapted from [63].

A tensile strain of ~1%, is observed, implying that the relationship between the expansion coefficients (α_g-α_{hBN}), averaged over the relevant temperature growth range (300–1770 K) is positive with a value 8×10^{-6}/ K. Nevertheless, since the magnitudes of the expansion coefficients of graphene[65] and bulk hBN[66] above 800K are unavailable, thermally induced strain is considered a plausible origin. A similar mechanism for introducing strain in graphene has been observed on graphene layers grown on SiC[67]. The strained graphene layers on hBN can relax spontaneously, weeks after growth or by scratching the layer with an AFM tip, forming cracks on the surface. The cracked layers display lower Moiré periodicities following strain relaxation. Interestingly, depending on the location of the crack and the carbon deposits pinning

the layers, anisotropically strained layers can be formed where the periodicities of the Moiré pattern differ for different directions or even Moiré patterns that gradually change their orientation across the layer. These features provide confirmation of the graphene layers being subjected to an overall strain. In addition, Summerfield et al. provide Raman spectra that shows splitting of the 2D peak, which indicates areas with different strains. The central areas of the Moiré pattern that appear lower in the STM and AFM images are under biaxial strain while close to the domain walls the strain is uniaxial.

Strain in graphene is of great interest as it can alter the Hamiltonian in a way that the electrons experience a potential as if they were subjected to a magnetic field perpendicular to the surface plane i.e. strain can induce pseudo-magnetic fields. For example, it has been shown that designed strain aligned along the main three crystallographic directions of graphene does not break the sublattice symmetry but rather shifts in opposite directions the Dirac cones at K and K' points, which is equivalent to the effect induced by a uniform magnetic field perpendicular to the plane on charge carriers[68]. It is argued that hBN could induce this type of stresses on graphene[69,70].

In parallel, early theoretical calculations based on a lowest energy configuration, predicted that lattice matched graphene on hBN would exhibit a bandgap of 53 meV [71]. In this configuration, one of the sublattices of carbon atoms sits above boron atoms in hBN while the other sits above the centre of the hexagon ring, breaking the sublattice A-B symmetry globally rather than locally. Opening a band gap by symmetry breaking through substrate interactions has been successfully explored by epitaxial growth on SiC[72,73]. Nevertheless, the mechanism to achieve the necessary 1.8% bi-axial strain that allows graphene to lattice match hBN over a significant area remained unsolved and was considered, until recently unachievable.

2.4 Graphene on hBN fabrication techniques

The most common methods for fabricating graphene devices on hBN nowadays are micromechanical exfoliation using adhesive tape and chemical vapor deposition (CVD). Micromechanical exfoliation from highly orientated pyrolytic graphite (HOPG) was the method used by Geim and Novoselov to isolate graphene and measure its electronical properties for the first time[1]. Graphene can be seen under white light, with an optical microscope when it lies on a SiO_2/Si substrate. Oxide thickness values of ~90 nm or ~280 nm maximize the contrast.[15] This allows a relatively easy and low cost identification of monolayers. However, mechanical exfoliation is a time-consuming process and only flakes on the scale of ~100 µm can be obtained, far from the wafer scale needed for industrial applications. Growth of graphene by CVD by dissociation of methane on nickel [34] and soon after on copper[37] were demonstrated, providing large area coverages.

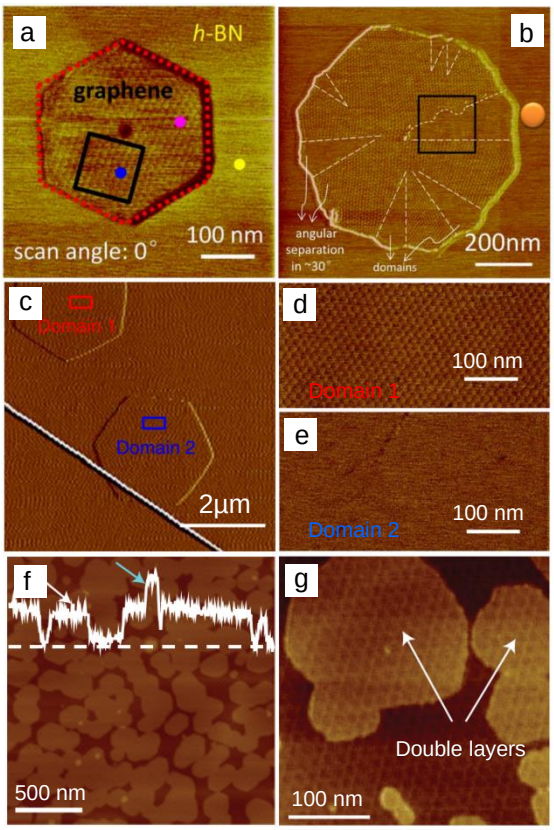

Figure 2.11: AFM images of graphene grown on hBN by CVD. Extracted from (a-b) [75], (c-d) [76], (f-g) [77].

After etching of the metal substrate, the graphene layer can be placed onto dielectric substrates like SiO_2 or hBN by dry or wet transfer methods[74]. The use of electron beam lithography (EBL) to tailor the contacts of these devices as well as stamping systems that allow control of the rotational alignment of the different crystals provide a route to device fabrication. CVD growth of graphene directly on hBN has been explored by a few groups obtaining in most of the cases growth of small islands. The most interesting results are in references[75–77]. The first of these studies, by Tang et al., using no catalyst or plasma shows growths of graphene islands with a few hundreds of nm across[75]. Most of the islands have faceted hexagonal edges oriented in the armchair

direction (Fig 2.11a) although depending of the precise growth conditions, the edges can also be more irregular (Fig 2.11b). In some of the islands with more irregular edges, epitaxial domains aligned to hBN exhibiting the expected ~14 nm Moiré pattern, coexist with rotated domains that show no Moiré pattern at all. Also, images of an island with a second layer are shown. A later study by the same group[76], this time using silane (SiH_4) as a catalyst shows much larger islands with maximum sizes of 20 μm. Most of these islands, from their hexagonal faceted edges and the sizes of their Moiré patterns, appear to be aligned with the substrate lattice. Nevertheless, authors show also images of an island where the Moiré pattern is absent. The edges of this island are ~30° rotated with respect to another aligned island situated a few μm away (Fig 2.11c-e). The sizes of such islands are enough to deposit metal contacts through electron beam evaporation and perform transport measurements. In the last of these studies, where a plasma source is used to break down the precursor molecule before growth, methane (CH_4), a single domain of epitaxial graphene with the usual Moiré covering the hole flake is obtained[77] (Fig 2.11f). Also, second and even third layers are formed through further deposition (Fig 2.11g). This last study also shows transport measurements where secondary Dirac points generated by the Moiré pattern influence the resistivity of Quantum Hall Effect fan diagrams.

2.5 Graphene grown on hBN by molecular beam epitaxy

Molecular beam epitaxy (MBE) is a crystal growth technique performed in ultra-high vacuum (10^{-10} Torr), where beams of atoms or molecules react with a heated crystalline substrate in order to form epitaxially grown highly pure crystal structures. MBE was developed at Bell Laboratories in the late 60's [78] by Alfred Y. Cho and John R. Arthur, Jr.

Epitaxy, is derived from the Greek roots epi (ἐπί), meaning "above", and taxis (τάξις), meaning "in an ordered manner" indicates that the crystal grown has the same or a similar structure as the substrate crystal and they keep, in general, a fixed orientation and registry. This ordered growth is obtained in MBE by a slow deposition rate ~1000 nm/hour. High substrate temperatures allow adsorbed species to diffuse along the

surface and incorporate at suitable sites. The low deposition rates require lower vacuum pressures compared to other growth techniques. The atomic or molecular beams are provided by different pure species heated in separate Knudsen cells. The intensity of the beams depends on the cells' temperature, which can be adjusted to take into account the different sticking coefficients of the different species and therefore set very precisely the stoichiometry of the grown crystals. Computer controlled shutters situated at the end of the cells can sequentially interrupt the beams of different species to control the thickness of different layers of crystals. In this way, heterostructures composed of thin alternating layers such as GaAs and GaAlAs, can be formed. In these structures electrons can be confined into quantum wells or quantum dots. The growth is typically monitored by reflection high energy electron diffraction and quadruple mass spectrometry.

Previous to the work by the Nottingham Graphene MBE group, the use of MBE to grow graphene directly on hBN had been explored[79,80] with partial success (Fig 2.12). Although Raman spectra indicates the presence of graphene in both of these studies, only AFM scans in Jorge M. Garcia et al. work show a recognizable layer, emerging just a few hundreds of nm from bulk carbon deposits adsorbed on hBN step edges (Fig 2.12a). These results are far from producing the quality and size of graphene layers obtained by mechanical exfoliation, by CVD growth on a sacrificial substrate or even by direct CVD growth on hBN. As was later shown by the Nottingham Graphene MBE group[64], the temperatures needed to obtain an appropriate mobility of carbon in the surface were around 500 °C higher than those achievable by conventional MBE systems at the time, around 1000 °C.

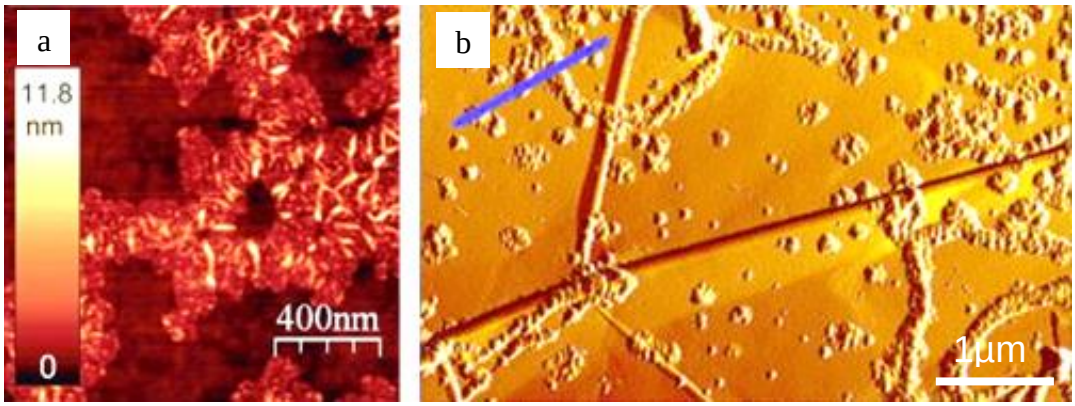

Figure 2.12: AFM images of earlier attempts of growing graphene by MBE from references (a) [79] and (b) [80].

2.6 Raman spectroscopy on graphene

Raman spectroscopy is a light scattering technique, whereby a molecule or a material scatters incident light from a high intensity laser light source. A small amount of light is scattered at different wavelengths, which depend on the chemical structure of the sample.

A Raman spectrum features a number of peaks, showing the intensity and wavelength position of the Raman scattered light. Each peak corresponds to a specific molecular bond vibration, can be used to detect and characterize graphene giving information about the number of layers, the density of defects[81,82], and most importantly for our case, the magnitude and nature of the strain within the layers[83,84]. Three main peaks G, D and 2D are observed in graphene. These peaks are used to detect the presence of graphene and deduce its thickness and number of defects.

The G peak at around 1580 cm^{-1} is associated with the doubly degenerate in-plane transverse optical (iTO) and longitudinal optical phonon (LO) modes at the Γ point and it is the only peak generated by a normal first order Raman scattering process in graphene. All sp^2 bonded carbon atoms such as fullerenes and nanotubes exhibit the G peak. These optical phonon modes correspond to vibrations of the sublattice A against sublattice B.

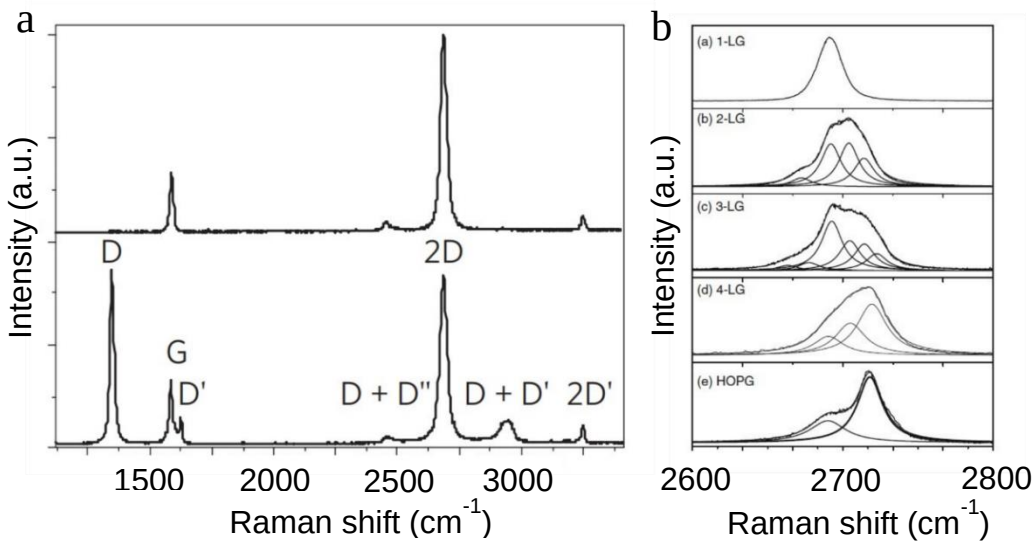

Figure 2.13: a) Raman spectrum of pristine (top) and defected (bottom) graphene. b) Evolution of the 2D peak with the number of layers. Extracted from [81]

The D peak located around 1360 cm^{-1}arises from a second order inter-valley K point scattering process involving one iTO phonon and one defect. The D peak is strongly dispersive with excitation energy due to a Kohn anomaly at the K point[85]. Since the activation process for the D peak involves defect scattering, the ratio between the intensities of the G and D peaks gives a measure of the quality of graphene.

The 2D peak at 2700 cm^{-1} arises from a second order inter-valley K point scattering process but in this case involving two iTO phonons at the Γ point. The 2D peak is present in defect free graphene. Since the valence and conduction bands are symmetric with respect to the Fermi level, triple resonance processes involving scattering of holes can occur. This can explain the larger intensity of the 2D peak compared to the G band. The principal Raman scattering processes are shown in Fig 2.14.

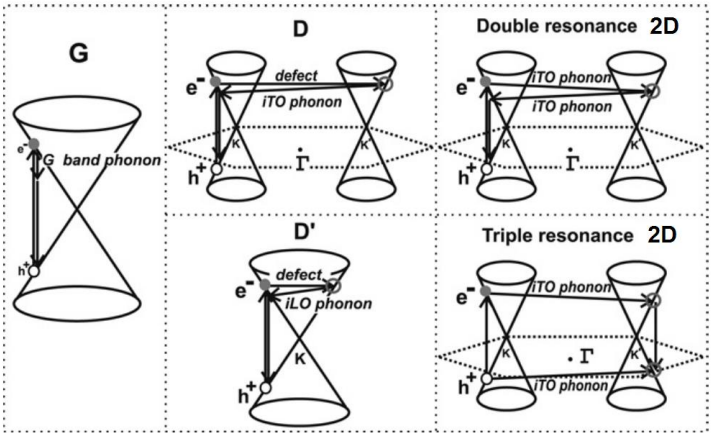

Figure 2.14: Principal Raman scattering processes in graphene. Extracted from [81].

Increasing the number of graphene layers results in a larger number of electron-hole creation transitions as well as a larger number of iTO phonon branches. This results in an increased number of possible K to K' electron-phonon scattering processes which progressively broadens and blueshifts the Raman 2D peak towards the expected shape of bulk graphite[86] as shown in Fig 2.13b. Additional peaks are present on defected graphene like the D' at ~1620 cm^{-1} and the 2D' at ~3230 cm^{-1}. The D' peak arises from a double resonance in an intravalley scattering of a photo-excited electron by a phonon along with elastic scattering by a defect. The 2D' is its overtone and, as the 2D peak, does not need defects for its activation so it is always present. In addition, the D+D' peaks are produced by one intravalley and one intervalley phonon scattering processes, and the D+D'' peak by two intervalley photon scattering processes, both in the presence of defects.

Raman spectra are also affected by strain. Graphene was deposited onto a polymer substrate which was a posteriori uniaxially deformed generating uniaxial strain in the graphene layer. The G and 2D bands appear shifted by a magnitude proportional to the strain and the G peak splits into two[83]. As mentioned earlier, the origin of the G band arises from a doubly degenerate E_{2g} phonon mode at the Γ point. When the uniaxial strain is applied, the rotational symmetries of graphene are lost, splitting the E_{2g} phonon mode into two singlet modes that give rise to the G^+ and G^- peaks. In fact, the relative intensities of these peaks depend on the angle of incident polarization relative to the strain axis. In addition, studies also show the splitting of the 2D band at large strains caused by both the Dirac cone shifting and the anisotropic softening of phonon modes[87,88]. The Dirac mode shifting induces variations in the three equivalent scattering paths which involve scattering phonons with different momenta. In contrast, biaxial strain causes also redshifts but does not result in peak splitting, since all the symmetries of graphene are preserved. Such spectra have been reported for a graphene membrane under hydrostatic pressure[84] (Fig 2.15).

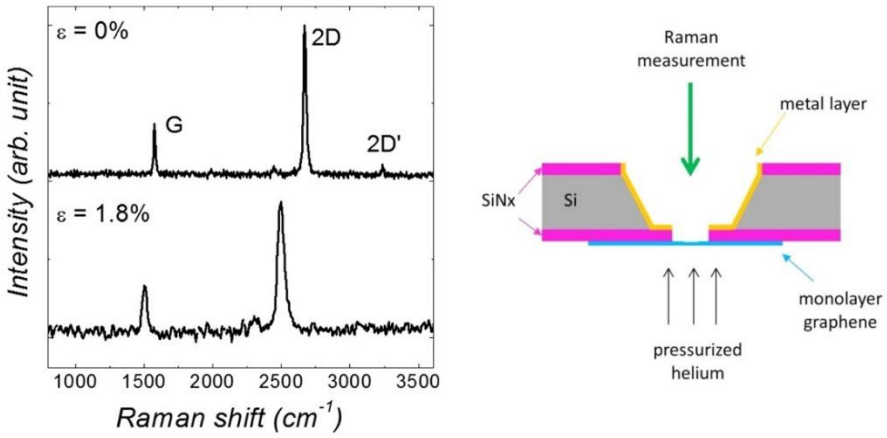

Figure 2.15: a) Raman spectra of a graphene membrane measured at ε ~ 0% and ε ~1.8% biaxial strain, measured at excitation wavelength of 514.5 nm. b) Experimental set up. The device is used to seal a chamber containing pressurized He gas. Extracted from [84].

2.7 Alkanes

The deposition of the long chain alkane hexacontane ($C_{60}H_{122}$) on hBN is described in chapter 7. Alkanes are open chain saturated hydrocarbons with the general chemical formula: C_nH_{2n+2}. In the case of alkanes the molecule forms only single bonds, as opposed to alkenes or alkynes containing at least one double or triple bond respectively. The structure of alkanes can be easily explained starting from methane (CH_4), and increasing the number of carbon atoms. Methane contains only one carbon atom bond to four hydrogen atoms. The 109.5° angles between C-H bonds are equal and form a tetrahedral shape. Ethane (C_2H_6) contains two carbon atoms joined by a single bond. The remaining three orbitals on each carbon atom form bonds with hydrogen atoms. Polyethylene, which is a mix of large chain alkanes is used in bags, toys, foams, containers, synthetic clothes and many other products.

Single sigma bonds allow rotation of the $–CH_2$ units since the sp^3 orbitals are symmetric about the internuclear axis. Steric effects, which consist of repulsive forces between overlapping electron clouds, determine the lowest energy conformation of the molecule. In the case of alkanes such conformation consists of all the C-C backbone bonds oriented in an alternating zig-zag configuration with an angle of 109.5°, leaving all the carbon atoms in the same plane.

Alkanes are not very reactive in comparison with other chemical species given the lack of double or triple bonds and the very stable sigma covalent bonds formed by sp^3 hybridized orbitals. In fact, alkanes are found in crude oil and natural gas, where they remain unchanged for millions of years. Alkanes are non-polar molecules and therefore are immiscible in polar solvents like water but can be dissolved in non-polar solvents like acetone, benzene or other alkanes. The boiling point of Alkanes increases with the chain length; typically the addition of each CH_2 segment increases the boiling point by between 10° and 20°. In the case of the melting point the trend is similar, but slightly distorted by the molecular packing of the solid crystal phase. For example propane has a lower melting point (85K) than methane (91K) due to a more densely packed crystal structure. Octadecane ($C_{18}H_{20}$) is the shortest alkane that is solid at room temperature. Longer alkanes are referred to as waxes.

2.8 Alkanes on graphite

The adsorption of alkane layers on graphite was initially studied using calorimetry techniques[89,90]. These studies revealed that the heats of adsorption for different alkanes increased linearly with the length of the chain, ~0.94 kJ/mol for each methylene unit. Also, since the area per molecule could be calculated from the adsorption isotherm, it was deduced that the length of the molecules adsorbed on graphite was slightly lower than in the three dimensional alkane crystal. Groszek et al suggested that the molecules were physisorbed with their long axis parallel to a main axis of graphite in an all-trans configuration. The methyl ($-CH_2-$) groups on the alkane chain lie on top of the centers of the carbon hexagons, where the substrate potential has a periodic minimum[90]. The length of alternate methylene groups, 0.251 nm, is only 2% longer than the 0.246 nm spacing between these hollows. This arrangement would be energetically favourable if the decrease in potential energy obtained by the fit of the hydrogen atoms on the hexagon centres would compensate the increase in energy of the molecules due to contraction.

With the advent of STM, it became possible to observe organic molecules adsorbed on conducting surfaces and the ordering of alkane layers on graphite was revealed. Alkanes are non-conducting, but for one or a few layers of material deposited on a conductive substrate, a sufficient current flows to the tip, allowing the use of this technique. Moreover, since the molecules alter the tunnelling current, the images of organic molecules usually show a combination of features corresponding to the molecules and the substrate. The contribution from each of them will depend on the strength of such alteration which can occur either by a change in the tunneling barrier or by modification of the density of states in the tip due to the interaction with the molecules.

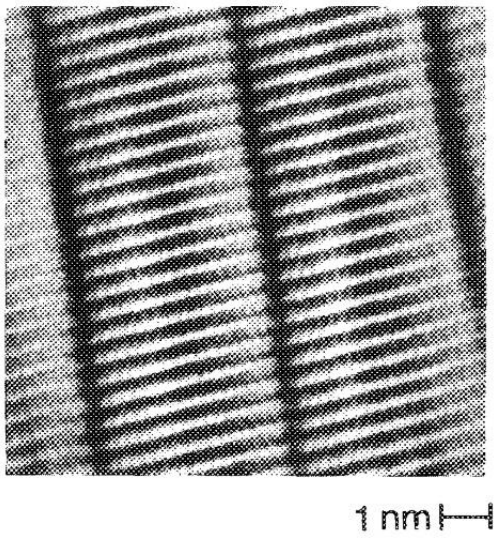

Figure 2.16: First STM image of alkane molecules adsorbed on graphite corresponding to dotriacontane ($C_{32}H_{66}$). Extracted from [91].

McGonigal et al, took for the first time STM images of alkanes, in this case triacontane n-$C_{32}H_{66}$, adsorbed from a solution of 10ml of iso-octane on graphite[91] (Fig 2.16). The images agree with the model proposed by Groszek although they are not sufficient to confirm that the molecules are oriented in an all-trans configuration. The molecules appear arranged parallel to each other and perpendicular to the troughs beyond their ends, forming lamellar rows with an structure similar to those formed by alkane molecules in their three dimensional crystal[92]. Across these troughs between rows, neighbouring molecules are offset by half the lateral distance between parallel molecules, in a manner such that their endings are interdigitated. Authors argue that the molecules are commensurate with the substrate, since otherwise a more irregular image due to "aliasing effects" caused by the differing periods of the substrate and adsorbate lattices would be expected.

Later images of heptacosaene ($C_{27}H_{56}$) on graphite show indeed a varying contrast along the molecules with one of the extremes being brighter than the other[93] (Fig 2.17.a). This has been attributed to similar *but not exact* distances between methylene groups and graphite hexagons, resulting in a modulation of the tunnelling current. However, along the lamellar rows, the molecules seem to be commensurate with the substrate since no contrast variation is appreciated in such direction.

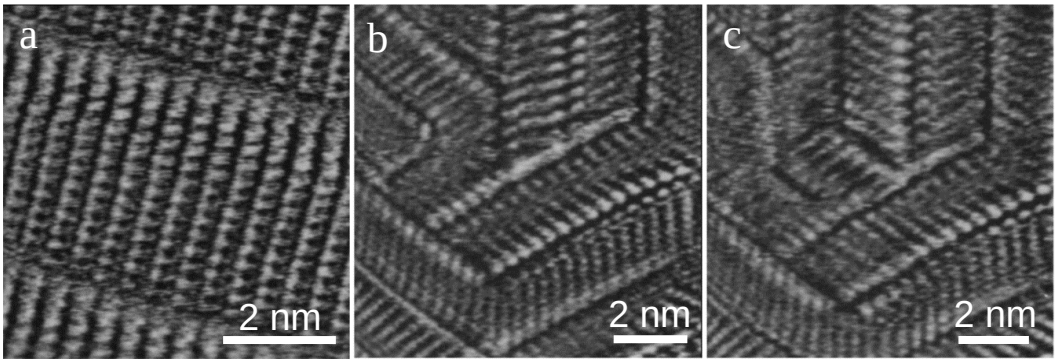

Figure 2.17: STM images of molecular monolayers on the basal plane of graphite. a) The alkane heptacosane ($C_{27}H_{56}$) presents a contrast variation in the direction of the molecule. The ends of the molecules on the upper side of the molecule look slightly brighter than the opposite sides due to a slight mismatch between methyl groups and the hexagon centres of graphite. b-c) Lamellar rows of octadecanol ($C_{18}H_{37}OH$) where the molecules change orientations on the left corner. Image (c) was taken 10 ms after (b). Images extracted from [93].

Alkanes on graphite seem to align perpendicularly to the lamellar row. However, other organic molecules with functional groups show different behaviour. In the case of alcohols such as octadecanol ($C_{18}H_{37}OH$) the molecules are tilted ~30° with respect to the lamellar row direction instead of lying perpendicularly to it (Fig 2.17b and c). The orientation of the molecules alternates often although not always between different rows resulting in a herringbone structure. The orientation of the molecules with respect to the lamella can switch between AFM scans. Even the domains of the lamellar rows can take over other domains. Figures 2.17 b and c in the top left corner reveal this kind of behaviour.

High resolution images of individual molecules show in detail a number of topographic features in a zig-zag configuration along the length of the alkanes[94]. The number of these features loosely matches the number of carbon atoms in the chain, which is consistent with the molecules lying in an all-trans configuration. Nevertheless, the angles and distances between bright features do not coincide with those expected to carbon atoms in the alkane chain. Instead, they match more probably orbitals of the top hydrogen atoms of alkanes. Also, the brightness of these spots is considerably stronger on one side of the molecule than in the other. This asymmetry has been for many years a source of debate where some authors suggested that the molecules lie with the molecular axis perpendicular to the substrate[93] or tumble back and forth between these orientations[95] instead of lying parallel[91].

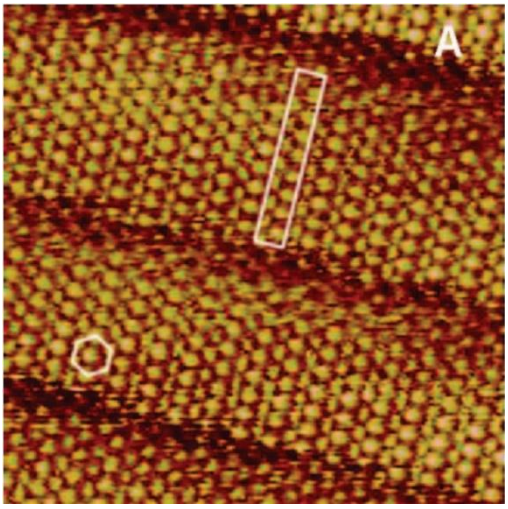

Figure 2.18: STM image of nonadecane ($C_{19}H_{39}$). The white box indicates the location of an individual molecule. Bright features correspond to methylene groups. Extracted from [94].

In order to shed light on this controversy, a series of theoretical studies where performed. Faglioni et al. developed a model based on perturbation theory in which computed STM images of octane with the molecular axis parallel and perpendicular to the surface of HOPG where produced[96]. The results show that the parallel configuration computed STM images (Fig 2.19b) are very similar to those obtained experimentally as opposed to the perpendicular configuration images (Fig 2.19a).

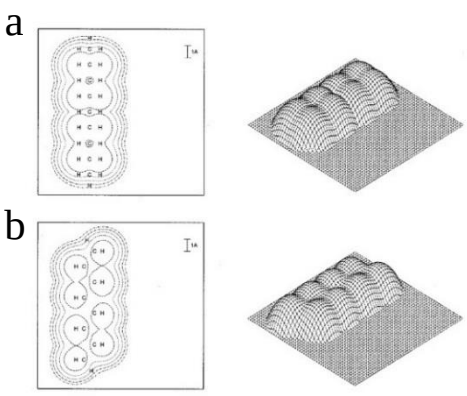

Figure 2.19: Computed STM images of an alkane molecule adsorbed with its molecular axis perpendicular (a) and parallel (b) to the graphite surface. The contour levels are at 1/6, 2/6, 3/6, 4/6, and 5/6 of the maximum height peak of each plot. Extracted from [96].

A*b initio* calculations[97] as well as molecular simulations of alkanes on HOPG[98,99] indicate that the most stable configuration corresponds to the all-trans. Intuitively, this configuration should be preferable, since the number of atoms closer to the surface, specially carbon atoms, is larger than in the perpendicular configuration. In addition, the second molecular simulation study explores the contribution of intermolecular forces, concluding that although the interactions between molecules are stronger in the case of the molecules lying perpendicular to the surface compared to lying parallel, the interactions with the substrate are stronger being the determinant factor. Nevertheless, the molecule-molecule interactions play a significant role in the formation of the lamellar structures.

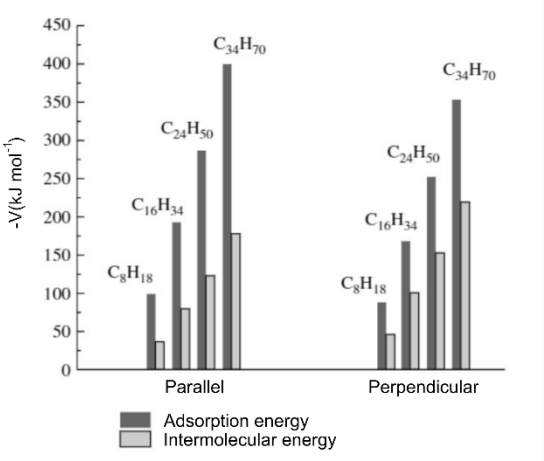

Figure 2.20: Adsorption and intermolecular energies for long chain alkanes adsorbed on graphite. Extracted from [99].

Ilan et al. performed first principles calculations based on density functional theory (DFT) showing that the asymmetry in the intensity between features at opposite sides of the alkanes can be induced by coupling of the frontier orbitals of the molecules with the orbitals of the carbon atoms in the graphite lattice[94] (Fig 2.21). Since the states near the Fermi level in graphite are dominated by π electrons on the B type carbon, the coupling depends on the registry of the molecules. Previous STM images of graphite show a marked difference in contrast between the two sublattices A and B, where A is the sublattice that has neighbours above and below and the B lattice lies above and below hexagon centers[100]. Since the STM images are insufficient to identify which sublattice corresponds to the higher contrast, theoretical calculations were used to determine the contribution from the Bloch wave functions corresponding to each sublattice to the states near the Fermi level that are scanned by the STM tip.

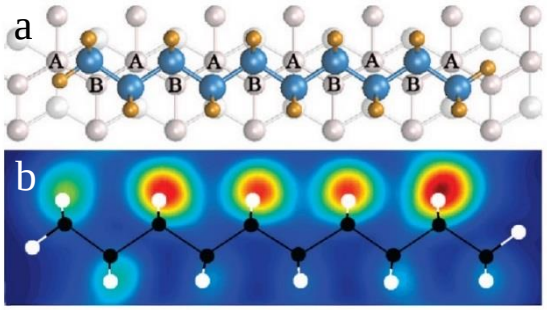

Figure 2.21: A relaxed decane molecule on graphite and its corresponding simulated STM image in an all-trans configuration on two layers of graphite. Extracted from [94].

The adsorption from solution into HOPG of a binary mixture of alkanes with different lengths, hexacosane ($C_{26}H_{54}$) and tetratriacontane ($C_{34}H_{70}$), have been investigated using STM[101]. Results are shown on Fig 2.22. Even in solutions with much higher

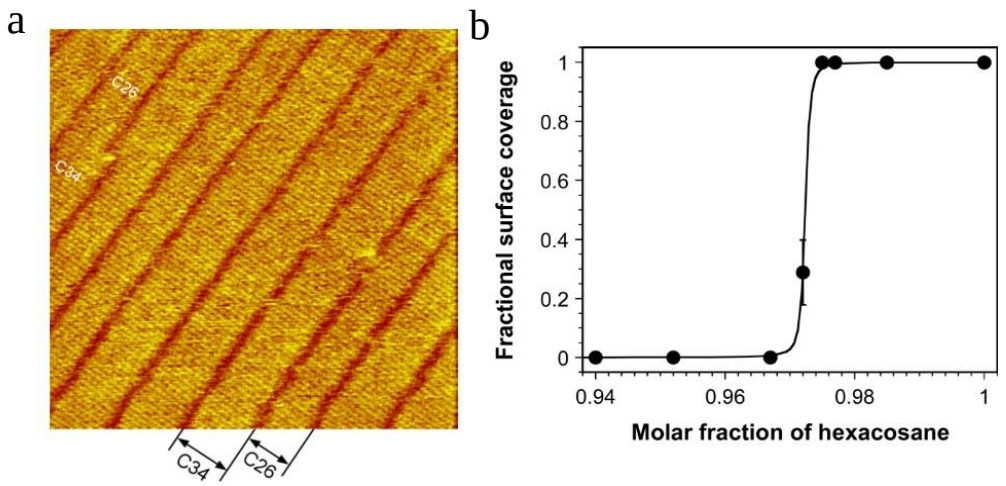

Figure 2.22: a) STM image of hexacosane ($C_{26}H_{54}$) and tetratriacontane ($C_{34}H_{70}$) molecules adsorbed onto the HOPG surface from a mixed binary solution. The STM image was obtained at 0.972 molar fraction of hexacosaene. The image area is 30 × 30 nm2. b) Fractional surface coverage of hexacosane, the shorter alcane, vs molar fraction in solution of hexacosane. The graph indicates a preferential adsorption of the longer alkane. Adapted from [101].

concentrations of the shorter alkane compared to the longer alkane, the adsorption of the longer alkane is preferred. This is due to the difference in the free energies of exchange between the surface and the solution, of the two alkanes, which as mentioned before, increase with the number of methylene groups. When the molar fraction of the shorter alkane reaches a certain threshold value, close to one, a sharp transition occurs and the longer alkane is rapidly displaced by the shorter alkane, leaving the surface almost exclusively covered by the later. These results agree with previous studies of adsorptions of binary mixtures of other alkanes on graphite[102–104].

The evolution of the morphology and orientation of alkane layers deposited by physical vapor deposition at various substrate temperatures has also been studied[105]. Alkanes of different lengths were used including hexacontane. Since alkanes have higher melting points and interact more strongly with the substrate as the number of

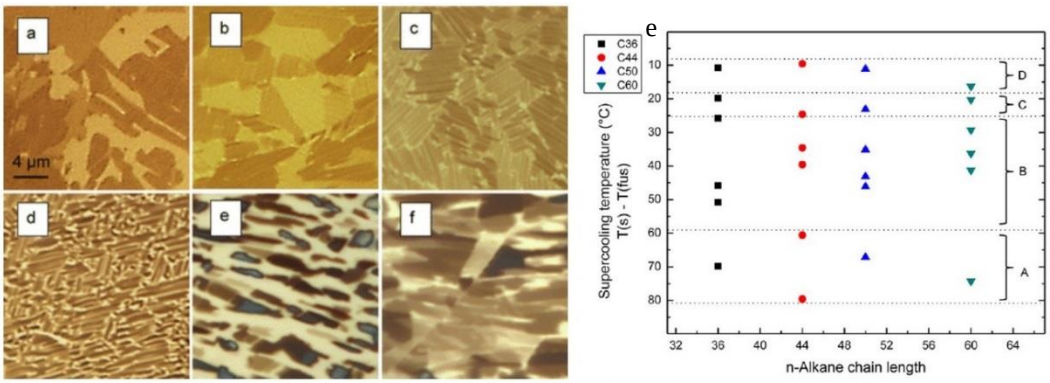

Figure 2.23: a-f) Polarized optical microscopy images of hexacontane grown at increasing substrate temperatures showing different phases e) Classification of the phases formed by the different alkanes depending onT_{SC} (temperature relative to melting point) : (A) epitaxial domains of uniform thickness; (B) rod-like domains reflecting surface symmetry; (C) pseudorectangular domains with no epitaxial order; (D) normal oriented domains. Extracted from [105].

methylene groups in the chain is increased, a supercooling temperature (T_{SC}) is used as a reference for the different alkanes. This temperature is defined as the difference between the melting point (T_{fus}) and the substrate temperature (T_S): $T_{SC} = T_{fus} - T_S$. The structures formed by the alkanes used in this study is compared showing that different alkanes behave similarly for close supercooling temperatures. Polarized optical microscopy images of hexacontane ($T_{fus} = 95$ °C) are displayed on Figs 2.23a-f. At lower substrate temperatures $T_S = 25$ °C in Fig 2.30a, the molecules form a film of uniform thickness with domains of different contrast that reflect the six-fold symmetry of graphite as expected for alkanes adsorbed with their molecular axis parallel to the substrate surface. As the temperature of deposition is increased, in Figs

2.23b-d: $T_S = 58$ °C, $T_S = 63$ °C and $T_S = 70$ °C, narrow rod-like structures are formed in the direction of the lamellae. These structures are formed by molecules piled up on each other with their molecular axis parallel to the surface. Also, the size of the domains tends to increase as a result of increased mobility during deposition, although in the case of hexacontane this trend is not really appreciable. At $T_S = 79$ °C in Fig 2.23e, a pseudorectangular phase is observed which shows no epitaxial order. Near edge X-ray absorption fine structure spectroscopy (NEXAFS) indicates that in this phase the molecules are still oriented in parallel to the surface despite the lack of epitaxial order. The interaction with the substrate at this point is relatively weak. Finally, at $T_S = 83$ °C, in Fig 2.23f, approximately 10 °C under the melting point, the molecules are oriented normal to the surface, as NEXAFS results indicate. At this point the interaction with the surface is too weak to maintain the alkanes parallel to the surface and they adapt to a more thermodynamically stable orientation.

AFM can be used to study the confinement of alkanes between two solid surfaces, which is relevant in lubrication applications. Figure 2.24 shows combined force and conduction curves of a conducting AFM tip approaching and pulling off of a graphite surface with a monolayer of different alkanes[106]. The monolayer can be squeezed out of the contact area during the approach of the tip to the surface, provided that the molecules are in an ordered state below their melting transition temperature. In contrast, when the molecules are in a disordered state above such temperature, a few molecules are trapped within the tip-surface contact zone. This phenomena is explained by the coupling between molecules that allows them to be removed from the surface as a rigid layer.

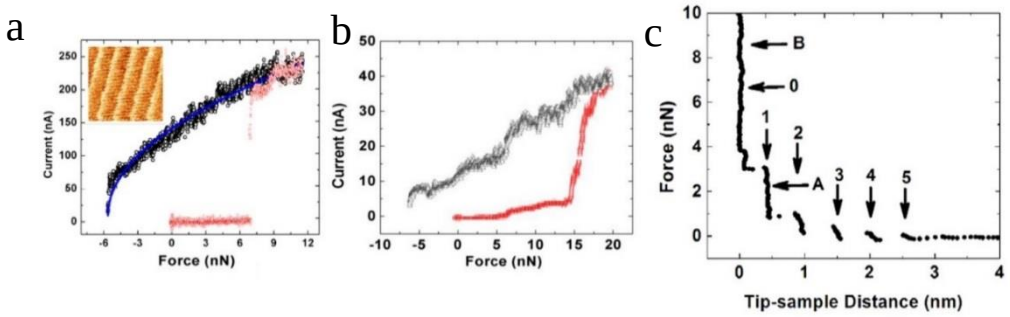

Figure 2.24: a) Current vs force curves during approach (red dots) and and pull-off for a monolayer of hexadecane on HOPG at 25 °C showing a sharp jump in current when the molecules are squeezed out of the surface. b) Same as (a) but at 65 °C. The irregular behaviour of the current indicates that the molecules are trapped between the tip and the surface. c) Force vs Tip-sample distance for 5 layers of hexadecane at 25 °C. The jumps indicate the force at which each layer is removed. Adapted from [106].

Few molecules thick layers of hexacontane $C_{60}H_{122}$ deposited on graphite were examined with AFM by heating the sample and the AFM tip during scanning at temperatures between 25 °C and 150 °C[107]. Figure 2.25 shows lamellar structures with a period of 7.5 nm matching the length of the molecule. This implies that, as expected, the alkanes are oriented perpendicularly to the lamella. A correlation between the molecular alignment and the 3-fold symmetry of the graphite lattice is indicated by domains with lamellar orientations that differ by 60 ° (Fig 2.25b). Also, the periodicity and orientation of the lamella is preserved in areas with several layers of molecules, in this paper labelled as nanocrystals. These nanocrystals are an example of homoepitaxy where the growth of additional layers is patterned by lower ones. A series of images taken between 25 °C and 150 °C show that the heights of the nanocrystals begin to decrease at 90 °C. In particular, a nanocrystal that at 80 °C and lower temperatures has a height of 2.8 nm is found to be 0.5 nm high at 90 °C. At 100 °C there are no nanocrystals found on the surface although the lamellar structures of the epitaxial layers are still observable. Further heating at 130 °C induces changes in the lamellar orientation between consecutive images. At 145 °C the lamella is finally no longer observable. This temperature is ~50 °C higher than the melting temperature of bulk hexacontane. When the temperature is lowered to 140 °C the epitaxial order is restored, although the orientation of the lamella in some domains has changed.

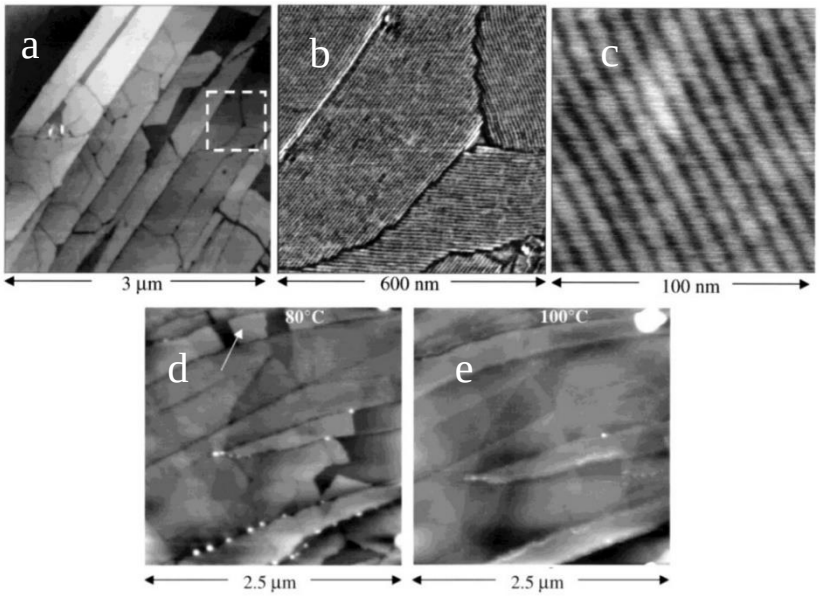

Figure 2.25: a) AFM topographic image of a graphite surface after deposition of hexacontane. b) AFM phase image of the area marked with a square on (a) showing three different lamellar orientations differing by 60°.c) Topographic image showing the lamellar rows in detail. (d-e) Topographic images showing the height of nanocrystals formed by several layers of hexacontane molecules. Arrow indicates one of these nanocrystals with a height of 2.8 nm at 80 °C in (d) being no longer visible at 100 °C in (e). Extracted from [107].

3. Experimental techniques

3.1 hBN Substrate preparation

Sapphire, which has a melting point of ~2050 °C was used a support substrate for hBN exfoliated flakes in the growth of graphene by MBE growth, while SiO_2/Si was used for hexacontane deposition on hBN at room temperature. In the case of graphene growth, the substrates were 1 cm square double-sided polished sapphire (0001) substrates (SurfaceNet GmbH) while for the deposition of hexacontane we used SiO_2 /Si 5x5 mm^2 wafers. hBN flakes were obtained by mechanical exfoliation from high-temperature high-pressure hBN crystallites[108].

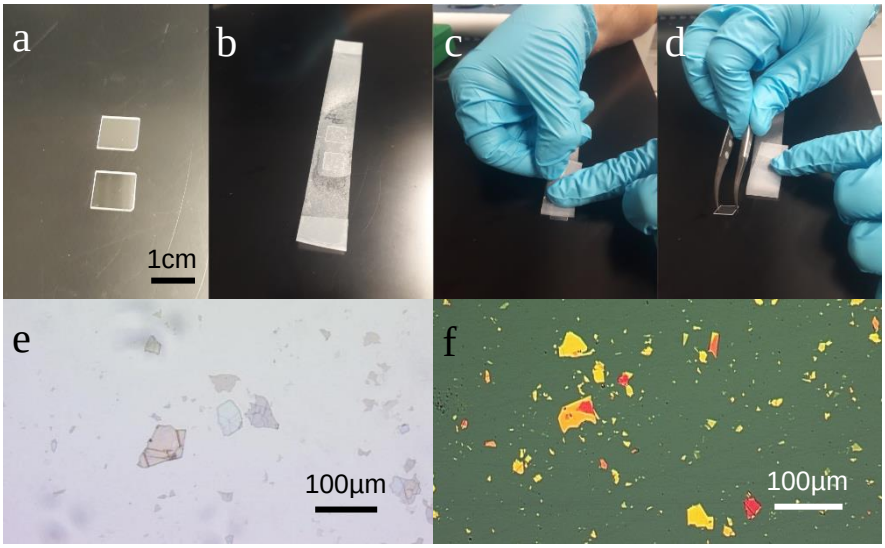

Figure 3.1: Sequence of images of transfer of mechanically exfoliated hBN flakes onto sapphire wafers. a) Samples are arranged on the table. b) Tape with hBN flakes is placed on the samples. c) Gentle removal of the tape. d) Sample ready to go into furnace. e) Optical microscope image of hBN flakes on a sapphire wafer. f) Optical microscope image of hBN flakes on SiO_2/Si wafer.

During the exfoliation process, a few of these crystallites are sprinkled into a low tack PVC with acrylic adhesive tape (Loadpoint Ltd) and the tape is folded into itself in a way that the crystallites are trapped between two adhesive surfaces. Then, the tape is unfolded and the crystallites are cleaved. Since the hBN layers are bound by weak van der Waals forces, the cleavage tends to occur in along these planes, despite the random orientation of the crystallites when initially placed on the tape. The process is repeated several times putting in contact the adhesive with itself at slightly different areas each time in order to extend evenly the flakes over the whole tape.

Then, a few support substrates are arranged on a line and the scotch tape is placed on top of them leaving the flakes in contact with the adhesive surface. We make sure that the adhesive and the sample surfaces are in contact by gently pressing with a finger on top of the tape. Notice that the tape is also in contact with the table. Once this is done, we start to peel off the tape with one hand while with the other we use tweezers to hold the samples on the table.

The typical lateral dimensions of the flakes range between 10 and 100 μm while the thicknesses is around a few hundreds of nanometres. Once the flakes were transferred, the samples are cleaned overnight by immersion in toluene (99.9% Chromasolv for high performance liquid chromatography, Sigma-Aldrich), followed by heating at 400 °C for 8 h in a flow of 0.15 sL/min of Ar/H_2 (95:5). Figure 3.1e shows an optical micrograph of a sapphire substrate with hBN flakes after the cleaning process. The apparent colour of the flakes is due to thin film interference. In the case of hexacontane deposition, the substrates were flame annealed before introduction in a UHV chamber for sublimation deposition or before submersion in solution, in order to remove undesirable adsorbates from the surface.

3.2 Hexacontane deposition by sublimation

Hexacontane deposition was carried out at a 10^{-7} Torr pressure by sublimation from a resistively heated a Knudsen cell at ~200 °C. Such high temperature of sublimation is a consequence of the great length of the hexacontane molecule. No heating was applied on the substrate during deposition. The layer thickness was determined using a quartz thickness monitor which was calibrated from the surface coverage of the dendritic structures formed by hexacontane on SiO_2.

3.3 Hexacontane deposition by immersion

Hexacontane was also deposited onto hBN by immersion in a vial with a solution of 10 μg/ml hexacontane/toluene under standard conditions during 1 minute. The sample was blown dry with a N_2 gun after removal from the solvent.

3.4 High temperature MBE graphene system

The MBE system used in this work, shown in Figure 2.2, is based on a Veeco Gen Xplor MBE system, with a modified substrate holder in order to allow growth temperatures up to 1850 °C, much higher than the typical substrate growth temperatures used in MBE (~1000 °C). The system is composed of two chambers, one to grow graphene and the other dedicated to the growth of hBN. This thesis focuses on the samples grown in the former.

The growth of graphene using MBE is in principle simpler than the growth of other crystals like hBN, or AlGaAs given that there is only one source material needed, in this case carbon. The optimal growth conditions are found by exploring the time of growth, the substrate temperature and the beam flux.

After the exfoliation process described in section 3.1, samples were transferred onto a tantalum sample holder and introduced into the MBE system where they were annealed before growth at 800 °C during 1h. The substrate temperature during growth was estimated using a thermocouple positioned behind the substrate heater, given that the transparent sapphire substrates used as a support for hBN flakes prevent the use of a pyrometer. The growth of graphene on hBN was explored in this work with three different types of carbon sources: a filament source, an atomic carbon source and an e-beam source.

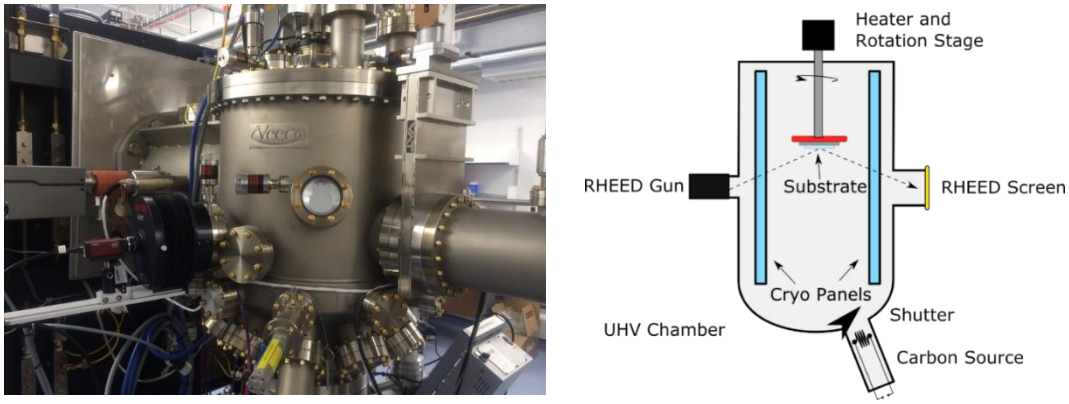

Figure 3.2: a) Photograph of the MBE system used in this work. b) Scheme showing the disposition of the different elements inside of the chamber.

In order to roughly calibrate the sources, carbon layers were grown on sapphire[109]. These layers are weakly attached to the sapphire substrate and can be easily removed with clean plastic-tip tweezers without damaging the substrate. By scanning with an AFM on the edge of the region where the material has been removed, we can measure the thickness of the layer. The amount of carbon deposited on sapphire is significantly lower than on hBN due to the higher mobility and lower sticking coefficient of carbon on hBN. Nevertheless, hBN is a surface free of dangling bonds, so the growth of graphene relies on nucleation points at defects or step edges which can vary from hBN flake to hBN flake.

3.5 Atomic Force Microscopy

Scanning tunnelling microscopy, the forerunner of atomic force microscopy was developed in 1982 by Gerd Binnig and Henrich Roher at IBM Research-Zurich[110,111]. Their invention earned them the Nobel prize in 1986. The operation of STM is based on a phenomenon known as quantum tunnelling effect which was first noted by Friedrich Hund in 1927 while calculating the ground state in a double well potential. When an electron encounters a potential barrier with an energy higher than its kinetic energy, the probability of finding the electron at the other side of the barrier, and in turn the electric current associated (tunnelling current), decrease exponentially with the width of the barrier. This is a consequence of the wave behaviour of the particle in contrast with the classical analogue where particles can only overcome barriers with energies below their kinetic energy. The relationship between such barrier width and the tunnelling current is so sensitive that an increase of 0.1 nm on the width implies a decrease of one order of magnitude in such current. The STM technique exploits this phenomenon by approaching an atomically sharp metal tip to the surface of study, which must be either a metal or a semiconductor. The barrier consists of the physical gap between the tip and the substrate. A voltage difference is applied between the tip

and sample so electrons tunnel from one to another. Figure 3.3 illustrates the wave-function of an electron as it tunnels through the potential barrier of vacuum.

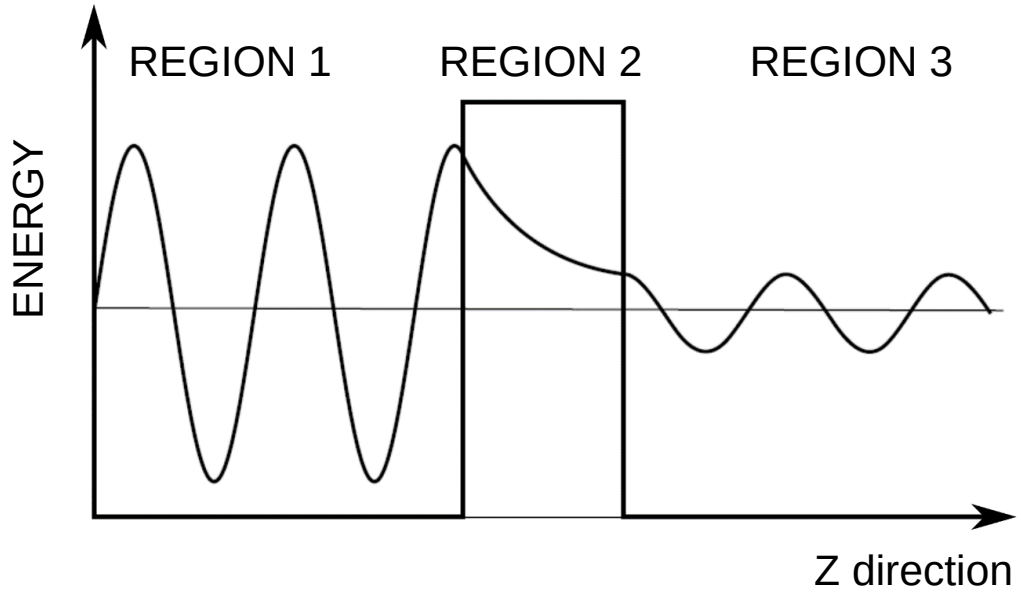

Figure 3.3: Diagram showing the tunnelling of an electron wave through the potential barrier of vacuum. The exponential decrease of the wave can be observed in the barrier.

The 1D time-independent form of the Schrodinger equation can be used to describe this phenomenon.

$$\hat{H}\psi(z) = -\frac{\hbar^2}{2m}\frac{d^2}{dz^2}\psi(z) + V(z)\psi(z) = E\psi(z) \tag{3.1}$$

The wave functions in the three regions can be represented as a superposition of waves moving from left to right and right to left:

$\psi_1 = Ae^{ikz} + Be^{-ikz}$

$\psi_2 = Ce^{-\mu z}$

$\psi_3 = De^{-ikz} + Fe^{ikz}$

with $\mu = \sqrt{2m(E - V_0)/\hbar^2}$ and $k = \sqrt{2mE/\hbar^2}$

Since the probability of tunnelling is defined as the ratio between the probability fluxes between the transmitted and incident waves:

$$I \propto T = \frac{|F|^2}{|A|^2} \propto e^{-2\mu a} \tag{3.2}$$

This shows that the tunnelling current decreases exponentially as the width a of the barrier increases.

Further analysis of the tunnelling current first by Bardeen[112] and later by Tersoff and Hamann[113] takes in consideration the density of states of the tip and the sample. This model shows that the topography observed can depend strongly on the local density of states (LDOS) at the Fermi level of the surface at the position of the tip.

The STM tip is mounted on a tube composed of a series of piezoelectric crystals that extend or contract when a voltage is applied on them, controlling the position of the tip. Given that the relationship between the extension and the voltage applied is linear the piezos are previously calibrated using a surface grid with known dimensions. A group of piezos control the movement in the x-y plane while another controls the position of the tip in the z coordinate. Typically, the tip scans the surface through a series of horizontal adjacent lines. In the most common mode of operation (constant current) a feedback loop adjusts the extension of the z piezo in a way that the tunnelling current will be kept constant. The magnitude of the current is referred to as the set point. By expanding and contracting the z piezo, the separation of the tip with respect to the surface i.e. the width of the tunnel barrier is kept also constant, as long as the conductivity of the surface is uniform. This way, while the x and y piezos move the tip across the surface, the z piezo expands and contracts maintaining this separation constant. The z height of the tip as well as its position on the x-y plane are recorded while scanning. The computer software then associates a colour brightness to each pixel proportionally to the z height. This forms an image where the brighter pixels correspond to higher positions.

In 1986 Gerd Binnig, Christoph Gerber and Calvin Quate invented the atomic force microscopy (AFM)[114] which, as opposed to STM, can be used on all types of surfaces including insulators. AFM relies on the interaction forces between the surface and an atomically sharp tip mounted on a flexible cantilever. In general, these forces are a combination of Pauli repulsion and attractive van der Waals forces. This can be, in general, modelled by a Lennard-Jones potential. Figure 3.4 shows the shape of this potential with the distance normalized in σ units (σ =3.4Å). Equation 3.3 corresponds to this potential. The first term accounts for Pauli repulsion and the second one for long range attractive forces like van der Waals. Also, the parameters ε and σ determine respectively the depth and position of the potential minimum.

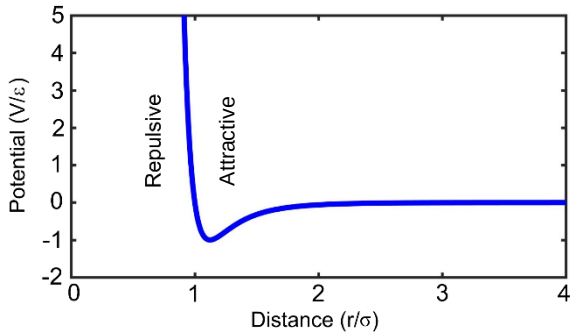

Figure 3.4: Lennard-Jones potential indicating the repulsive and attracting regimes.

$$V(r) = 4\epsilon\left(\left(\frac{\sigma}{r}\right)^{12} - \left(\frac{\sigma}{r}\right)^{6}\right) \tag{3.3}$$

AFM allows different modes of operation. The simplest, contact mode uses the force between the cantilever and the surface given that the tip displacement $(z-d)$ is proportional to the force between the tip and the surface following Hooke's law,

$$F(z) = k(z-d)$$

where k is the spring constant of the cantilever. If the tip is at the right (left) side of the dip of the curve in the Lennard-Jones potential, in attractive (repulsive) regime, the cantilever will bend towards (away from) the surface. However, contact mode is typically used in the repulsive regime, since thermal fluctuations place a limit in the minimum spring constant of the cantilever which implies that a stable measurement of force in the attractive regime is very difficult if not impossible.

The deflection of the cantilever is measured by projecting a laser onto the backside of the tip which is often coated with a reflective metal like Al (Fig 3.5a). The laser beam then reflects and hits a photo-detector which is formed by four photo diodes arranged in such a way such that they can detect the horizontal or vertical deviation of the laser, with respect to the original position when the tip is away from the surface and subjected to no force. Figure 3.5b shows a scanning electron microscope (SEM) image of an AFM cantilever with the tip.

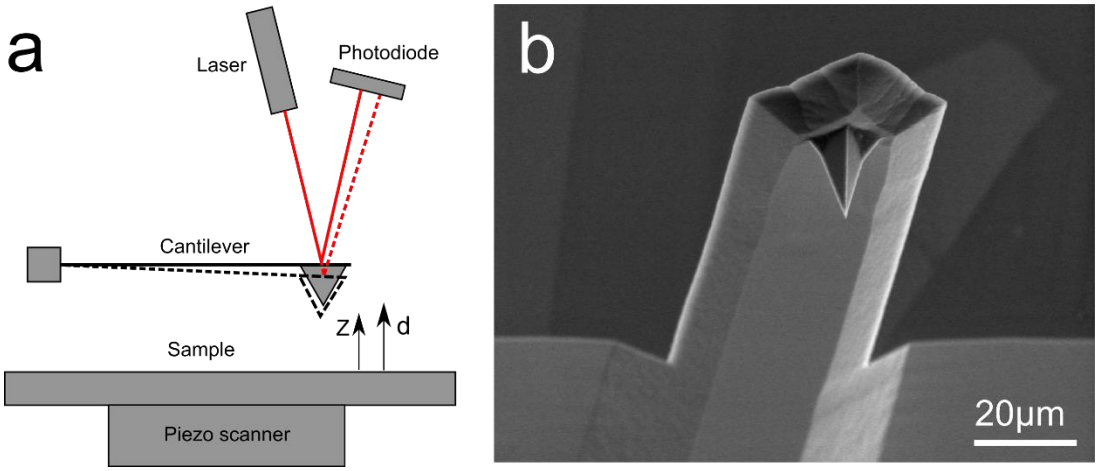

Figure 3.5: a) Schematic drawing of an AFM microscope. b) SEM image of an AFM tip. Extracted from https://ieeexplore.ieee.org/document/6150392.

The deviation of the laser is proportional to the deflection of the cantilever which is in turn proportional to the force applied when in contact with the surface. With this, the same feedback control system used on STM can be used here, with the force applied on the cantilever as a set point instead of the tunnelling current, provided that such force is constant for a particular separation distance.

Contact mode allows to the acquisition of images faster and in some cases with better resolution than other techniques, but it can result in the modification of the tip and the sample. For this reason, is often limited to high resolution scans of small areas of strongly bound materials.

Another scanning mode which is widely used is tapping mode. In tapping mode an extra piezo crystal is used to excite cantilever oscillations at, or close to its resonant frequency. When the cantilever is located far from the surface the amplitude of the

oscillation has a particular value called free-air amplitude. When the tip approaches the surface, the resonance frequency shifts due to the height-dependent interaction force.

The system can be described by the following equation,

$$F_0 \cos(\omega t) + F(z) = m\frac{d^2z}{dt^2} + \gamma\frac{dz}{dt} + k(z-d) \tag{3.4}$$

where the first and second term on the left-hand side account respectively for the external oscillatory driving force supplied by the excitation piezo, with amplitude F_0 and the van-der-Waals force of interaction between the tip and the sample. On the right-hand side of the equation we have (from left to right) the response of the cantilever, the damping force, with damping constant γ and the restoring force of the cantilever.

The amplitude of the cantilever oscillation and the phase shift between the cantilever and the piezo for a given drive frequency ω are given by,

$$A(\omega) = \frac{F_0}{k}\frac{\omega_0^2}{[(\omega^2-\omega_0^2)^2 + \left(\frac{\omega\omega_0}{Q}\right)^2]^{1/2}} \tag{3.5}$$

$$\varphi(\omega) = tan^{-1}\left(\frac{\omega\omega_0/Q}{\omega_0^2-\omega^2}\right) \tag{3.6}$$

where, ω_0 is the resonant frequency of the cantilever, k is the spring constant and F_0 is the amplitude of the driving force. The quality factor,

$$Q = {}^{k}/_{\omega\gamma}$$

is related to the width of the resonant peak of the cantilever. The narrower the peak, the higher Q. For small oscillations around the equilibrium position, we can substitute z by z_0 + z_1(t), and with this, expand F(z) around the equilibrium,

$$F(z) = F(z_0) + z_1(t)\frac{dF}{dz} \tag{3.7}$$

Substituting into equation 3.4 we obtain,

$$F_0\cos(\omega t) + F(z_0) + z_1(t)\frac{dF}{dz} = m\frac{d^2z_1(t)}{dt^2} + \gamma\frac{dz_1(t)}{dt} + k(z_0 + z_1(t) - d)$$

Since $F(z_0) = k(z_0 - d)$,

$$F_0\cos(\omega t) = m\frac{d^2z_1(t)}{dt^2} + \gamma\frac{dz_1(t)}{dt} + \left(k - \frac{dF}{dz}\right)(z_1(t)) \tag{3.8}$$

This gives us,

$$k_{eff} = k - \frac{dF}{dz}$$

$$\omega_1(z) = \sqrt{\frac{k_{eff}}{m}} = \sqrt{\frac{k}{m}}\left(1 - \frac{dF}{kdz}\right)^{1/2} \approx \omega_0 - \frac{w_0}{2k}\frac{dF}{dz} \tag{3.9}$$

Therefore, the angular resonant frequency shift obtained is,

$$\Delta\omega_0 = -\frac{\omega_0}{2k}\frac{dF}{dz} \tag{3.10}$$

This assumes that the amplitude of the oscillation is small and that k >> $\frac{dF}{dz}$.

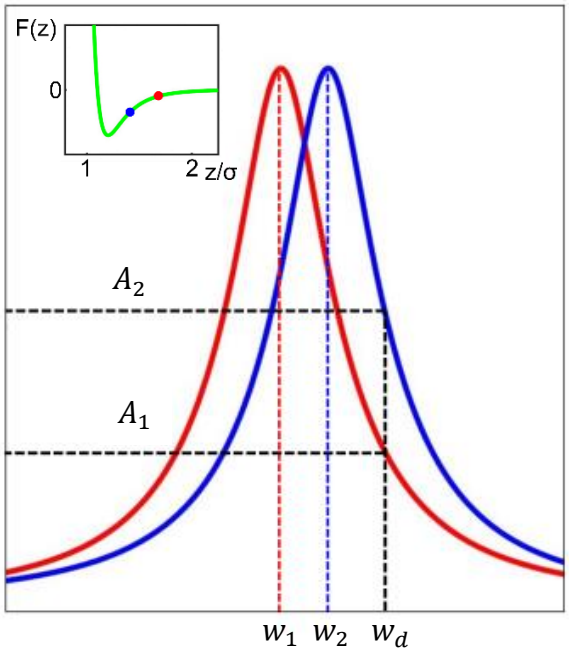

Figure 3.6: The resonant frequency is shifted by the tip surface interaction. The shift is proportional to the variation of the interaction force with the distance.

The driving force from the piezo can be set to a frequency close to resonance. As the cantilever gets closer to the surface, since the gradient of the force changes, there is a shift in the resonance peak, which in turn changes the oscillation amplitude of the cantilever. For the choice in drive frequency on Fig 3.6 the amplitude decreases as the tip approaches the surface until it matches a certain value previously introduced (set point). During the scan the

distances between the cantilever and the surface momentarily change, which in turn change the gradient of the force and the amplitude of oscillation. A feedback loop adjusts the height in order to match the oscillating amplitude. Figure 3.6 shows schematically to resonance peaks corresponding to two different heights. The inset shows their corresponding position in the force curve.

Tapping mode was the main technique used during the development of this thesis. The fact that this mode is performed without contact on the surface allows a higher stability of the tip as well as less wearing of the surface. All AFM measurements (unless stated otherwise) were performed in amplitude-modulated tapping (AC) mode with an Asylum Research Cypher-S AFM and an Asylum MFP-3D AFM using Multi75 Al-G AFM probes (Budget Sensors) at set points between 400mV and 600 mV (free-air amplitude normalized to 1V) in ambient conditions (k ~3 Nm^{-1}, ω_0=75 (60-90) kHz).

Conductive AFM (cAFM) is a different mode in which a metal tip scans in contact with the surface, while a voltage difference is applied between the two. The current that flows through the sample and the tip is measured during scan, generating an image where the areas with different magnitude of conductance can be distinguished. This technique was used to measure the surface conductance at different areas along the Moiré unit cell. Fig 3.7 shows a scheme of the set up. In order to supply a bias voltage on the graphene layers a gold electrode was formed on the sapphire substrate by resistive thermal evaporation and silver nanowires were deposited onto the surface. The deposition was calibrated so the density of nanowires was enough to form a conductive path for the current to flow from the electrode to the graphene layers on top of hBN flakes but leaving enough space between them so the surface could be scanned. These conductive measurements were taken by James Thomas from the University of Nottingham.

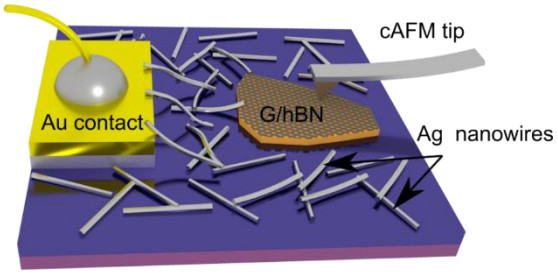

Figure 3.7: Experimental set up for cAFM. Ag nanowires were deposited onto the surface in order to stablish a conductive path between the graphene layer on hBN and the gold contact. The gold contact was evaporated using a mask.

4. Graphene growth on hBN using a carbon filament

In this chapter graphene growth using a SUKO-63 carbon filament source supplied by Dr. Eberl at MBE-Komponenten GmbH was investigated. The carbon source consists of a looped filament made of pyrolytic graphite. Sublimation of carbon is achieved through resistance heating to temperatures up to 2300 °C.

These sources were developed for the growth of Si-C and Si-Ge-C alloys in Si MBE, but in the last few years have been successfully applied to graphene growth and can provide a stable flux at low deposition rates. In order to avoid contamination of undesirable species, the heater assembly is constructed from pyrolytic graphite (PG) parts. In addition, internal water cooling of the electrical contacts avoids overheating of these parts.

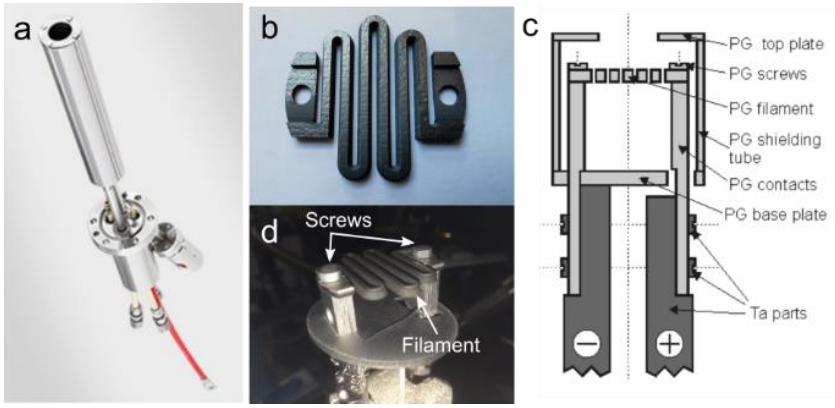

Figure 4.1: a) Photograph of the flange of the carbon filament source. b) Photograph of the filament source. c) Schematic of the source inside the flange. d) Photograph of the filament attached to the SUKO assembly. Images (a) and (d) are extracted from: https://www.mbe-komponenten.de .

In Figure 3.1a a photograph shows the flange inside which the filament source is located. The arrangement of the different elements is shown schematically in Fig 4.1c. An image of the filament attached to the system is also shown in Fig 4.1d. The filaments have an average life of 20 hours at a current of ~100A. In order to obtain full coverage, the time of growth was fixed to 4 hours for each sample. Partial growth was discussed by Summerfield et al[64].

4.1 Monolayer growth

The growth of a monolayer of graphene on hBN is achieved usually at substrate temperatures above 1500ºC. Lower substrate temperatures typically result in hBN flakes completely covered in amorphous carbon. Figure 4.2 shows a series of optical microscope and AFM images of flakes completely covered in graphene.

An image of the whole wafer was acquired using a composite of optical microscope images (Fig 4.2a). Bottom right and bottom left corners of the wafer are cut in order to identify the orientation of the sample as well as the "up-side" covered in flakes. The dark colour is due to the carbon deposited on sapphire all over the surface of sample except on the corners where the clips of the substrate holder are attached during growth. The flakes correspond to the brighter small objects scattered around the surface. The blue box marks the area where the image in Fig 4.2b was taken. Most of the hBN flakes have dimensions that range from 10 μm to 100 μm. Their different colours are due to the light interference which is dependent on the thickness of the flakes.

Figures 4.2c and d show an optical microscope and a topographic channel AFM image of the flake highlighted by a blue box in Fig 4.2b. Wrinkles running along principal axes, which are due to thermal cycling during growth are present on both images. Blue boxes indicate where each subsequent image was obtained. In Fig 4.2e the wrinkles previously mentioned can be resolved more clearly (see green arrow). Flakes also show folds due to the rugosity of the underlying sapphire substrate. Amorphous carbon deposits are accumulated on step edges forming lines that run along several micrometres. One of these lines is indicated by a magenta arrow in the same image. Carbon deposits also accumulate on hBN defects. These appear as higher contrast dots (yellow arrow in Fig 4.2f). The presence of carbon deposits, for example on step edges seems to play a role in the preservation of strain in the graphene layer as discussed later. Figures 4.2g and h correspond to topographic and phase channel images from a scan in the area marked with a blue rectangle in Fig 4.2f. A fold runs diagonally close to the top right corner on both images. Also, amorphous deposits lie on the right-hand side.

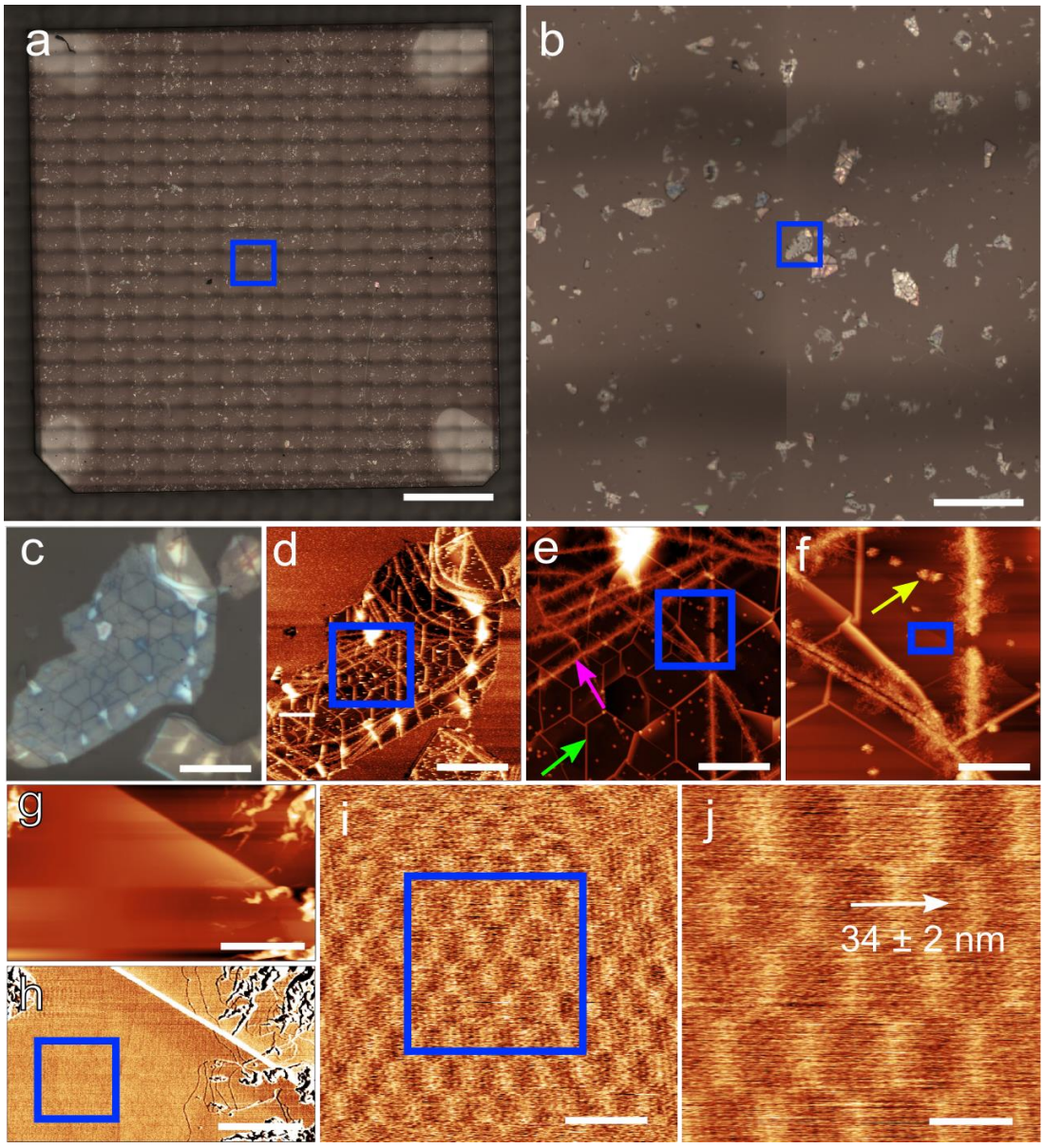

Figure 4.2: A series of zoom-in images connect the scale of a sample with the scale of the Moiré pattern. a) Image obtained from a mosaic of optical microscope images of a sapphire wafer covered in hBN flakes after graphene growth. The dark colour of the sample is due to the carbon deposited everywhere except on the edges of the sample under the holder clips. At this scale the flakes look like bright spots. b) Higher magnification image of the hBN flakes with sizes ranging from 10 µm to 100 µm obtained from the area indicated with a blue square in a. Inside the blue square in b lies a flake shown in detail in c (optical) and d (AFM). Both c and d show hBN thermal cycling wrinkles running along the principal axis. The remaining images were all obtained using AFM. e) In addition to the thermal cycling wrinkles (green arrow), carbon deposits lie on the surface on terrace step edges forming higher contrast lines (arrow in magenta). f) There are also present carbon deposits formed on hBN defects. These appear as brighter contrast spots (yellow arrow). Blue rectangle indicates the area scanned on both g (topographic channel) and h (phase channel). Carbon deposits attached to a step edge are located on the right side of both images. An hBN fold runs diagonally. Another blue box in h indicates the area shown in i where the hexagonal Moiré pattern is clearly resolved. i) The topography image is considerably distorted but the hexagonal Moiré pattern can be appreciated. j) Higher magnification topography image gives a slightly better quality. The Moiré periods along the three principal directions are indicated. Scale bars:(a) 2 mm, (b) 200 µm, (c-d) 20 µm, (e) 4 µm, (f) 1 µm, (g-h) 200 nm, (i) 50 nm, (j) 20 nm.

The edges of additional graphene layers emerging from the deposits can be seen on the phase channel image as lines with darker contrast compared to the background. The blue box indicates where the topographic channel image in Fig 4.2i was obtained.

Finally, Fig 4.2i shows a Moiré pattern. The image has been filtered in order to avoid the underlying relief, making the Moiré pattern more obvious. Notice that after such large scans the tip of the AFM is not very sharp, limiting the quality of the images taken in this sequence. A higher magnification image in Fig 4.2j reveals the pattern more clearly. The pattern is formed by lower contrast areas divided by boundaries that form hexagons as the 14 nm period Moiré patterns formed by graphene flakes stacked on hBN or grown by CVD which were discussed in chapter 1. Nevertheless, the periods in the three different directions are close to 34 nm, which is more than twice the value expected for unstrained material. As demonstrated in chapter 1, the relationship between the Moiré period and the strain is given by the expression:

$$\frac{\Delta a_G}{a_G} = \delta \frac{\lambda_s - \lambda_0}{\lambda_s}$$

From this we can calculate the overall strain in this layer to be ~1.1%. Patterns with similar sizes using the same MBE system have been reported previously by the Nottingham MBE graphene group[64]. As explained in chapter 1, Moiré patterns with high periodicities emerge as a consequence of strain within the graphene.

Another flake on the same sample exhibits a regular Moiré patern with a 14.2 ± 0.7 nm period. Figure 4.3a is a 20×20 μm^2 topographic channel image obtained from the centre of the flake. The subsequent images form a sequence of zoom-ins analogous to the sequence in Fig 4.2. All images correspond to the topographic channel except Fig 4.3d which corresponds to phase. Figures 4.3e and f show the Moiré pattern. The path of the profile shown in Fig 4.3g is indicated in magenta. The Moiré pattern has the same morphology but the period in this case is 14.2 nm, approximately the same the period found in stacked aligned graphene/hBN van der Waals heterostructures. The height of the hexagonal wall is ~ 40 pm, similar to the height measured by Summerfield et al[64] previously.

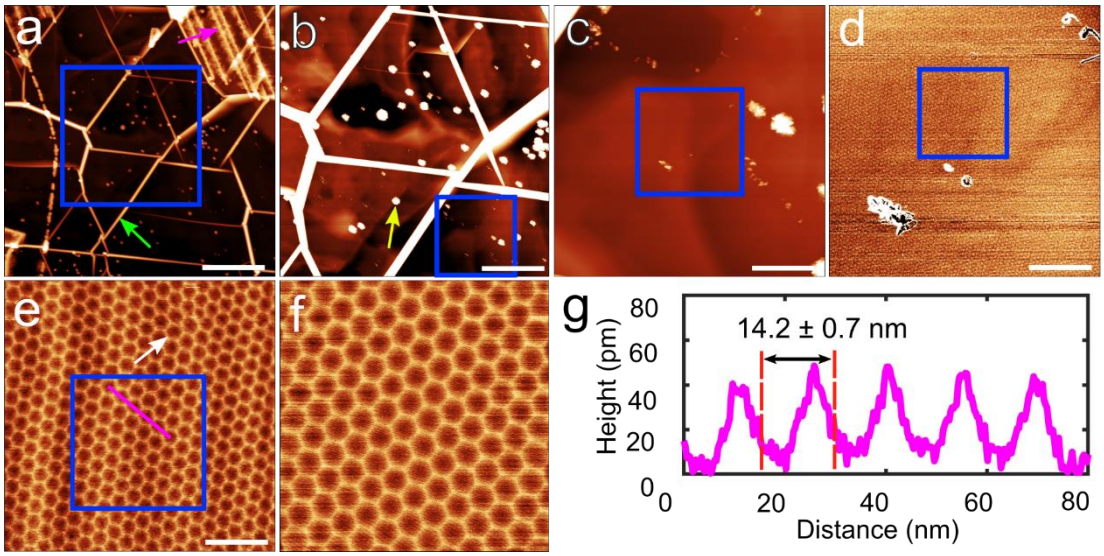

Figure 4.3: AFM images of a flake presenting a 14.2 ± 0.7 nm period Moiré pattern. All images correspond to the topographic channel except d (phase). Blue squares indicate the areas where the next image was taken. White arrow in e points at topological defects Profile in g was taken from the path marked by a magenta line in e. The peak to peak height of the Moiré is ~ 40 pm. Scale bars: (a) 4 µm, (b) 2 µm, (c) 500 nm, (d) 250 nm, (e) 50 nm, (f) 20 nm.

Moiré patterns with different periodicities are typically found on different flakes of the same sample. Even in the same flake different periodicities can be observed, at different areas and change progressively along the surface. Nevertheless, we tend to observe that the largest period found on each sample tends to increase with the growth temperature. Figures 4.4b-f correspond to the largest period Moiré found in samples grown at different temperatures, ranging from 25 ± 2 nm (0.79 ± 0.04 % strain) on samples grown at 1500 ºC up to 75 ± 4 nm (1.46 ± 0.08 % strain) on a sample grown at 1710 ºC. In Fig 4.4a, the 14.2 ± 0.7 nm Moiré shown previously, provides a reference. The area scanned in each image is 250×250 nm^2. All images correspond to the topographic channel except Fig 4.4d which is a phase channel image. In the phase channel the domain walls appear in darker contrast.

The largest Moiré patterns in each sample are usually found in areas close to deposits. Specially those on step edges. The 75 ± 4 nm Moiré was found in an area with these characteristics (Fig 4.4g). The precise location is indicated by the blue box and the Moiré is shown in 1×1 μm^2 (Fig 4.4h) and 500×500 nm^2 (Fig 4.4i) images. The blue line indicates the path of the profile shown in Fig 4.4k. Figure 4.4l shows the location of the flake in the sample with red arrows indicating the next image.

The morphology of the patterns is similar despite the large difference in periodicities. For example, they display domain walls with heights of the same order and topological defects.

These results indicate that the periods of the Moiré patterns and in turn the overall strain of graphene layers grown on hBN can be greatly increased by using a higher growth temperature. As explained in the background, we consider the difference in expansion coefficients between the two crystals as a possible mechanism responsible for the introduction of overall strain in graphene although this matter requires further investigation.

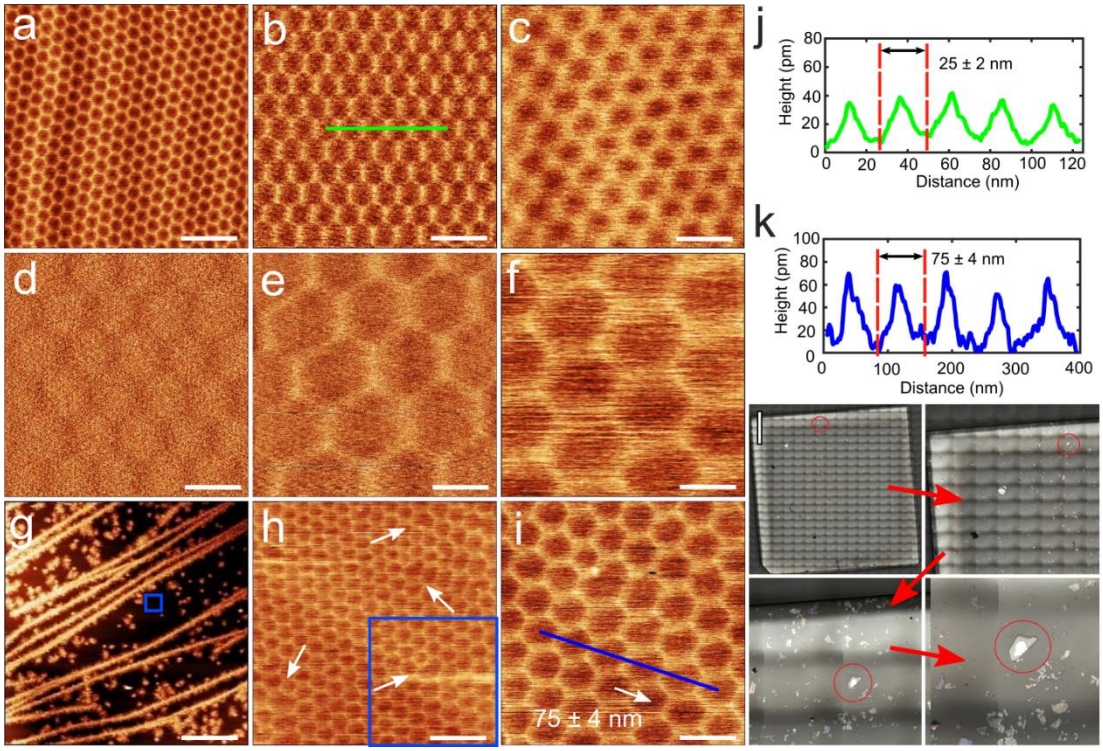

Figure 4.4: AFM images of Moiré patterns with the maximum period found at given temperatures compared with the 14.2 ± 0.7 nm Moiré. a) 14.2 nm Moiré. 0% strain. b) 25 ± 2 nm Moiré. 0.8 ± 0.1% strain. T_{growth}= 1500 ºC. Green line indicates the path of the profile shown in (j). The height of the domain walls is ~35 pm. c) 35 ± 2 nm Moiré. 1.08 ± 0.06 % strain. T_{growth}= 1520 ºC. d) 51 ± 3 nm Moiré. 1.30 ± 0.07 % strain. T_{growth}= 1575 ºC. e) 67 ± 4nm Moiré. 1.42 ± 0.08 % strain. T_{growth}= 1600 ºC. f) 75 ± 4 nm Moiré. 1.46 ± 0.08 % strain. T_{growth}= 1710 ºC. g) Large scan of the flake where the largest period Moiré pattern was found. Amorphous carbon deposits attached to step edges run diagonally across the image. A blue box on one of the terraces indicates the area where the image in (h) was obtained. h) The 75 nm period Moiré pattern extends over a 1 μm^2 area. A few topological defects are indicated by white arrows. i) Higher magnification image extracted from the area in blue box in (h). Blue line indicates the path of the profile shown in (k). The height of the domain walls is ~50 nm. l) Sequence of zoom-in optical microscopy images showing the location of the flake with the 75 nm Moiré. Scale bars: (a-f) 50 nm, (g) 4 µm, (h) 200 nm, (i) 100 nm.

4.2 Lattice-matched graphene

As explained in the introduction, strained graphene has a lattice constant, which is increased from a_G to $a'_G = a_G + \Delta a_G$. This results in a reduction of the mismatch between the lattice constants and an increase in the period of the Moiré pattern. Equation 1.14 shows that in the limit when $a'_G = a_{hBN}$ the Moiré period diverges. In this section we show hBN flakes covered in graphene grown at a substrate temperature of 1675ºC, close to the substrate temperature limit of the MBE system, which exhibit Moiré patterns with periods that effectively diverge. This indicates that the graphene is strained up to a condition where it matches the hBN lattice.

Figure 4.5a shows a large scan of a region on one of the flakes where Moiré patterns with divergent periods were found. Carbon deposits are formed on a series of hBN step edges that run across most of the flake. Their morphology is similar to that of deposits formed on step edges found on other samples. Deposits on defects are also present. The two squares in green and blue respectively indicate the scan areas of Figs 4.5b and c which show the two terraces in more detail. A higher magnification image taken from the rectangular area indicated in green is shown in Fig 4.5d. The Frenkel-Kontorova walls that appear as bright topographic lines form distorted Moiré patterns around the edges of the image. These Moiré patterns are connected with a network of Frenkel-Kontorova walls that run hundreds of nm along one of the specific crystallographic directions with a relative orientation of 120º. The typical separation between walls is 100-200 nm and their widths are highly uniform. Many of these Frenkel-Kontorova walls terminate at specific points instead of connecting to other walls.

Figure 4.5e, extracted from the terrace located in the centre of Fig 4.5c shows another area with the same features but in this case, there is a large region in the centre of the image where the separation between lines is ~500 nm. We argue that these regions between Frenkel-Kontorova walls, where the Moiré pattern effectively diverges, correspond to lattice-matched graphene on hBN. Later in this chapter, AFM lattice resolution images show that the points where the domain walls terminate, correspond to defects in the graphene lattice.

The phase channel image in Fig 4.5f shows Moiré patterns and the Frenkel-Kontorova domain walls in relation with the carbon deposits. The image was obtained from the same area as the topographic image in Fig 4.5c. Figures 4.5g and h were extracted from nearby areas on this flake.

Figure 3.5i shows the same hBN terrace in Fig 4.5c and f approximately two months after the previous images were taken. The terrace in the middle of the image remains intact, but the two neighbouring terraces above and below display cracks (meandering black lines). A series of zoom-in images in Figs 4.5j and k (purple and yellow squares) show the bottom terrace in more detail.

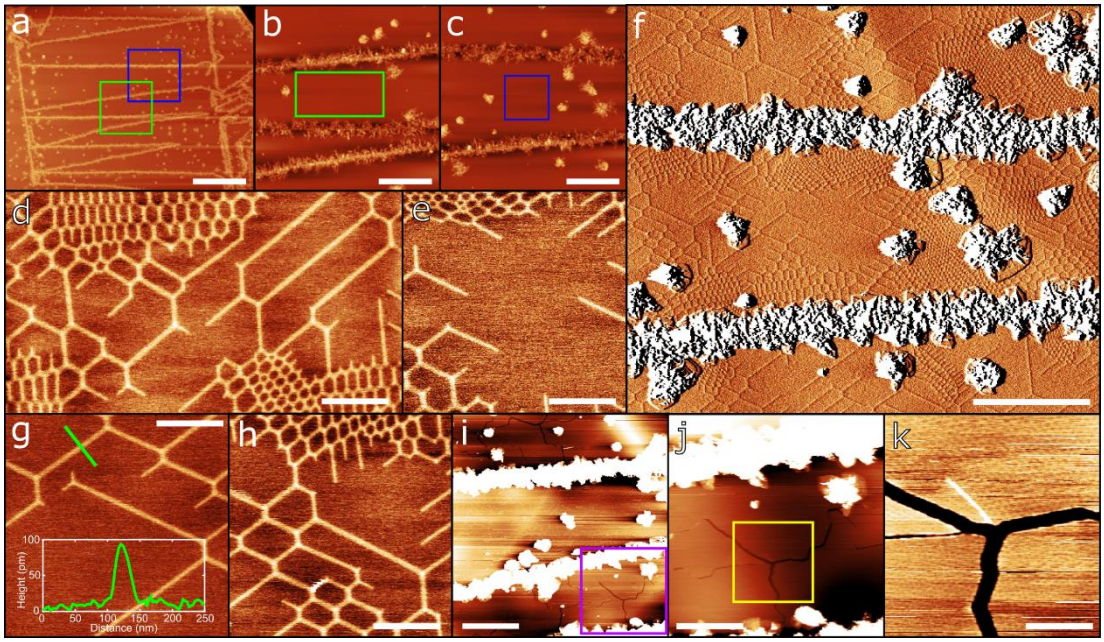

Figure 4.5: AFM images of a hBN flake on a sample grown at 1675 ºC exhibiting Moiré patterns with divergent periods. All images correspond to the topography channel except (f) which is an amplitude channel image. a) Large scan of the flake. A series of step edges with amorphous carbon deposits are distributed along the surface of the flake. Blue and green squares denote respectively the areas where (b) and (c) were taken. b-c) Higher magnification images of these terraces and the areas between them. A few deposits at defects can also be appreciated. The green rectangle in (b) indicates the scan area of (d) and the blue square in (c) indicates the area shown in (e). d) Distorted Moiré patterns lie on the bottom corners and at the top of the image. In the areas unoccupied by these distorted Moiré patterns we can observe bright topographic features i.e. F-K domain walls running along specific crystallographic directions with a relative orientation of ~120º. The widths and heights of these features are highly uniform. Although all the domain walls are connected to each other or to a Moiré pattern, some of them have an end that terminates abruptly. e) Similar features are found in an area on the neighbouring terrace. In this case there is an area of ~ 500×500 nm^2 between walls. f) Amplitude channel image showing the location of features described with relation to the carbon deposits on the step edges. The area approximately matches the area covered by (c). g and h) Similar features found in a nearby terrace. Profile in (g) shows that the height of the wall measured is ~90 pm. i) Image taken approximately 2 months after the previous showing in the centre of the image a terrace with no cracks while the graphene layers in neighbouring terraces above and below are cracked. j and k) Sequence of zoom-in images of one of these cracks. Scale bars: (a) 5 µm, (b and c) 1 µm, (d, e, g and h) 200 nm, (f) 1 µm, (i) 1 µm, (j) 500 nm, (k) 100 nm.

Lattice resolution AFM images, shown in Fig 4.6, were taken from another flake in the same sample grown at 1675 ºC, after various failed attempts on the flake described in Fig 4.5 resulted in cracking and relaxation of graphene layers. Figure 4.6a shows a topographic image in AC mode of the region where these images were obtained. The region is located on a terrace surrounded by amorphous carbon deposits on hBN step edges, similar to the regions shown in Fig 4.5. Figure 3.6b corresponds to the phase channel of the image in Fig 4.6a. Small additional layers emerging from carbon deposits as well as the Frenkel-Kontorova-like domain walls, in darker contrast, can be appreciated. In Fig 4.6c a higher magnification phase channel image allows a clearer view of the domain walls. The blue box indicates where the image in Fig 4.6d was taken.

The bright topographic features i.e. F-K domain walls observed in this flake exhibit the same morphology as those in Fig 4.5. A profile (Fig 4.6f) along the path identified in Fig 4.6d shows an apparent height of 40 ± 4 pm and a FWHM of 21 ± 2 nm as measure in AC mode, while in contact mode the apparent height is ~64 ± 4 pm and the FWHM is 6 ± 0.5 nm. These differences arise from the different scanning modes employed. In the case of AC mode the AFM tracks contours of constant amplitude while in contact mode the contours are of constant cantilever deflection. An image with lattice resolution (Fig 4.6e) of the area highlighted in Fig 4.6d where one of the F-K domain walls terminates shows that the lines are oriented at 30º to the lattice vectors of graphene. These directions are overlaid on Fig 4.6e.

A schematic cross-section of an F-K defect is shown in Fig 4.6h. Here the periodic potential minima on the hBN are represented by the red sinusoid, while the filled black circles correspond to carbon atoms. At the edges of the schematic the carbon atoms sit in their preferred positions above the potential minima arising from the hBN substrate, but at the centre there is an extra row (viewed in cross-section) of carbon atoms. Thus, the lattice constant varies across the graphene and is larger at the centre of the Moiré cell than at the edge. If the assignment to F-K defects is correct we expect that the bright topographic lines can only terminate at the origin of an edge dislocation in the graphene lattice. This is confirmed by a high-resolution AFM image (Fig 4.6g) in which a hexagonal closed path with edges corresponding to 17 lattice constants is overlaid on the image. The start and end points of the circuit, marked by the yellow

and red points on the circuit, do not coincide. The difference between these points corresponds to the Burgers vector for a defect enclosed by the path which has a magnitude equal to one lattice constant and is oriented normal to the bright topographic

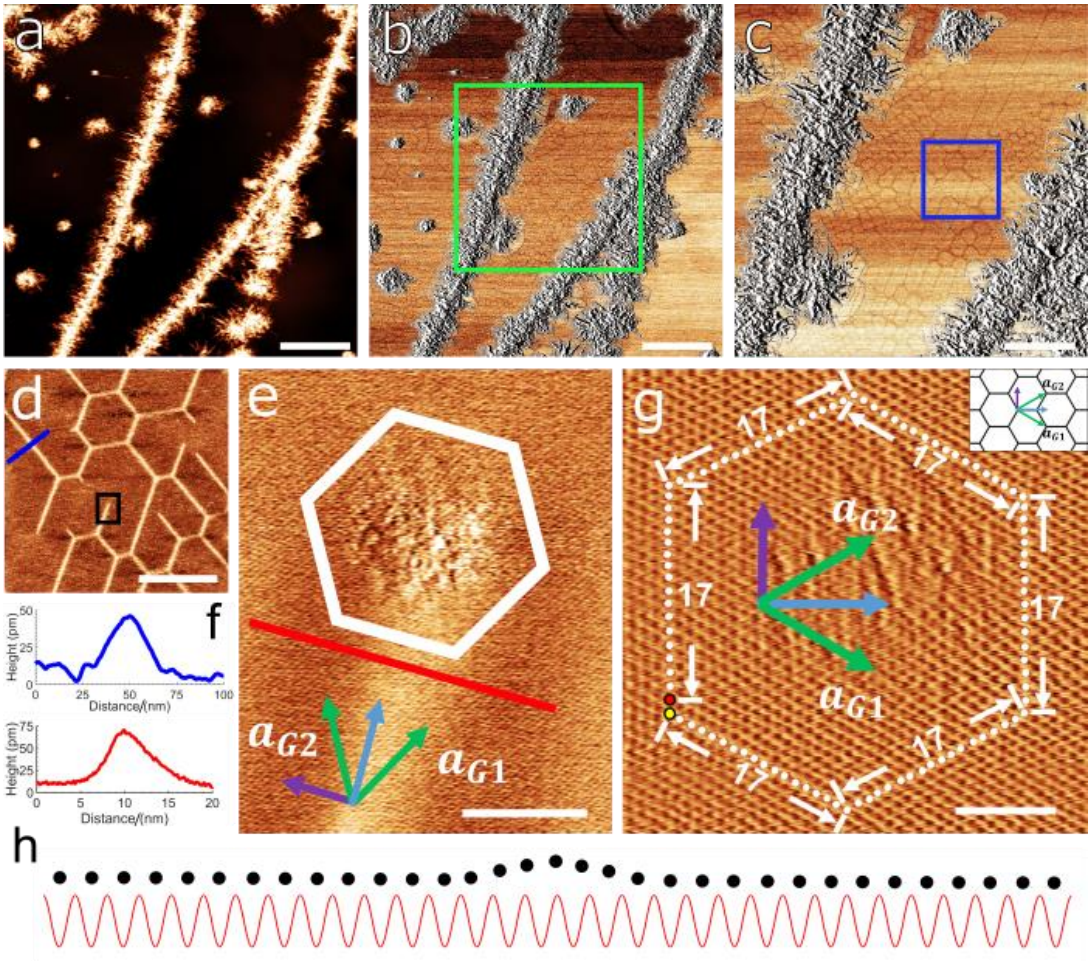

Figure 4.6: AFM images of highly strained graphene and lattice-matched regions. a) Topographic image acquired in AC mode of a terrace containing a highly strained graphene region. b) Phase channel image of the same area shown in (a). c) Phase channel image obtained in AC mode extracted from the area marked with a green square in (b). d) Topographic image acquired in AC mode of a highly strained graphene region, obtained from the area indicated with a blue square in (c). High contrast lines correspond to Frenkel-Kontorova-like domain walls. e) Contact mode topographic image of the area marked with the black rectangle on d showing the end of the defect line. The green, blue and purple arrows indicate respectively, the directions of the unit cell vectors, the defect line and the measured Burgers vector corresponding to an edge dislocation. The white hexagon indicates the path used to obtain the Burgers vector. f) Height profile on path marked by blue line on d and along the path marked in red in (e); g) Lattice resolution image (contact mode, deflection channel) of the end of the defect line. The image is 70° clockwise rotated with respect to (e). The dots with darker contrast are the gaps in the lattice, namely the centres of the graphene hexagons. Those centres coloured in white indicate the Burgers path, which consists of steps over 17 lattice constants along each side of the hexagon, starting at the red dot and finishing at the yellow one. The fact that these two points are not coincident indicates that there is an enclosed dislocation. Inset on top-right shows a schematic of the graphene lattice. Inset on top-right shows a schematic of the graphene lattice with the same orientation. h) Schematic vertical (and perpendicular to the ridge) cut of the graphene lattice (black dots) with the potential generated by the hBN lattice (red line). The graphene is strained and matches the hBN lattice on each side of the dislocation line. Scale bars: (a) 1 µm, (b and c) 500 nm, (d) 200 nm, (e) 5 nm, (g) 2 nm.

lines. This observation provides direct confirmation that a commensurate-incommensurate transition[63] occurs and that the sources of network lines correspond to the introduction of an additional row of carbon atoms. The central regions of graphene in Figs 4.6d are thus lattice-matched to hBN with strain relief in the neighbouring regions provided by point-like defects which act as the source for additional rows of carbon atoms.

The Raman spectra in Fig 4.7 were acquired by Andrew Davies from the University of Nottingham at the locations of the corresponding AFM images with Moiré patterns with periods (Figs 4.7a-d) of λ_S =14.2 ± 0.7nm, 32 ± 2 nm, 50 ± 3 nm and 75 ± 4 nm. These periods correspond respectively to strains of 0 ± 0.1%, 1.01 ± 0.06%, 1.30 ± 0.07% and 1.46 ± 0.08%. Raman spectra from an area with lattice matching material shown in Fig 4.5e, were also acquired. From the background, the strain in this case is given by δ = 0.018. We made sure that the AFM and Raman data corresponded to the same areas by taking nearby carbon deposits as a reference.

As expected,[81,83] the presence of strain leads to pronounced changes in the spectral features. In Figs 4.7a-d there are three peaks in the 2D band of the Raman spectra, two of which (here referred to as 2D† and 2D††) are red-shifted relative to unstrained relaxed graphene. A third peak, $2D_{ag}$ is associated with the presence of turbostratic graphene aggregates which co-exist with monolayer graphene in some regions of the surface. The two red-shifted peaks were previously assigned[64] to strained graphene on hBN, and the spectra in Fig 4.7 show clearly that the trend for increasing red-shift of the 2D† and 2D†† bands with increased Moiré period continues beyond the previously reported[64] limit of λ_S = 30 nm. The Raman spectrum shown in Fig 4.7e is qualitatively different; here we find a highly red-shifted, mono-lorentzian 2D† peak at 2460 cm^{-1}, and both the 2D†† and $2D_{ag}$ bands are absent. In addition, we observe a clear red-shifted G peak, referred to as G†, at 1488 cm^{-1}. Remarkably, the complex splitting and broadening which is present in Figs 4.7a-d evolves into Raman peaks in Fig 4.7e which are much narrower with full-width half maxima (FWHM) of 22 and 13 cm^{-1} ((2D†) and G†, respectively), close to the values observed for high quality exfoliated graphene[81].

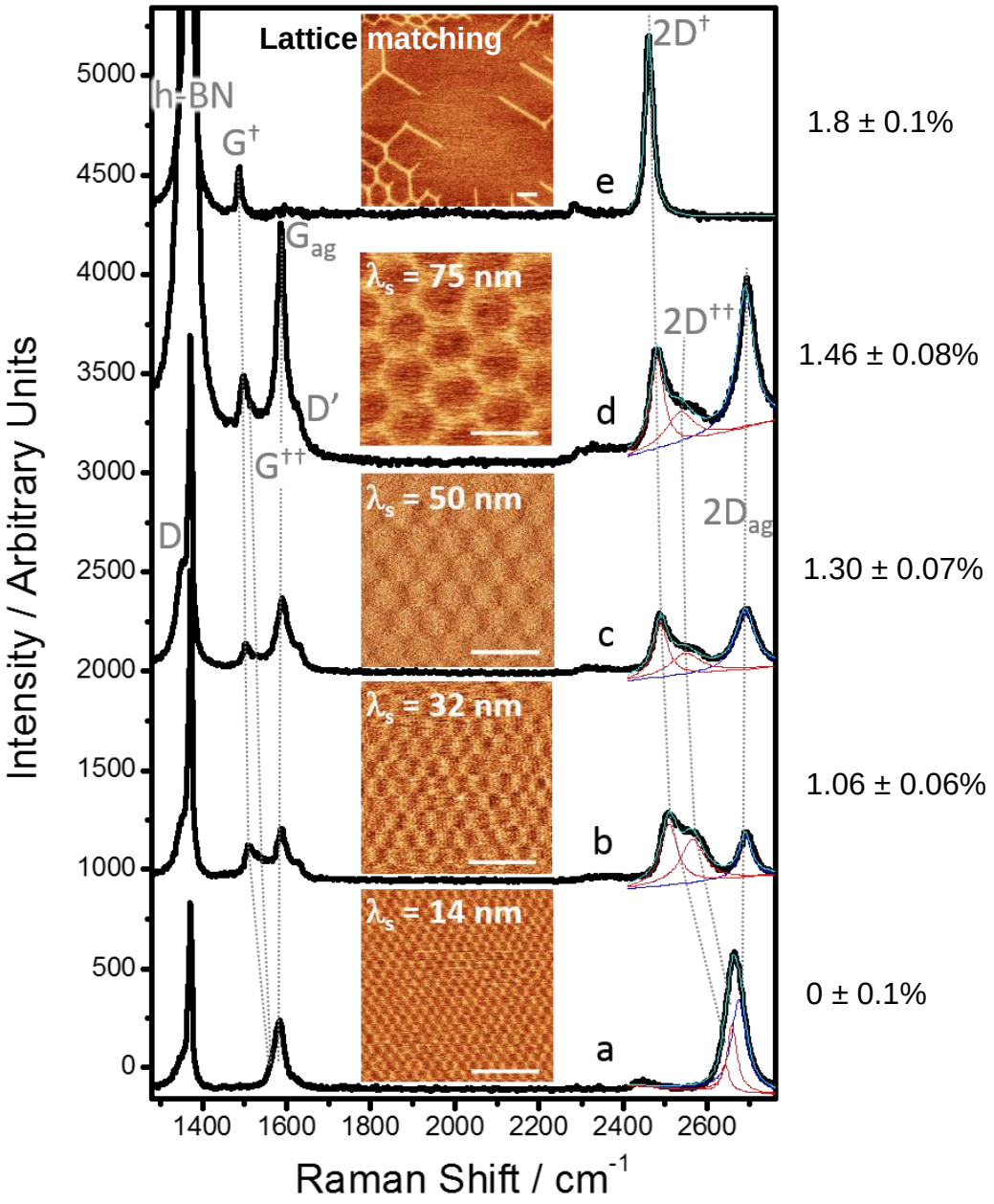

Figure 4.7: Raman spectra showing the evolution of the red-shifting G and 2D bands with increasing Moiré periodicity. The black lines are experimental data and the overlaid light blue line is a multi-Lorentzian fit to the 2D region; (a)-(d) have two red-shifted components (the red curves) and a third unshifted band (dark blue) arising from carbon aggregates whilst (e) has a single red-shifted band; In the G region there are two red-shifted peaks (one in (e)) together with the unshifted G and D' peaks from the carbon aggregates ((b)-(e) only). Inset Figures show the AFM image recorded in AC mode in the vicinity of the location where the Raman spectrum was obtained. The Moiré period λ_S ranges from 14.2 ± 0.7 nm for unstrained graphene on hBN (a) up to 75 ± 4 nm in (d) and effectively diverges in (e) where the defect lines are topologically modified. The percentage of overall strain is indicated next to each spectrum. Scale bars are 100 nm.

These observations provide direct evidence that the local environment of carbon atoms is much more uniform in regions such as in Fig 4.7e. Note that a graphene sheet subjected to isotropic strain would be expected to exhibit Raman peaks which, although shifted in energy, would not undergo splitting due to the absence of symmetry breaking. Such spectra have been reported for a graphene membrane under hydrostatic pressure[84] and, for a quoted strain of 1.8%, are very similar to those observed in Fig 4.7e although our measured values of FWHM are significantly narrower. We also note that the relative intensity I(2D††)/I(G††) ≈ 3.8, close to the value observed for exfoliated monolayer graphene[81]. Several other peaks are present, like the hBN E_{2g} phonon mode, at 1366 cm^{-1}. The spectra in Fig 4.7a-d show a G†† peak associated with strained graphene (present as a shoulder on the G† peak), and other peaks associated with the presence of turbostratic graphene - an unshifted G_{ag} peak (at ~1585 cm^{-1}), a D shoulder on the hBN peak (at ~1350 cm^{-1}), and a D' shoulder on the unshifted G peak (at ~1625 cm^{-1}).

At low red-shift the 2D†† peak has a higher intensity than the 2D† peak (Fig 4.7), but is weaker for higher red-shift. Summerfield et al. suggested[64] that the 2D† and 2D†† bands could arise from, respectively, the centre of the Moiré cell where the strain is isotropic[69] and the edges where it is uniaxial.

In Fig 4.8a we compare the measured dependence on strain of the intensity ratio, I(2D†)/I((2D††) with a simple model which assumes that the edge region has a fixed width, d, independent of the strain and that the ratio of the intensities of the 2D†† and 2D† peaks is equal to the ratio of the boundary and central regions of the Moiré unit cell. For a Moiré pattern with period λ_S the intensity ratio is given by:

$$\frac{I(2D\ \dagger)}{I(2D\ \dagger\dagger)} = \frac{(\lambda_S - d)^2}{{\lambda_S}^2 - (\lambda_S - d)^2} = \frac{(\lambda_S - d)^2}{d(2\lambda_S - d)^2}$$

Noting that $\lambda_S = \frac{a_G^2}{\delta a_G - \Delta a_G}$ with $\delta a_G = (a_{hBN} - a_G)$ and $\Delta a_G = (a_{Gstr} - a_{G\ unstr})$:

$$\frac{I(2D\ \dagger)}{I(2D\ \dagger\dagger)} = \frac{a_G^2(1 - d(\delta a_G - \Delta a_G)^2/a_G^2}{d(2(\delta a_G - \Delta a_G) - d(\delta a_G - \Delta a_G)^2/a_G^2)}$$

In the limit where $\delta a_G \rightarrow \Delta a_G$ and assuming that λ_S >> d, the expression reduces to:

$$\frac{I(2D\,\dagger)}{I(2D\,\dagger\dagger)} = \frac{a_G^2}{2(\delta a_G - \Delta a_G)}$$

The intensity ratio is expected to diverge as the strain approaches the lattice-matching condition. This is consistent with our observations and a fit to the data in Fig 4.8 gives a value of 1.9 ± 0.1% for $\delta a_G/a_G$, close to the expected value, 1.8%. Note that for lattice-matching the fraction of material at the edge regions is negligibly small and the associated 2D†† peak is no longer present, as observed in Fig 4.7e. We also assign the G† and G†† features to the two different graphene environments (centre and edge of the Moiré cell respectively).

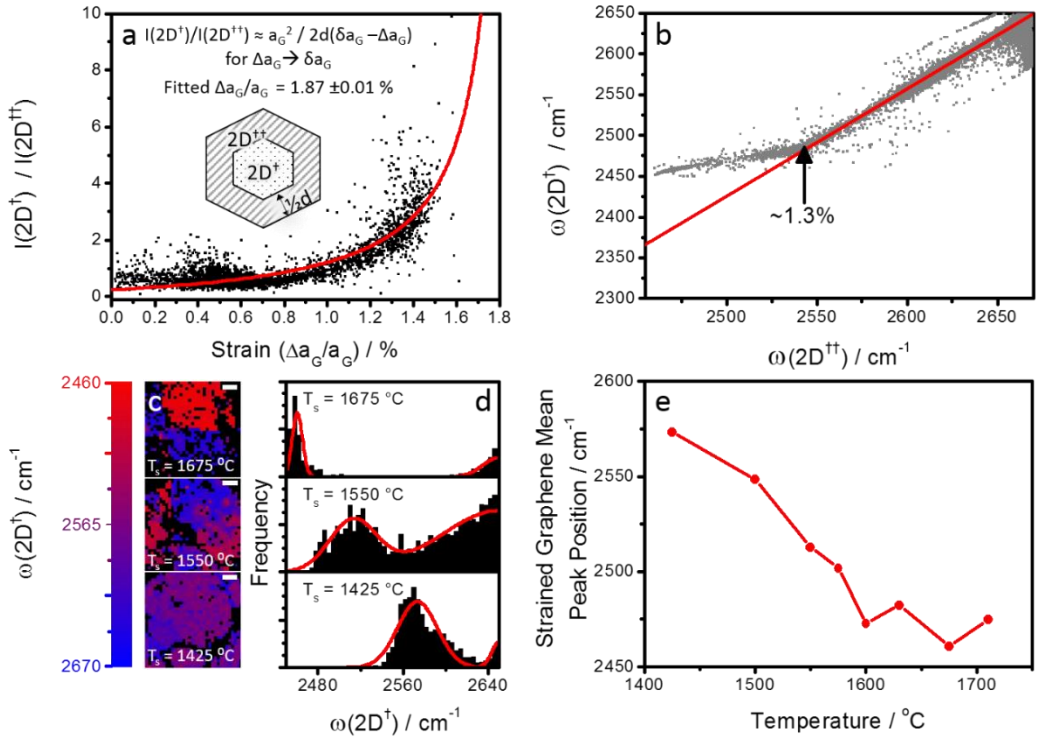

Figure 4.8: Raman analysis of the transition to lattice-matching. a) Ratio of the Intensities of the two 2D Raman bands as a function of strain (estimated from the Raman peak position). The red line shows a fit of the data to a model based on our assignment of the two bands to the centre (2D†) and edge regions (2D††) of the Moiré pattern (inset and SI). b) Position of the two 2D bands plotted against each other from samples grown at temperatures ranging from 1425 °C to 1710 °C. The red line shows the trend for strains up to 1.3%. c and d) Statistical analysis of peak fitted Raman spectral maps for the 2D† band. c) False colour maps of ω (2D†), Scale bars: 5 µm, whilst (d) shows frequency distribution histograms of the same data. The red line shows a bi-Gaussian fit. The effect of temperature on the position of the most red-shifted Gaussian domain (indicative of strained graphene), is shown in (e).

An interesting critical behaviour is revealed in Fig 4.8b, which shows a scatter plot of the Raman 2D peak position shifts, ω(2D†) and ω(2D††). For strains up to ~1.3%, which corresponds to λ_S ~ 50 nm, we observe a linear dependence (red line), followed

by an abrupt change in gradient for higher strains. We suggest this change occurs when the average strain is sufficiently high for the graphene at the centre of the Moiré cell to be lattice-matched with the hBN substrate. This change in gradient would imply that the strain at the centre of the Moiré cell is close to 1.8% when the average strain is 1.3%, while the strain at the edges will be < 1.3%. Further increases of the average strain beyond this value results in an increase of the fraction of the Moiré cell area which is lattice-matched, but the maximum strain, and therefore the 2D† Raman shift will remain approximately constant. In contrast, the strain at the edges, and the red-shift of the 2D†† Raman peak, will continue to increase until the average strain is ~1.8% at which point the Moiré period diverges, the edge regions effectively disappear and the 2D†† peak loses intensity and merges with the 2D† peak.

Nevertheless, since the contribution of the D'+D peak to the Raman spectra is not considered and the $2D_{ag}$ peak is not fully measured due to the range of the Raman spectra taken (Fig 4.7), the deviation of this trend at 1.3% could be due to issues around fitting the three peaks. Besides, for strains ~1% or lower, the 2D†, 2D†† and $2D_{ag}$ peaks are clustered together in a single peak (Figs 4.7a and b) which may affect to the reliability of the data for strains below 1% in Figs 4.8a and b.

The dependence of the strain on the growth temperature was extracted from Raman maps of the sample as shown in Fig 4.8c. Raman spectra were acquired at each point (in a square map of dimensions 32 x 32 μm^2) and the band position, ω (2D†), was extracted using a fitting procedure for samples grown at temperatures between 1425 and 1710 °C. For selected growth temperatures in Fig 4.8, spatial maps of ω(2D†) show regions of highly strained material (red) co-existing with regions (blue) where the strain is much lower. From our AFM scans we believe that the bluer regions correspond to areas of graphene which were initially strained but relaxed post-growth through the propagation of cracks. For each temperature we also show a histogram of the number of pixels with a given value of ω(2D†) revealing a bi-Gaussian distribution corresponding to strained and relaxed graphene. In Fig 4.8e the extracted mean peak position of the strained material confirms a systematic increase in the Raman shift (and strain) with growth temperature up to ~1600 °C. Above this temperature ω(2D†) is approximately constant (ca. 2460-2480 cm^{-1}) indicative of lattice-matched graphene at the centre of the Moiré cell.

4.3 Cracked layers, additional layers and other features

Figure 4.9 shows images of a flake where a 14.1 ± 0.7 nm and a 25 ± 2 nm period Moiré were found. The graphene was grown at a 1520 °C sample temperature. In Fig 4.9a a 10×10 μm^2 image of the flake surface shows a series of carbon deposits. The approximate widths and heights of these deposits are respectively ~500 nm and ~150 nm. The green square in Fig 4.9a marks the area between deposits where the image in Fig 4.9b was taken.

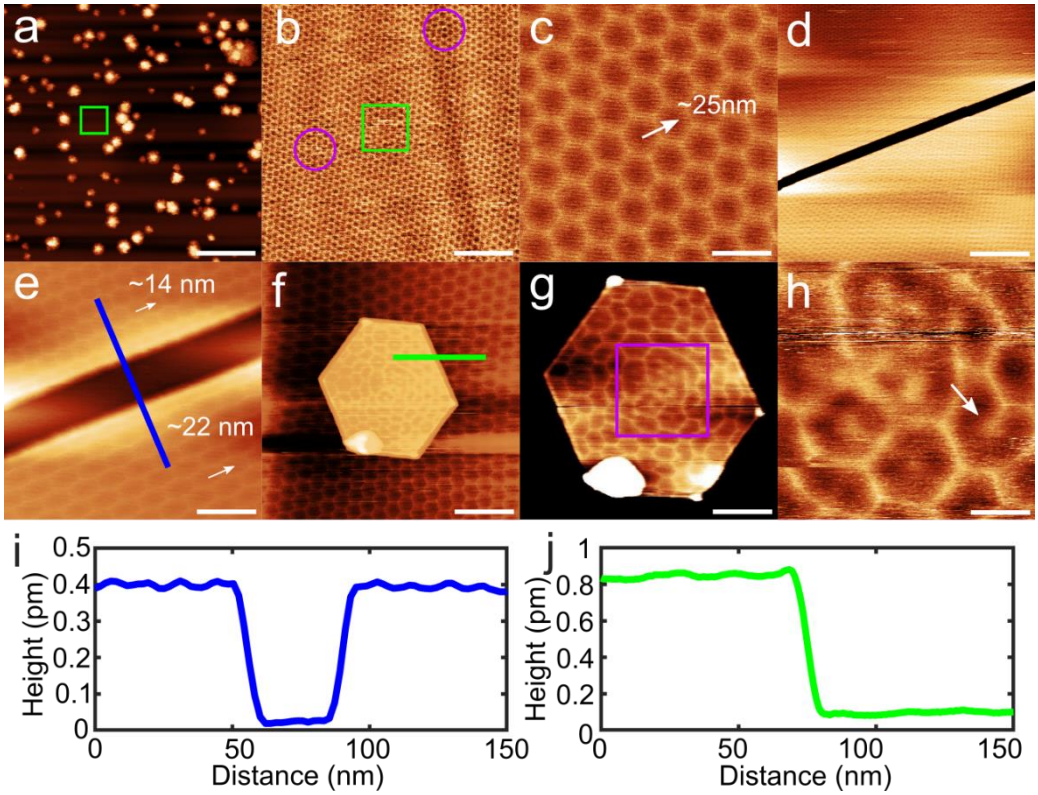

Figure 4.9: AFM topographic images of a various features on a hBN flake in a sample grown at 1520 °C. Images a to c are a series of zooms-in in the regions indicated by green squares. a) 10×10 μm^2 image of the flake shows large carbon deposits. In this case there are no hBN thermal cycling wrinkles. b) A 1×1 μm^2 where the surface rugosity has been subtracted shows the Moiré pattern along the area. Purple circles indicate topological defects. c) Moiré pattern in detail with the periods of the Moiré pattern in each direction indicated. d) A crack in a nearby area. The Moiré pattern in the domain above the crack remains quite regular while in the region below the Moiré is distorted shifting orientation as we move from left to right. e) A closer look in the area shows that the domain below the crack preserves an overall strain (~0.7%) in the direction parallel to the crack with a 22 ± 2 nm Moiré in this direction. The domain above the crack presents a regular 14.1 ± 0.7 nm Moiré. Profile with path indicated by a blue line shown in (i) indicates that the crack has a depth corresponding to a graphene monolayer. f) An island with hexagonal edges on the same flake. The profile in (j) indicates that the island is formed by a second and a third layer. The Moiré pattern in the island, is roughly aligned and has a similar periodicity to the 25 ± 2 nm Moiré of the first layer below. The contrast has been adjusted in order to observe both the first layer and the island Moiré patterns. g) Higher magnification of the island shows the pattern on the whole surface of the island. h) Zoom-in image in the area indicated by purple square in g. White arrow points at a defect. Scale bars: (a) 2 μm, (b) 200 nm, (c) 40 nm, (d) 200 nm, (e) 40 nm, (f) 100 nm, (g) 60 nm, (h) 20 nm.

The 25 ± 2 nm Moiré pattern extends over the whole 1×1μm^{2}scan area in Fig 4.9b. Purple circles highlight two topological defects. A higher magnification image in Fig 4.9c shows the Moiré pattern in more detail. The periods of this Moiré in each direction are very close which indicates that the overall strain is approximately isotropic. Figure 4.9d shows two graphene domains separated by a gap on an area ~15 μm above the area where image c was taken. This gap is most probably a crack formed after growth. The Moiré pattern in the area above the gap is 14.1 ± 0.7 nm parallel to the crack. Below the gap the Moiré pattern in the direction parallel to it is 22 ± 2 nm and in the other two direction is 15.1 ± 0.8 nm and 16.4 ± 0.8 nm. This gap is the upper limit of the strained domain shown in Figs 4.9b-c. The depth, measured with a profile taken along the path in blue and shown in Fig 4.9i is ~0.35 nm, corresponding to a graphene monolayer while the width is ~40 nm.

Small (~200 nm) multi-layered graphene islands have been observed. Figures 4.5f-h show an island found in the strained domain, below the crack previously described. The edges of this island form a hexagon and seem to run in parallel to the walls of the Moiré pattern corresponding to the armchair direction. Small ~0.5 nm high carbon deposits lie on four of the six corners of the hexagon. A larger carbon deposit (~ 4 nm high) lies on the bottom left corner. The period and the orientation of the Moiré pattern on the island roughly match the period and orientation in the first layer, although the Moiré observed on the top of the island is very distorted. The height of the island ~0.7 nm was measured with a profile, shown in Fig 4.9j and corresponds to two additional graphene layers. The top layer of the island is therefore a third layer. The step is very sharp and no surface of the second layer is exposed.

We believe that the additional layers in this island are strained in a similar manner as the first layer, since if they were relaxed, conforming to the relief of the Moiré pattern of the first layer, we would see an additional Moiré pattern. Interestingly, from the size and shape of the pattern, which can be observed in detail over the whole island in Fig 4.9g, it seems like the strain close to the right and left sides of the island, in the vertical direction is larger than in the horizontal direction while close to the up and bottom sides of the island the horizontal strain seems larger than the vertical direction. Figure 4.9h shows the Moiré pattern in the centre of the island in more detail. A defect where a domain wall ends up abruptly is indicated by a white arrow. The mechanism by

which the island was formed may involve a larger growth rate of the top layer (third layer) compared to the second layer. Otherwise, the surface of the second layer would be partially exposed.

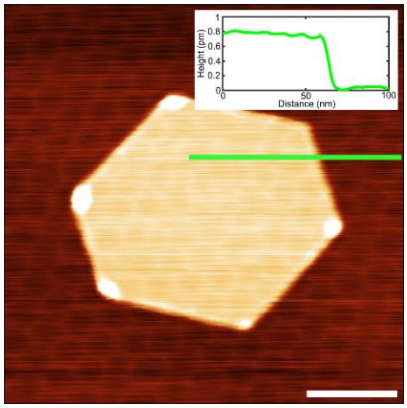

Figure 4.10: A hexagonal island with a third layer on top similar to the one described in the previous Figure found in another sample also grown at 1520 ºC. Moiré pattern on top ~19 nm. Scale bar: 40 nm.

An island formed also by two additional layers with hexagonal edges was found in another sample grown at 1520 ºC (Fig 4.10). The height was also measured by a profile shown in the inset. The path is indicated in green. The Moiré pattern in the top layer, which is also a third layer has the same periodicity as the Moiré in the surroundings with ~15 nm period in two of the directions and ~19 nm in the third direction and is aligned with it. The edges of the island run also approximately parallel to the walls of the Moiré pattern and carbon deposits, in this case ~2 nm in height lie as well on most of the corners of the island.

Cracked layers are often found in flakes with a low density of carbon deposits on samples where graphene was grown at high temperatures. This supports the hypothesis of carbon deposits playing a role in the preservation of strain. Figure 4.11 shows images of flakes with cracked layers on a sample grown at 1630 ºC. Figure 4.11a corresponds to a 10×10 μm^2 phase channel image where a few deposits are mostly located in the lower left quarter. Squares coloured in yellow blue and green indicate respectively the areas where Figures 4.11b-d were taken. Images on Figs 4.11e-f were taken from cracks in another flake of the same sample with cracked layers.

Contrary to the case of the crack in Fig 4.9d-e, the widths of the gaps between layers shown in Fig 4.11 are not constant (green and blue arrows in 4.11b) and in some cases the Moiré varies orientation leading to areas with a larger Moiré and strain (white arrows in Fig 4.11b and g). We can infer that the right-hand side of layer, past the narrow neck, is pushed downwards or rotated clockwise with respect to the left-hand side.

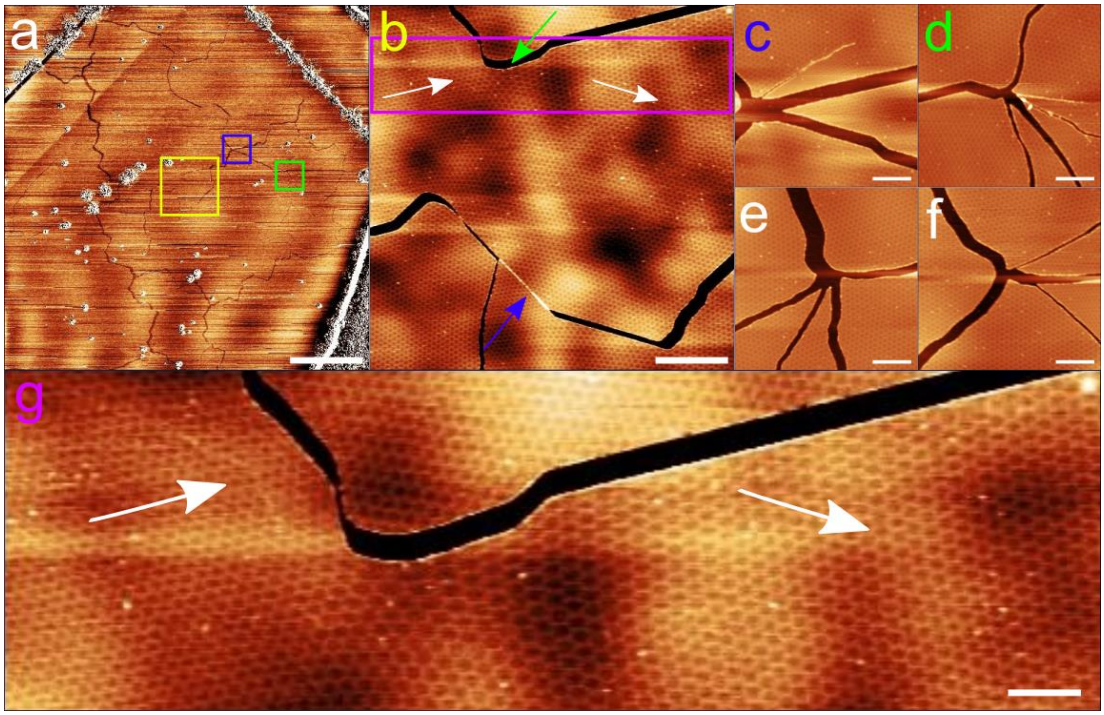

Figure 4.11: Images of cracked graphene layers on a sample grown at a high temperature 1630ºC with an insufficient amount of carbon deposits to hold the strain. Image (a) corresponds to the phase channel while the rest of the images correspond to topographic. In (a), yellow, blue and green squares indicate the areas where (b), (c) and (d) were respectively taken. In this flake, some Moiré patterns appear rotated with respect to each other at opposite sides of the cracks or even shift orientation along the layer, as indicated with white arrows show in (b) and in the higher magnification image in (g) extracted from the area indicated by the rectangle in magenta. Green and blue arrows in (b) point respectively at a region with horizontally strained graphene and an edge where the layers connect. Scale bars: (a) 1 µm, (b) 200 nm, (c-f) 100 nm, (g) 70 nm.

Figure 4.12 shows images of another flake in the same sample where a crack close to carbon deposits generates other areas of anisotropically strained graphene. A V shaped line of deposits (Fig 4.12a) was formed on a hBN step edge. There are also a few carbon deposits formed on hBN defects in the centre of the image. Figure 4.12b, corresponding to the phase channel of the same image, reveals the graphene cracks formed post-growth. In Figure 4.12c (from purple square in Fig 4.12b), we can examine the area between deposits in more detail. Additional graphene layers emerge from the step edge and from the carbon deposits next to it. The numbered arrows on the image indicate the location where the images in the next rows in the same figure where taken. The path of the crack in has been highlighted with a black curve in the up-right quadrant of Fig 4.12c.

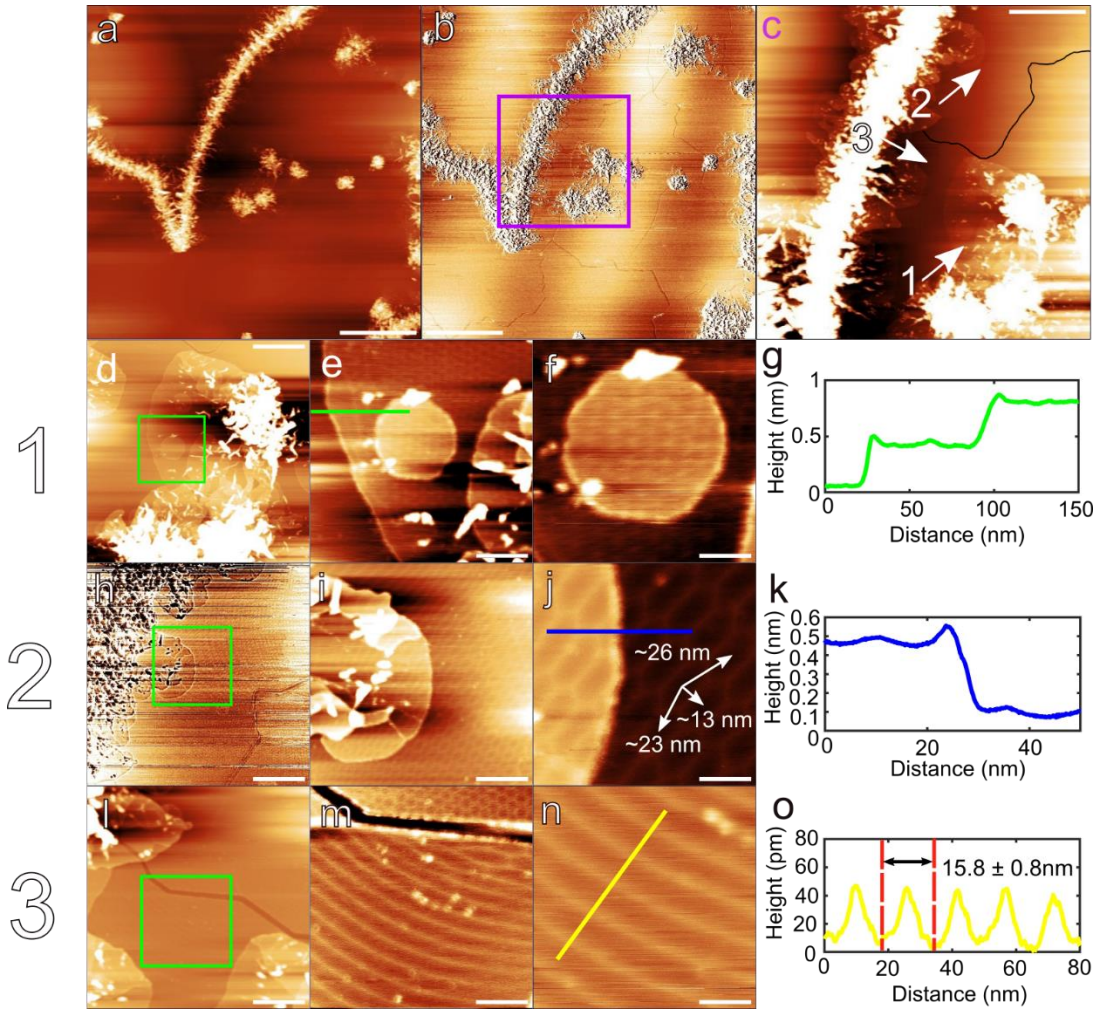

Figure 4.12: Images of a flake with a series of interesting features. The sample was grown at 1630ºC a) Large scan topographic image of an area with a V-shaped carbon deposit on step edge and a few other deposits. b) Phase channel image corresponding to a, allows to observe graphene cracks in the surface. c) Higher magnification image obtained from the area indicated in (b). Additional graphene layers emerging from the deposits on step edge and hBN defects. Numbers indicate the areas where the images in the next rows where taken. Black meandering line highlights the path of the crack. d) Phase channel image of carbon deposits from which additional graphene layers emerge. e) Image taken from area marked with a green square in (d). A third graphene layer with circular edges lies on the surface of a second layer with a larger surface. Line indicates path of profile shown in (g). f) Higher magnification image of the island. The Moiré patter is aligned with the pattern of the layers below and has the same periodicity. Small ~4 nm carbon deposits are found on the edges. g) Profile showing the ~0.35 nm height of the second and third layers. h) Phase channel image. Additional layer emerging from the step edge carbon deposit. The distorted Moiré pattern and a nearby graphene crack are also present. j) Zoom-in image extracted from the centre of (i). The distorted Moiré pattern has the same shape in both first and second layers. Arrows indicate periods in each direction. Blue line denotes the path of the profile in (k). k) Profile indicates height of a graphene monolayer. l) Area between carbon deposits with a semi-horizontal crack running through the middle of the image. The crack also runs below a second graphene layer in the up-left corner. m) Graphene layer anisotropically strained displays a wave-like Moiré pattern. Above the crack, lies a ~14 nm Moiré graphene layer. n) Higher magnification scan shows the Moiré pattern in more detail. The profile extracted from the area is shown in (o). o) Profile indicates that the relief and the periodicity of the Moiré are respectively 40 pm and 15.8 nm. Scale bars: (a-b) 1µm, (c) 400 nm, (d) 200 nm, (e) 60 nm, (f) 30 nm, (h) 200 nm, (i) 70 nm, (j) 20 nm, (l) 100 nm, (m) 40 nm, (n) 20 nm.

Row 1 displays images of two carbon deposits (at right-up corner and at bottom in Fig 4.12d) and the additional layers emerging from them. Figure 4.12e, taken from the area marked by a green square in Fig 4.12d, shows a third layer island on top of the second layer. Green line indicates the path of the profile in Fig 4.12g, which denotes a ~0.4 nm height on each step. Although distorted, the Moiré pattern can be distinguished on this third layer (Fig 4.8f). It has the same ~14 nm period as the pattern in the second layer and it is aligned with it. The magnitude of the Moiré period in this area indicates that the graphene is approximately overall relaxed.

Row 2 shows images of a secondary layer that has emerged from the V-shaped line of carbon deposits. Figure 4.12h corresponds to a phase channel image showing the location of the additional layer next to the line of carbon deposits. The crack close to the bottom-right corner and a distorted Moiré pattern can be appreciated. The green square indicates where Fig 4.12i was taken. The second layer has a round edge with no appreciable deposits. Small additional layers decorated with ~4 nm high carbon deposits are distributed along the edges in a C shape. The Moiré pattern is highly anisotropic in both the first and secondary layers. Figure 4.12j shows in more detail the edge of the island. The image was taken from the central area of Fig 4.12i. The Moiré on the island, with a brighter contrast in the left side of the image, not only has the same periodicity along the different directions but is in phase with the Moiré of the first layer on the right hand side of the image, i.e. the first layer. A profile shown in Fig 4.12k (path indicated in blue in Fig 4.12j) confirms the ~0.35 nm height of a single graphene layer. The arrows indicate the Moiré period in each direction. The shorter 14 nm Moiré direction (white arrow) runs approximately parallel to the direction of the closest trajectory from the carbon deposit the crack. Moreover, this shorter period runs roughly perpendicularly to the step edge covered in carbon deposits. Therefore, we can infer that the strain has been preserved by the carbon deposits located in parallel to the direction of the step edge.

Row 3 shows an area around the crack show in Fig 4.12c, close to carbon deposits on a step edge. Fig 4.12l shows the crack in the centre with additional layers that emerge from nearby carbon deposits at some corners of the image. A higher magnification image in Figure 4.12m reveals a wave-like slightly curved Moiré pattern on the area below the crack and between deposits. On the up-right corner of the domain, next to

the crack, the Moiré recovers a recognizable shape. In the region above the crack the graphene shows a 14 nm Moiré pattern. Figure 4.12n shows the Moiré pattern in higher magnification. A profile taken along the direction approximately perpendicular to the crack, marked with a yellow line, indicates a 15.8 ± 0.8 nm period. From the shape and orientation of the pattern, we can infer that the carbon deposits, located both on the step edge line and on the hBN defect are maintaining the strain of the graphene layer parallel to this direction, while in the perpendicular direction the layer is almost overall relaxed.

Carbon deposits can give rise to other interesting features. A sample grown at ~1700ºC presents narrow carbon deposits that originate from larger deposits on defects and step edges and form meandering lines. Figure 4.13a shows a 10×10 μm^2 area covered in these elongated deposits that, in some cases run along distances up to ~4 μm. White arrows in Figs 4.13a indicate a few of them. If we follow their path we can see them split into two, end up adsorbed by larger carbon deposits or reduce progressively their width until they vanish (with a shape similar to a spike). In Fig 4.13b we can observe two of them, marked with white arrows emerging from a step edge deposit marked with a green arrow. A profile taken from Fig 4.13b crossing both a step edge and a narrow deposit is shown in Fig 4.13g for comparison of their dimensions. Figure 4.13c shows an area where one of these narrower deposits emerges from a carbon deposits on a defect. The contrast has been adjusted so the narrow deposit is visible. The pink square indicates the area around the end of the narrow deposit where Fig 4.13d was taken. This image corresponds to the phase channel. The narrow deposits seem to be in contact with another deposit but does not merge with it. Instead, it advances ~500 nm further up where it forms the spike.

Figure 4.13e, taken from the area indicated by the green square in the previous image allows the resolution of the spike and the underlying Moiré pattern. In most cases, the patterns bend towards the spike and remain misoriented at opposite sides of the deposit (white arrows). The misalignment between the Moiré patterns at opposite sides of the narrow deposits remains several micrometres away from the spike. A further magnification scan shown in Fig 4.13f, reveals a topological defect located precisely

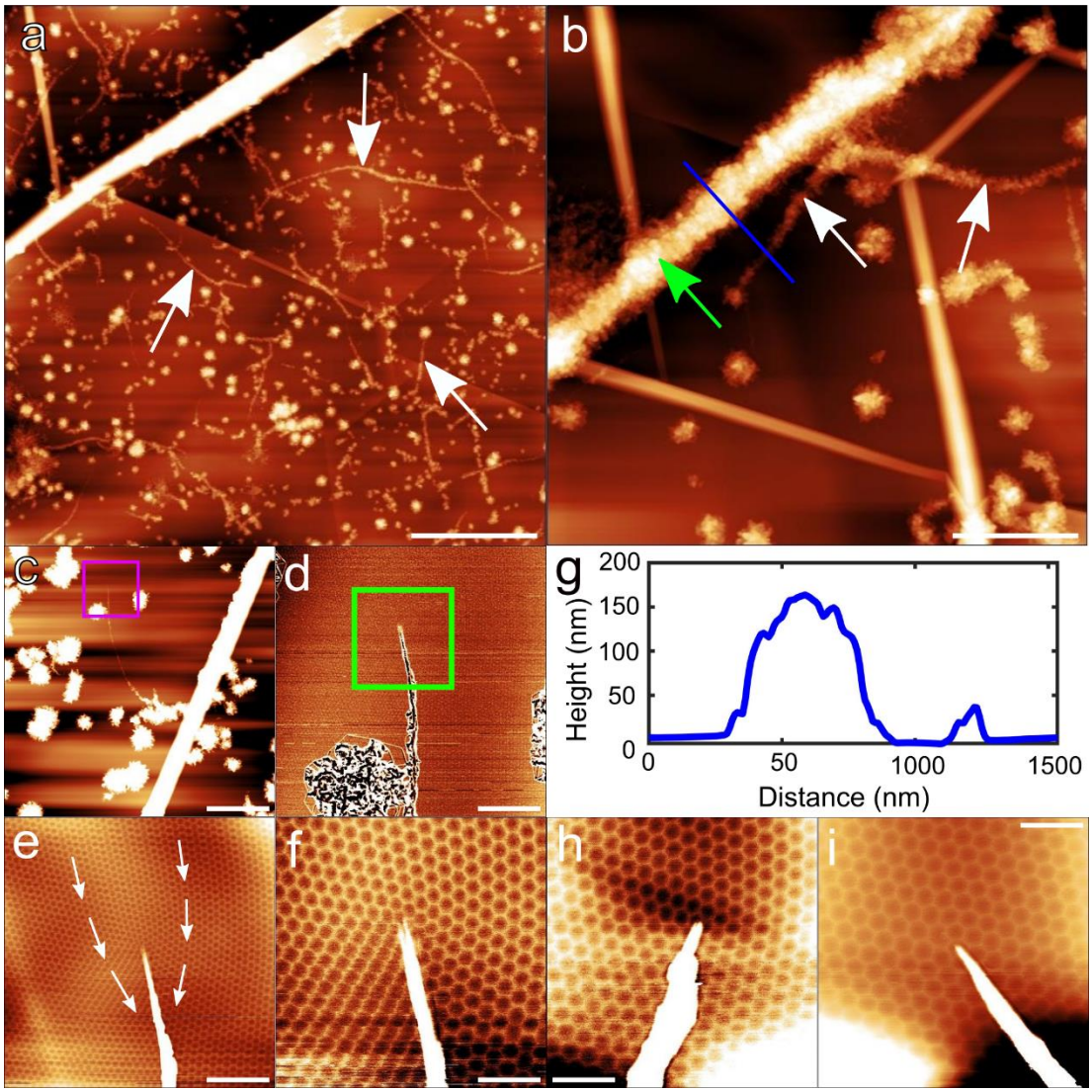

Figure 4.13: a) Large scan showing the surface of a flake covered in narrow carbon deposits that emerge from the usual larger deposits on defects. These deposits can connect larger ones or end up abruptly forming a spike, micrometres away from where they emerged. b) Two narrow deposits (white arrows) emerging from a step edge deposit (Green arrow). Blue line indicates path of the profile in (g). c) Narrow deposit emerging from a deposit on a defect. The large diagonal line corresponds to a hBN thermal cycling wrinkle. The contrast has been adjusted in order to see the narrow deposit crossing the centre of the image. Pink square marks area where the image in (d) was taken. d) Phase channel image of the end of a narrow deposit forming a spike. e) Moiré pattern around a spike. The orientation shifts towards the spike as we approach to it leaving the pattern misoriented at opposite sides of the deposit. f) Higher resolution image taken from the centre of (e) showing a topological defect right at the tip. g) Profile extracted from (b) allows a comparison of the dimensions of a step edge deposit, ~160 nm in height and ~500 nm in width, with a narrow deposit ~40 nm in height and ~150 nm in width. h) Another example of these spikes in a different flake, also displays a shift in the orientation of the Moiré and a topological defect. i) A less likely case where the Moiré is not misoriented. Nevertheless, the defect is also present. Scale bars: (a) 2 µm, (b) 1µm, (c) 1 µm, (d) 200 nm, (e) 100 nm, (f-i) 50 nm.

on the tip of the spike. Figure 4.13h illustrates another spike feature with two rotated Moiré patterns around it. An exception of this feature is show in Fig 4.13i where a defect adsorbs a Moiré row but there is no significant rotation of the pattern.

Additional graphene layers are also found emerging from these deposits. In Fig 4.14a a narrow deposit runs diagonally across the image. The morphology of the deposit can be appreciated in a higher magnification topographic image in Fig 4.14b, taken from the area indicated with a blue square. Figure 4.14c shows the same area in the phase channel. The additional graphene layers lie at both sides of the narrow deposit. The green, turquoise and yellow squares denote the scan areas of Figs 4.14.d, e and f. The edge of an additional layer, in the top-right area of Fig 4.14d exhibits a Moiré pattern aligned, with the same ~14 nm periodicity and in phase with the Moiré pattern of the first layer, as we usually find in additional layers emerging from conventional carbon deposits. Interestingly, the height of this additional layer and of the other layers emerging from the narrow deposit in the area covered by the image in Fig 4.14b are ~0.7 nm, corresponding to two layer graphene. Figures 4.10e and f show the slight rotation of the ~14 nm Moiré pattern at opposite sides of the narrow deposit.

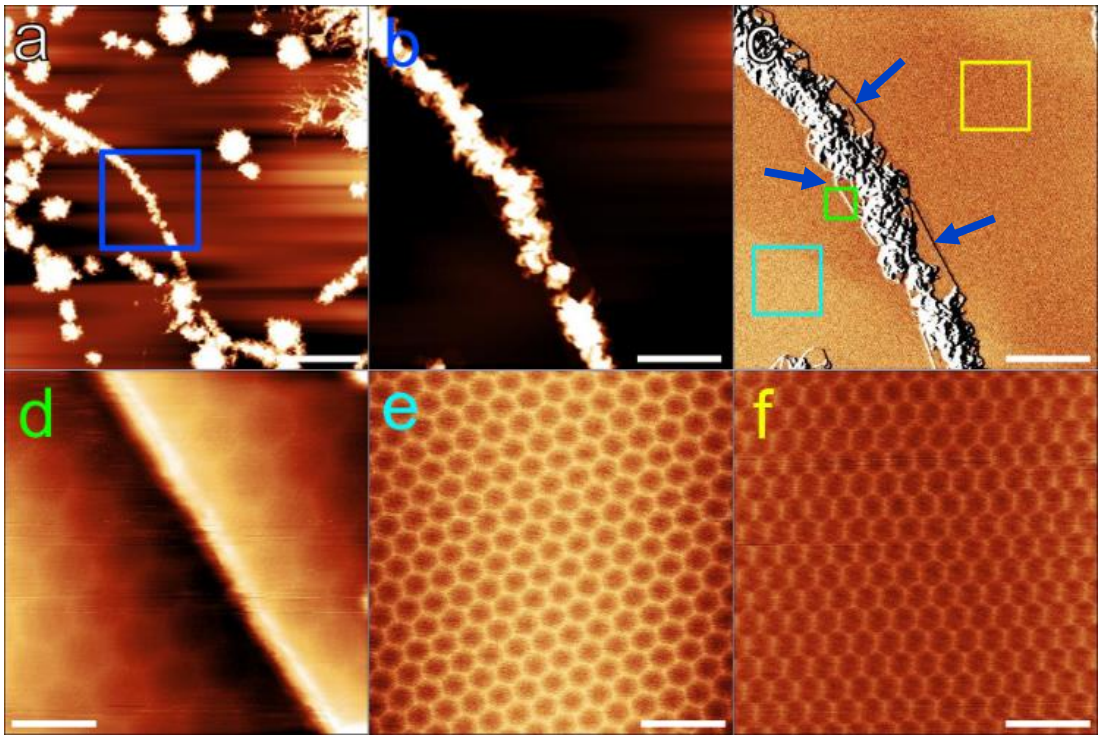

Figure 4.14: Images of a narrow deposit with additional graphene layers emerging from both sides. a) Topographic image shows the area where the narrow deposit lies. b-c) Topographic and phase channel images extracted from the area indicated by the blue box in a show additional layers at both sides of the deposit (blue arrows). Squares in green, turquoise and yellow indicate respectively the areas where (d-f) were taken. d) Edge of an additional double layer graphene sheet (up-right area) with a Moiré pattern aligned with the same ~14 nm period and in phase with the first layer. e) Moiré pattern on the area located at left side of the narrow deposit. f) Same as (e) on the right-side area. Scale bars: (a) 1 µm, (b) 200 nm, (c) 200 nm, (d) 20 nm, (e-f) 40 nm.

In some cases, graphene ribbons are formed on gaps between these narrow deposits. Figure 4.15a shows the neighbouring area of one of these ribbons and the deposits around it. The red square indicates the area where the phase channel image in Fig 4.15b was taken. In this image the edges of the ribbon can be appreciated. An additional graphene sheet with hexagonal edges lies at the top. In Fig 4.15c a topographic image reveals that the hexagonal sheet has two areas with different heights and a ~3 nm carbon deposit lies on one of the vertexes. The profile in d shows that the top layer in the ribbon is a third layer. Besides, the top layers in the hexagonal sheet are a third, where the hexagon does not overlap with the ribbon, and a fifth where it does overlap as numbers indicate. The Moiré pattern on the ribbon is aligned with the area belonging to the first layer located at the right of it but misaligned ~8º with the area on the left. Also, the Moiré on the third layer of the hexagonal sheet is aligned with Moiré at the neighbouring first layer while the fifth layer Moiré is aligned with the Moiré in the ribbon. Figures 4.15e and 4.15f show a ribbon in another flake with very similar features. There are also hexagonal sheets around it with the same layer distribution.

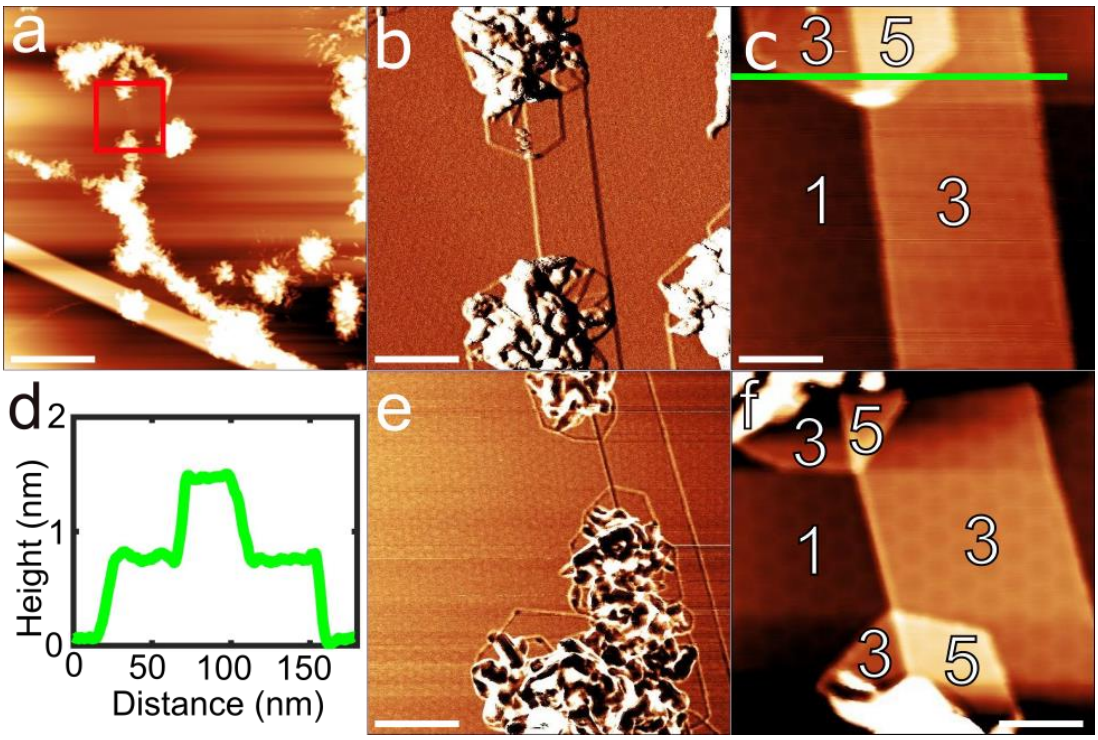

Figure 4.15: a) Location of a three-layer graphene ribbon. Square indicates scan area of (b). b) Phase channel image shows the edges of the ribbon and a hexagonal sheet at the top. c) Further magnification topographic image. Indexes mark the number of graphene layers in each area. d) Profile along the path marked in (c). e- f) Phase and topographic images of another ribbon with similar features in another flake. Both ribbons are ~100 nm across. Scale bars: (a) 500 nm, (b) 100 nm, (c) 40 nm, (e) 100 nm, (f) 40 nm.

Some samples show graphene domains separated by discontinuous gaps with carbon deposits in their edges. In Fig 4.16a one of these gaps runs across the right half of the image while on the left a trace of carbon deposits follows the same meandering path. As in previous figures, squares indicate the area where the next image was taken. Fig 4.16b shows in a higher magnification an area where the gap has disappeared leaving a trace of carbon deposits and small holes. The Moiré patterns in the domains at opposite sides of the trace are rotated ~5º with respect to each other.

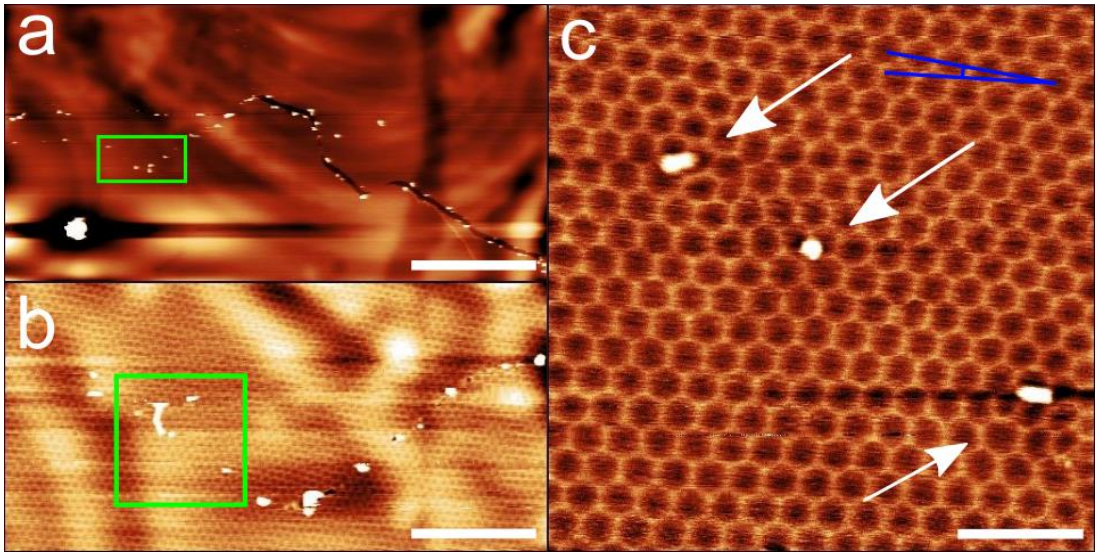

Figure 4.16: Images of two slightly rotated graphene domains partially coalesce leaving a trace of carbon deposits and topological defects. Green rectangle and green square in (a) and (b) show the area where the next image was taken. The sample was grown at 1630ºC. The blue angle in (c) indicates the 5º rotation between the Moiré patterns in the two domains and the arrows point at carbon deposits located on topological defects (white) and on areas with no defect. Scale bars: (a) 800 nm, (b) 200 nm, (c) 50 nm.

As explained in the background, rotation of Moiré patterns implies that the lattices are also rotated though a much smaller angle. Figure 4.16c shows topological defects around the carbon deposits, indicated by white arrows. The periodicity of the Moiré patterns in the two domains are roughly the same ~16 nm. The distribution of carbon deposits on the edges of the gap (Fig 4.16a) and areas where the two domains merge indicates that the two domains partially coalesced during growth and in this case the gap does not correspond to a crack formed post-growth.

Rotated Moiré patterns that coalesce leaving no gaps have been also found on other samples. Figures 4.17a and b show images of an area on a flake in a sample grown at 1500 ºC where two domains with slightly rotated Moiré patterns can be distinguished. Both Moiré patterns have periods ~22 nm. One of the domains occupies an area covering the bottom left quarter of the image in Fig 4.17a while the other occupies the other three quarters. A series of topological defects, indicated with white arrows, are distributed along the boundary between the domains. The patterns merge with a ~12º rotation marked with the dashed line in green in one of the domains and in yellow in the other. Figure 4.17b, shows in detail a defect in the frontier. The area is indicated with a blue square in Fig4.13a.

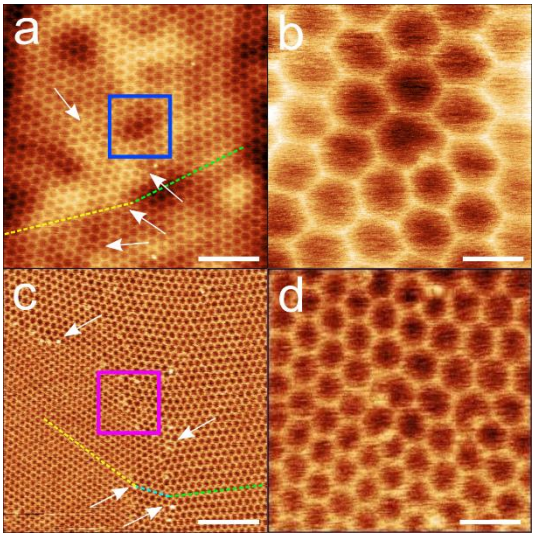

Figure 4.17: a) Slightly rotated graphene domains in a flake from a sample grown at 1500ºC. A series of topological defects lie in the frontier, indicated with white arrows. The dashed line with a different colour in each region, indicates the 12º Moiré rotation. b) Topological defect from the area indicated with a blue square in (a). c) Another example in a different sample grown at 1675ºC. In this case three domains coalesce. The dashed line highlights their orientation. d) In this case two topological defect are found. One of them is located at the centre of the image. Two cells away in the right-down direction lies the second one. Scale bars: (a) 100 nm, (b) 20 nm, (c) 100 nm, (d) 20 nm.

Figures 4.17c-d shown another example, from a different sample grown at 1675 ºC, of graphene domains with misaligned Moiré patterns that coalesce. In this case, the Moiré pattern in the left region has a ~14 nm period while the Moiré pattern in the region on the right has a ~16 nm. There is also a third region between them, although it is more difficult to distinguish it. The period of the Moiré in the middle region varies from 14 nm to 16 nm as we move from left to right. The misalignment between the left and right domains is ~30 º. The dashed line in the bottom of the image goes through the three domains with a different colour in each region. In Fig 4.17d, extracted from the area marked with a pink square in Fig 4.17c, two topological defects are present, one in the centre of the image, and a second, located only two Moiré cells away from the first one.

4.4 Summary

The results show that high temperature-MBE equipped with a resistively heated carbon filament source can be used to grow highly strained graphene on hBN. Graphene presents complex Moiré patterns with periods whose sizes range from the ~14nm period corresponding to the expected value for perfectly aligned unstrained graphene on hBN, to ~75nm corresponding to an overall $\Delta a_G/a_G \sim 1.46\%$ strain. Note that here Δa_G is the deviation of the lattice constant averaged over the Moiré period. A small variation of the graphene lattice constant across the unit cell has been reported in aligned G/hBN heterostructures[63] and is consistent with our findings.

The differences in the magnitude of strain between the topographically lower regions and the Frenkel-Kontorova domain walls give rise to split Raman peaks. The red shifting of both peaks increases with the Moiré pattern size as a consequence of increased strain in these regions.

Moreover, graphene layers grown at the highest temperatures ~1700 ºC present Frenkel-Kontorova domain walls, observed with AFM as topographically brighter lines, that are broken at specific points. In the areas between F-K walls, graphene reaches a 1.8% bi-axial strain and matches the hBN lattice. High resolution AFM images show that the broken F-K walls contain an extra row of carbon atoms running in parallel with them in the arm-chair direction and that the walls terminate at defects. Layers can relax post growth spontaneously or through scratching with an AFM tip, leaving cracked graphene layers were the period of the Moiré patterns is reduced. Anisotropically strained graphene layers are also present, which lead to Moiré patterns with periods that have different magnitudes in different directions.

A series of associated phenomena are also described: additional graphene layers that conserve the Moiré pattern, coalesced graphene layers with rotated Moiré patterns and elongated carbon deposits that end up abruptly with additional graphene layers shaped as ribbons.

These results show for the first time lattice matched graphene on hBN grown by MBE demonstrating the viability of this technique as a route for the introduction of strain in graphene.

5. Graphene growth on hBN using an atomic carbon source

The atomic carbon source SUKO-D consists of a 50μm thick tantalum tube filled with a mixture of ^{12}C and ^{13}C carbon powder[115] (Fig 5.1). The tube is 2cm long with an inner diameter of 5 mm. Once the carbon is introduced, the tube is sealed at the ends. Inside of the MBE chamber, the ends of the tube are connected to two electrodes. During growth, a direct current provided by a constant power output source travels through the metal tube provided that the electric tantalum, heating the carbon at 2200 K. The carbon is incorporated into the metal in the form of a solid solution. Then the atoms diffuse towards the external surface of the tantalum wall where they re-evaporate as atomic carbon. Essentially, the tantalum converts the carbon clusters inside the tube into carbon atoms before the evaporation occurs. Through this technique we can stablish a flux of predominantly atomic carbon (C_1) on the surface of hBN.

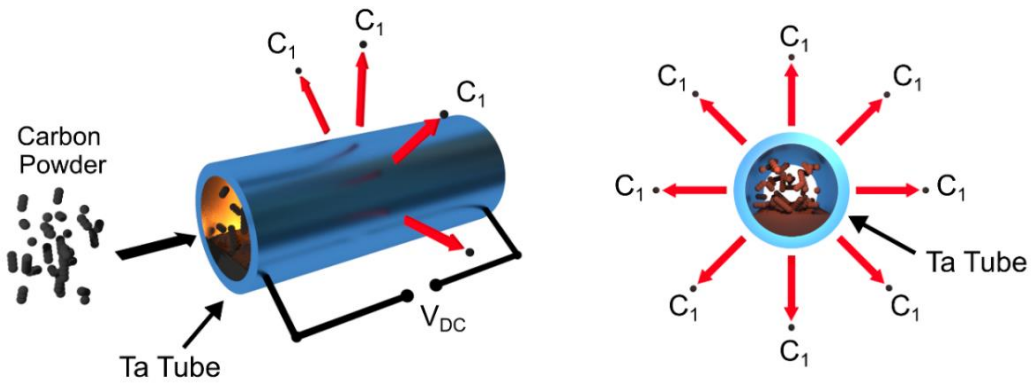

Figure 5.1: Schematic diagram of the novel atomic carbon source. Carbon powder is sealed into a thin-walled Ta tube, which is subsequently heated by a DC current.

The flux of carbon generated by this source has been studied and compared to the carbon flux generated by a graphite rod, using He droplets pick-up technique and mass spectrometry. The results indicate that the Ta sleeve source generates a flux of predominantly C_1 while the graphite rod produced mainly C_3 together with smaller quantities of C_6 (Fig 5.2a). The authors argue that the C_2 and C_3 peaks are due to formation of carbon clusters inside of the He droplets and that the number of carbon clusters increases with the number of He atoms in the droplets, which is independent of the carbon source itself. To support this data, they investigated the number of C_1 and C_3 ion counts vs the number of He atoms per droplet (Fig 5.2b). The probability of collisions between the droplets and carbon atoms increases with droplet size. As a result, the C_3/C_1 ratio should increase with the helium droplet size if the clusters are formed in the droplets. As can be seen in Fig 5.2b, this is indeed the case.

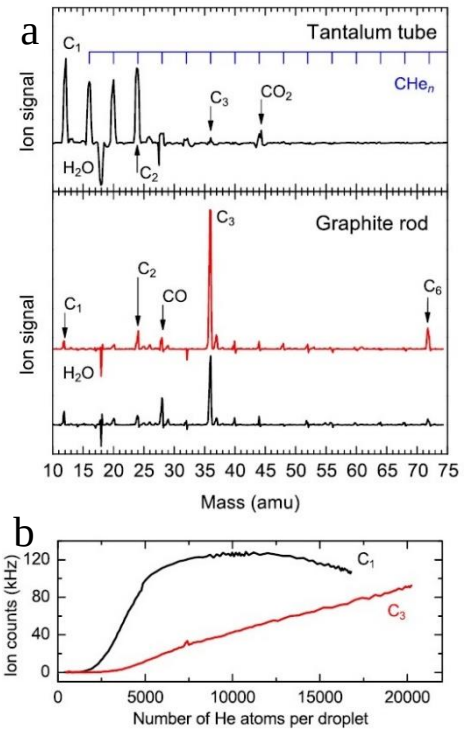

Figure 5.2: a) Mass spectra of helium droplets doped by ^{12}C produced by the atomic carbon source (upper frame) and by species evaporated by a graphite rod. The temperature of the graphite rod is higher for the spectrum in red. The mass spectra of undoped He droplets was subtracted for clarity. b) Ion signals vs He droplet size measure for C_1 and C_3 provide evidence of cluster formation inside of the He droplets. Extracted from [115].

5.1 Island growth

We began by exploring the growth at ~1400 °C. The growth conditions were later adjusted in order to obtain full coverage, slowly increasing the substrate temperature. A series of images in Fig 5.3 show the general appearance of an hBN flake with islands and small carbon deposits. Each image from a to d, is a double magnification zoom-in from the previous image. The brighter contrast lines correspond to hBN wrinkles are induced by the thermal-cycling process. The profile in Fig 5.3e shows their heights. Many of these wrinkles run along the hBN principal axes. Figure 5.3f shows a few profiles across deposits along the paths indicated by the coloured lines in Fig 5.3c. In Fig 5.3d a few small islands with some carbon deposits distributed along their surface coexist with larger islands.

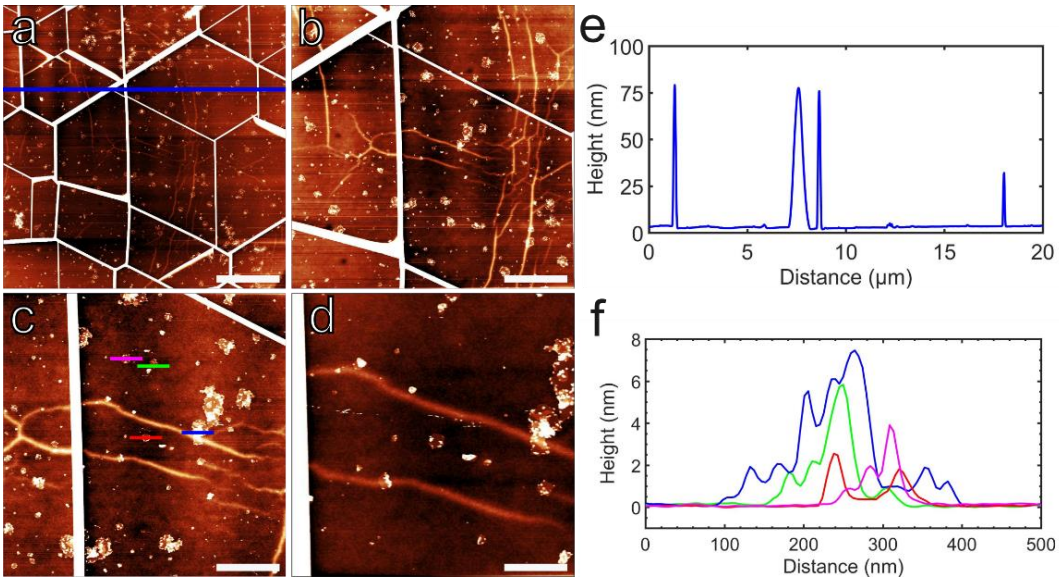

Figure 5.3: AFM topographic images of an hBN flake covered in small carbon deposits and graphene islands. The brighter lines correspond to wrinkles of the hBN flake induced by heating, running along hBN principal axis. An inset in image (a) shows the height of these wrinkles ~70 nm. Scale bars: (a) 4 μm, (b) 2 μm, (c) 1 μm, (d) 500 nm.

Figure 5.4 shows a comparison between AFM topographic images of graphene layers grown on hBN flakes grown under the same substrate temperature ~1400 °C but using different sources, the new atomic carbon source (Figs 5.4a-d) and the filament source (Figs 5.4e-f). Both layers were grown at substrate temperature of ~1400 °C although the times of deposition were adjusted in order to achieve a similar coverage: 5h in the case of an atomic carbon source and 1h for the filament source. The morphology of the layers grown on the surface shows some similarities but also differences.

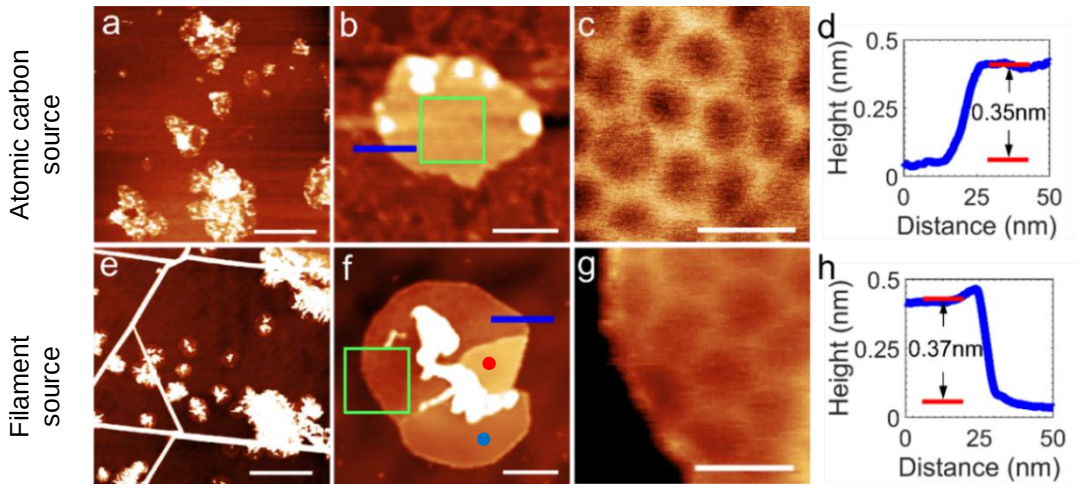

Figure 5.4: AFM topographic images of graphene layers on hBN grown at 1400ºC. Images (a-c) correspond to a sample grown using the filament source. The paths of the profiles in (d) and (h) are indicated respectively in (b) and (f) by blue lines. Images (e-g) correspond to a sample grown using the filament source. First and second graphene layers in (f) are indicated respectively by a red and a blue dot. Scale bars: (a and e) 500 nm, (b and f) 50 nm, (c and g) 20 nm.

Figures 5.4a and e show topographically high carbon clusters co-existing with small graphene islands. Higher magnification images on Figs 5.4b and f show graphene islands in detail. Their sizes are comparable but the distribution of the deposits on their surface quite different. For the filament source a series of deposits are situated close to the edges of the island. The sizes of these deposits are ~20 nm across and ~3 nm high. In the case of the filament source, a carbon deposit is typically located in the centre of the island, suggesting that these carbon deposits act as nucleation centres. The sizes of these deposits are considerably larger, ranging from 5 to 25 nm in height and from 50 nm up to 100 nm width in some cases. For the particular cases shown in Figs 5.4b and f, the deposit with the largest height on the atomic carbon source grown island is ~ 4 nm high while the central deposit on the island grown using the filament source is ~12 nm.

In Figs 5.4c and g higher magnification images taken respectively from the areas indicated by green squares on Figs 5.4b and f show Moiré patterns of 14 nm corresponding to the value expected for unstrained graphene which is orientationally aligned with respect to the underlying hBN. Profiles shown on Fig 5.4d and h provide evidence for monolayer height of the graphene. Their paths are marked respectively on 5.4b and f with blue lines. Blue and red dots on Figure 5.4f show respectively a second and third layer where the Moiré pattern is absent, most probably due to a rotation relative to the first layer.

Figure 5.5 shows AFM topographic images of different islands scanned on the same sample as the flake shown in Fig 5.4a-d, also grown at ~1400 ºC. These islands show similar characteristics. They have a round shape with small deposits that tend to be close to their edges. Most of the islands also show Moiré patterns with regular ~14 nm periodicities. In some cases, they present second and third graphene layers (indicated respectively by blue and red dots on Figs 5.2a and d) and edges which meet to form a sharp corner with a carbon deposit in the end (indicated by blue circles in 5.5b and d).

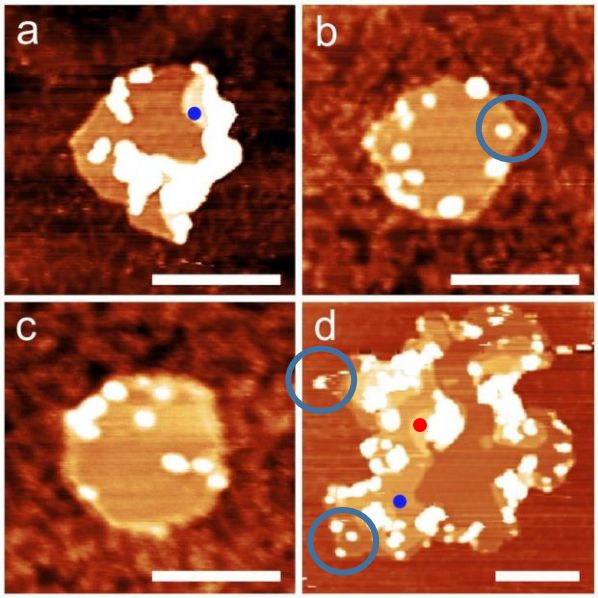

Figure 5.5: AFM topographic images of graphene layers grown on hBN with the atomic carbon source at a substrate temperature of ~1400 °C showing Moiré patterns with ~14 nm period. The carbon deposits tend to be more scattered across the graphene layers compared to those grown with the carbon filament source, where they are more clustered around the centre of the layer. Some islands present graphene double and triple layers (see areas indicated by a blue dots in (a) and (d)). All scale bars are 100 nm.

Islands and layers emerging from deposits on step edges on some samples discussed later, present pointy edges much more developed but with the same deposit at the tip. Most of the islands that have a significant fraction of the surface free of carbon deposits, such as those shown in Fig 5.5, have lateral sizes ~ 150 nm. Larger islands are also present, but their surface is mostly covered in carbon deposits as in Fig 5.4a.

As mentioned before, the islands coexist with larger deposits (Fig5.4a and e). Although their lateral sizes are quite similar, the

heights of these deposits are significantly larger when using the filament source. This suggests that the use of the atomic carbon source would be preferable for fabricating a cleaner graphene, which is free of clusters.

To investigate this, the maximum height of a hundred deposits (for each of the two samples grown at 1400 °C shown on Fig 5.4) have been manually measured and are presented as a histogram (Fig 5.6). Deposits with heights ranging from 5 nm to 25 nm are observed for the filament source while have a peaked distribution around 3 nm in the case of atomic carbon. Note that deposits on islands for both samples were also included.

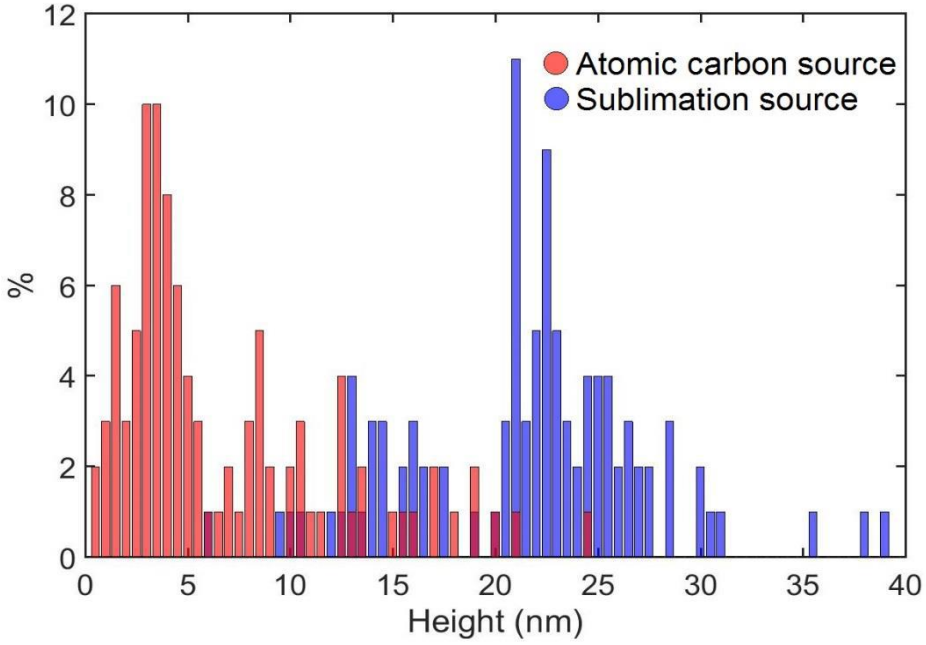

Figure 5.6: Histogram of maximum height of carbon deposits for the samples shown in Fig 5.4 grown using the atomic carbon source (red) and the filament source (blue).

At a higher substrate temperature ~1560 °C islands with larger sizes (~400 nm across) are formed. Figures 5.7a-d show examples of these islands with their corresponding higher magnification images next to them, respectively on Figs 5.7e-f. The areas magnified are indicated by blue squares. The deposits on the edges of the islands have the same dimensions as the ones in the smaller islands and slightly pointed edges are found on some of them as well, indicated by green circles on Fig 5.7b-c. On many of these islands regular Moiré patterns with ~14 nm periodicities can be observed (Fig 5.7e).

Other islands present dislocations where a row of the Moiré pattern terminates (Fig 5.7f) leaving Moiré cells with a local coordination of 5 and 7 rather than 6. These dislocations have been reported before[64,116] and usually appear at the frontier where domains with rotated Moiré patterns coalesce leading to a long range curvature of the pattern. Figure 5.7g shows a high magnification image of the island in 5.7c. The Moiré pattern can only be observed in the top side of the image. Perhaps, the graphene layer in the bottom domain is rotated with respect to the underlying hBN by an angle large enough for the Moiré period to drop and not be visible. Nevertheless, there is no sign of any defect on the frontier which is expected when two rotated graphene layers coalesce. Lastly, Figure 5.7h shows a higher magnification image from the surface of the island in Fig 5.7d where two clearly different Moiré patterns are divided by a vertical boundary, as indicated by a dashed black line. The Moiré pattern on the right hand side of the image, which is much distorted, has periodicities that range from 13 nm to 20 nm depending on the direction. It appears that there is a larger strain in the vertical direction compared to the horizontal. Black arrows indicate a small ~10° rotation between the Moiré patterns at the high and low areas. In addition, at the left side of the image a ~7 nm Moiré pattern is present, indicated by green arrows, which is also rotated with respect to the distorted Moiré patterns on the right side. Such small periodicity can only be obtained by a ~1.5° rotation of graphene with respect

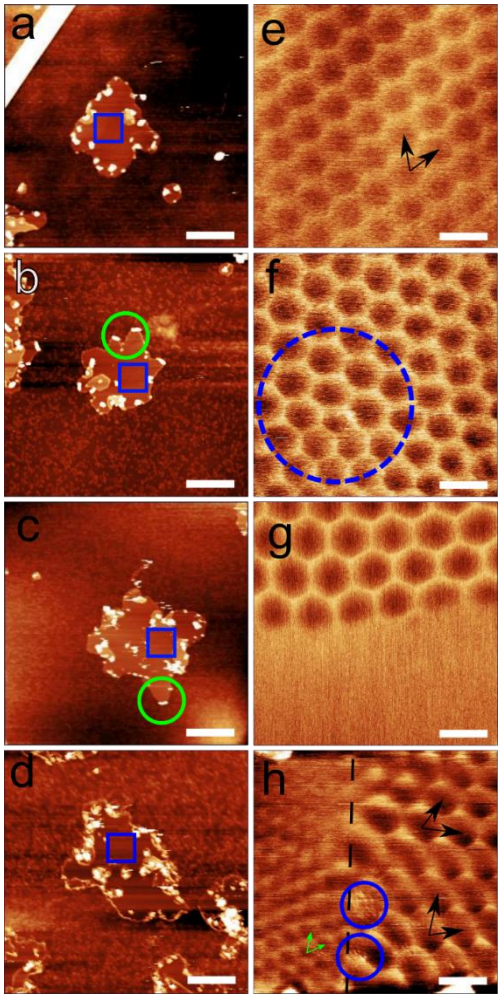

Figure 5.7: AFM topographic images of graphene islands grown at ~1560 °C (a-d). Their sizes are ~ 400 nm across and their borders are quite regular although some pointy edges, indicated by green circles, are also found. The blue squares indicate the areas where the corresponding higher magnification images (e-h) where obtained. The Moiré patterns found on their surfaces show different behaviours: regular Moiré patterns (a), slightly distorted with defects that alter the local coordination of the Moiré unit cell (b), domains where the Moiré pattern is absent with no trace of defects (c) and strained ~20 nm Moirés coexisting with rotated ~7 nm Moirés separated by a frontier with defects. Scale bars:(a-d) 200 nm, (e-h) 20 nm.

to the underlying hBN. In this case, defects are present in the frontier between the two domains. These are indicated by two blue circles on the lower area of the image. Moiré patterns with periodicities larger than 14 nm have not been observed in islands grown using the filament source. Since the distribution of the carbon deposits on the surface of these islands was central rather than scattered along the edge, we speculate that the deposits found on the edges of the islands play a role in maintaining the strain in a similar way, although in a smaller scale, as larger deposits on step edges and defects maintain the strain of full growth graphene layers on hBN.

Although many samples grown using the atomic source show islands with relatively regular edges, on other samples we find islands were the sharp corners shown on Fig 5.8 are much more developed, forming narrow strips that emerge from the islands. At the end of these spikes there is usually a small carbon deposit. The deposits on the edges seem to play a role in the formation of the spikes under certain conditions. It is difficult to find a precise reason for this modification since the growth with the atomic carbon source has a low reproducibility and this type of island is found on all ranges of substrate temperatures. The Moiré patterns on their surface show the same features described earlier on islands with more regular edges. An example similar to that shown on Fig 5.7h is also found on the surface of the island on Fig 5.8d magnified in Fig 5.8e.

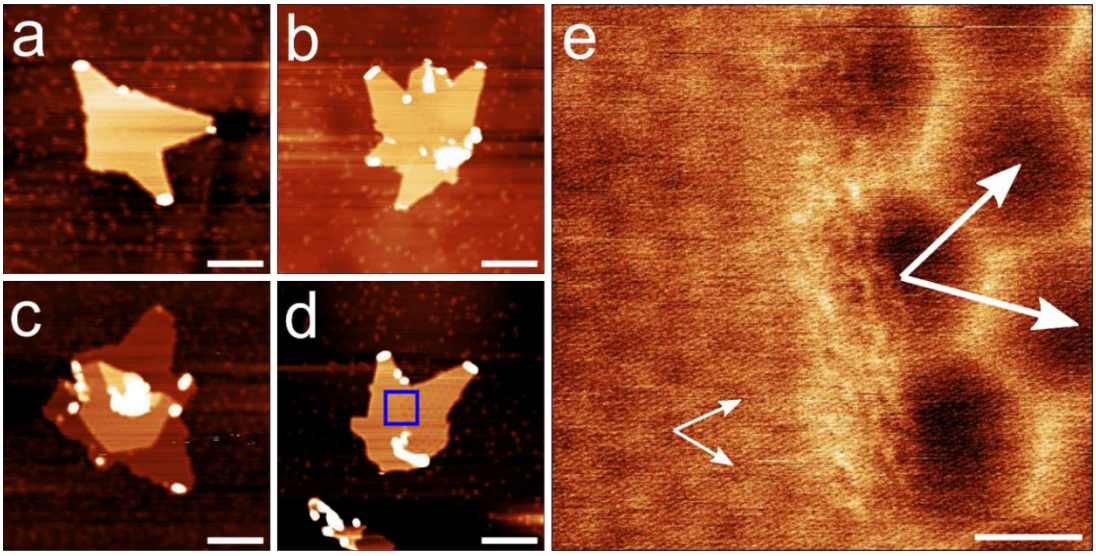

Figure 5.8: a) AFM images of an islands with star-like shape. At the end of the narrow strips deposits of ~30 nm across and ~2 nm high are usually found. Island on (c) presents a second layer with hexagonal shape with borders running along the zig-zag direction. There is also a third layer in the centre next to a deposit. Image (e) shows a higher magnification image taken from the area indicated by a blue square on (d). The island presents two Moiré patterns with 15 nm and 7 nm periods rotated with respect to each other and divided by a straight frontier. Moiré cell vectors are represented by white arrows. Scale bars: (a-d) 100 nm, (e) 10 nm.

The right-hand side of the image presents a rather regular ~14 nm Moiré pattern while at the left side there is a fainter ~7 nm Moiré. The patterns are slightly rotated with respect to each other. At the boundary between the two domains there is a continuous distribution of defects.

Carbon deposits also nucleate on hBN step edges forming lines of several tenths of µm in length. Graphene layers emerging from these deposits can be observed. Figure 5.9a shows two of these lines of carbon deposits running in diagonal on a sample grown at ~1400 °C. Islands with rounded edges can be observed around these deposits. The borders of the graphene layers that emerge from them are also round, in a similar way as the islands. A profile taken across the line of deposits, indicated by a blue line in Fig 5.9a is shown on Fig 5.9d. The height of the line of deposits is ~8 nm high. A higher magnification image on Fig 5.9b, taken from the area indicated by a red square, at the bottom of the image shows in detail these emerging layers. The inset, whose path is marked by a cyan line, indicates the height of a monolayer. Figure 5.9c shows another line of deposits grown on a step edge on a sample that presents islands with pointy edges. The layers emerging from these deposits also present a similar morphology. A profile with a path indicated by a green line shows that in this case the height of the deposit line is ~4 nm. At the end of the sharp corners, small carbon deposits are typically found, as discussed above.

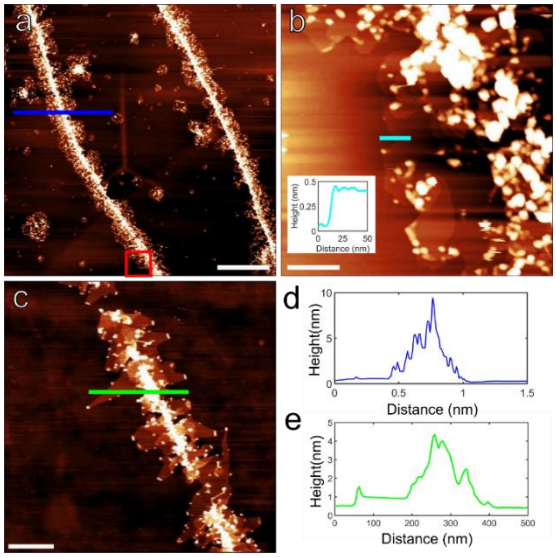

Figure 5.9: AFM topographic images of carbon deposits growing at hBN step edges. (a) Two of these lines running in diagonal among graphene islands. The path in blue corresponds to the profile in (d). (b) Higher magnification image of the edge of one of these lines of deposits marked by a red square in (a). The edges of the layers emerging from the deposit line are similar to the edges of islands growing from defects. A profile along the path marked by a cyan line is shown on the inset, indicating the height of a graphene monolayer. (c) A line of deposits with sharp corners. Notice the small deposits at the ends of the spikes, looking very similar to those in the islands described before. (a) 1µm, (b) 100 nm, (c) 200 nm.

X-ray photoelectron spectroscopy (XPS) is a technique based on the photoelectric effect. The kinetic energy of an emitted photoelectron is equal to the difference between the photon energy, and the binding energy of the electron. Since the binding energy is characteristic of the element, this technique allows characterization of the elements in the sample. Figure 5.10 shows wide scan X-ray photoelectron spectroscopy (XPS) spectra over the full energy range for two graphene samples grown with the atomic carbon source (red and blue lines) and one reference sample (green line). The measurements were obtained by Professor Christopher Mellor. A hBN/sapphire wafer was heated in the MBE chamber up to growth temperatures in vacuum, but with no atomic carbon flux. XPS detects the elements in the uppermost 10 nm of a surface and Al, O, C, B, and N are detected on all samples. The XPS tantalum (Ta) signal was observed on all studied graphene layers grown with the atomic carbon source. The right inset is a high sensitivity spectrum for each sample over the Ta 4d spectral region, clearly showing the Ta doublet at 231.0 and 242.5 eV on the surface of all graphene samples except for the reference wafer. The Ta concentration was 0.2 ± 0.1 atomic %.

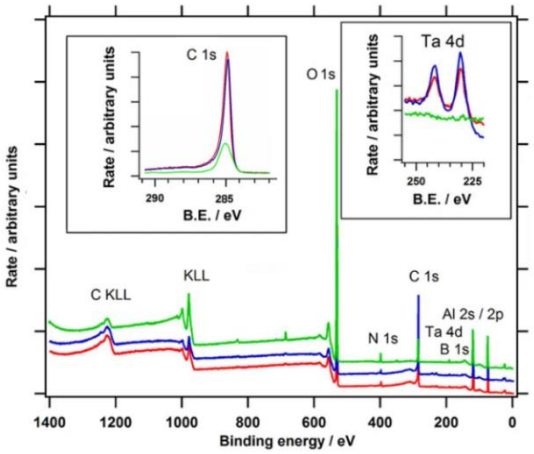

Figure 5.10: XPS wide scan spectra over a full wide energy range for two graphene samples grown for 3 h and 5 h and one reference sample. The insets show the C 1s (left) and the Ta 4d (right) high sensitivity spectra for the same three sample areas. The later indicates the presence of Ta on all except the reference sample.

Carbon is detected on the reference sample, but the intensity is lower and peak shape is significantly different to the 3 h and 5 h deposited samples. The C 1 s peaks appear at ~284.5 eV and are asymmetric to the high binding energy side, with a long ‘tail’ to high binding energy (left inset), which is consistent with graphitic/graphene-like bonding. (sp2 bonding), whilst the detected carbon peak on the reference sample is at ~284.7 eV and more symmetrical. The broader peak suggests sp3 bonding dominates in this case. (For this comparison the spectra were further charge corrected to the N 1 s substrate peak at ~397.8 eV.) We propose that it is possible that some adventitious carbon exists on the surface of the reference sample prior to heating and this has reacted or stayed adsorbed onto the sapphire and/or the hBN surfaces.

5.2 Monolayer growth

Samples grown with the atomic carbon source using a substrate temperature below 1600 °C are either completely covered in carbon deposits or have a partial coverage of graphene. In the range from 1600 °C to 1680 °C full layers of graphene are found with Moiré patterns larger than 30 nm or cracked with relaxed graphene layers. Figure 5.11 shows images of two samples (one in each column) grown consecutively at 1640 °C. The power applied to the source was the same for both samples but the time of growth was 5h for the sample shown in the first column while 3 h for the sample in the second column. Figures 5.11a and d show both samples have a high coverage of carbon deposits. The heights of these deposits compare with those discussed earlier range between 5 nm and 15 nm. Areas between deposits are completely covered in graphene and continuous Moiré patterns can be seen in the phase channel images in Fig 5.11b and e. The images are respectively taken from the areas indicated by blue squares on Fig 5.11a and d. The Moiré patterns are highly distorted in both samples with different sizes and orientations along the surfaces, probably due to on the large amount of deposits surrounding these areas. Higher magnification images in Fig 5.11c and f taken respectively from the areas indicated by green squares in Fig 5.11b and e show the Moiré patterns in detail with white arrows that indicate their Moiré vectors. These periods are different depending on the direction in either case which implies that the strains are not uniform.

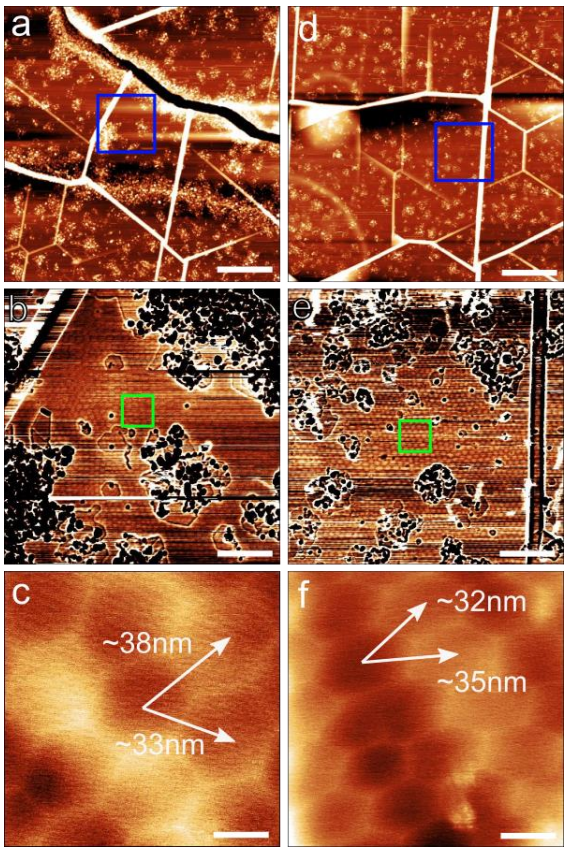

Figure 5.11: Images of two samples grown at 1640 °C for 5 h (left column) and 3 h (right column). Coloured squares indicate the areas where the next images were taken. a,d) Both samples present a large fraction of their surface covered in carbon deposits. b,e) Phase images show continuous highly distorted Moiré patterns between deposits. c and f) Moiré patterns with periods above 30 nm, indicated by white arrows. Scale bars: (a and d) 1µm, (b and e) 200 nm, (c and f) 20 nm.

Another sample grown at slightly higher temperature, 1680 °C, shows a lower density of deposits and full coverage but in this case the graphene layer is cracked with domains of typical sizes ~500 nm across. Figures 5.12a and b show the same area with the contrast adjusted to see respectively the deposits and the cracks on the surface. Fig 5.12c is a zoom of the blue square in Fig 5.12b. Figure 5.12d shows more closely a crack in a nearby area. Although there are less big carbon deposits, there are a large amount of small deposits of ~2 Å in height partially covering the Moiré pattern. On the upper side of the crack it can be appreciated how the orientation of the Moiré pattern, indicated by blue arrows, slightly shifts between the areas at right and left. The Moiré periods in this area range from 14 nm to 18 nm. On the other hand, the domain below the crack on the bottom presents an area, indicated with a green arrow, where the Moiré pattern acquires a wave-like shape. This kind of Moiré pattern has been observed before next to another crack in a sample grown using a filament source. In one direction the period diverges corresponding to strain ~1.8% while in perpendicular to the crack the period is ~14 nm.

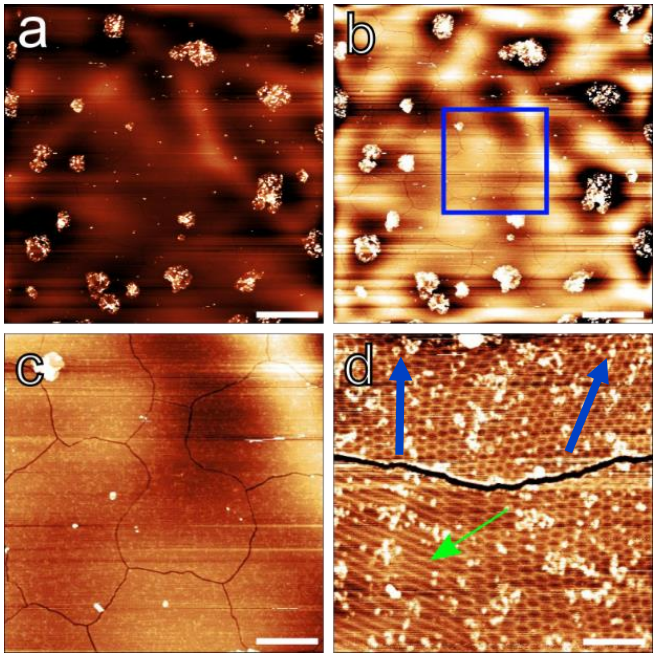

Figure 5.12: Topographic mages from a sample grown at 1680 °C showing fewer carbon deposits compared to Figure 4.10. a) Contrast was adjusted to highlight deposits. b) Contrast was adjusted to highlight graphene cracks. Blue square indicates where image (c) was taken. c) Domains between cracks show typical sizes ~500 nm. d) Higher magnification image showing distorted patterns partially covered by smaller ~2 nm deposits. Above the crack blue arrows indicate the orientational shift of the Moiré pattern. Scale bars: (a and b) 1 µm, (b) 300 nm, (d) 100 nm.

5.3 Lattice matched graphene

Two samples grown at the highest substrate temperatures, 1690 ºC and 1730 ºC showed flakes with lattice matched graphene. The best images were obtained from a flake grown at 1730 ºC. A mosaic image was elaborated arranging 1×1μm^2 phase channel images (Fig 5.13). Moiré patterns and domain walls in phase channel appear with darker contrast compared to the background. The image shows a hBN step edge covered in amorphous carbon running diagonally.

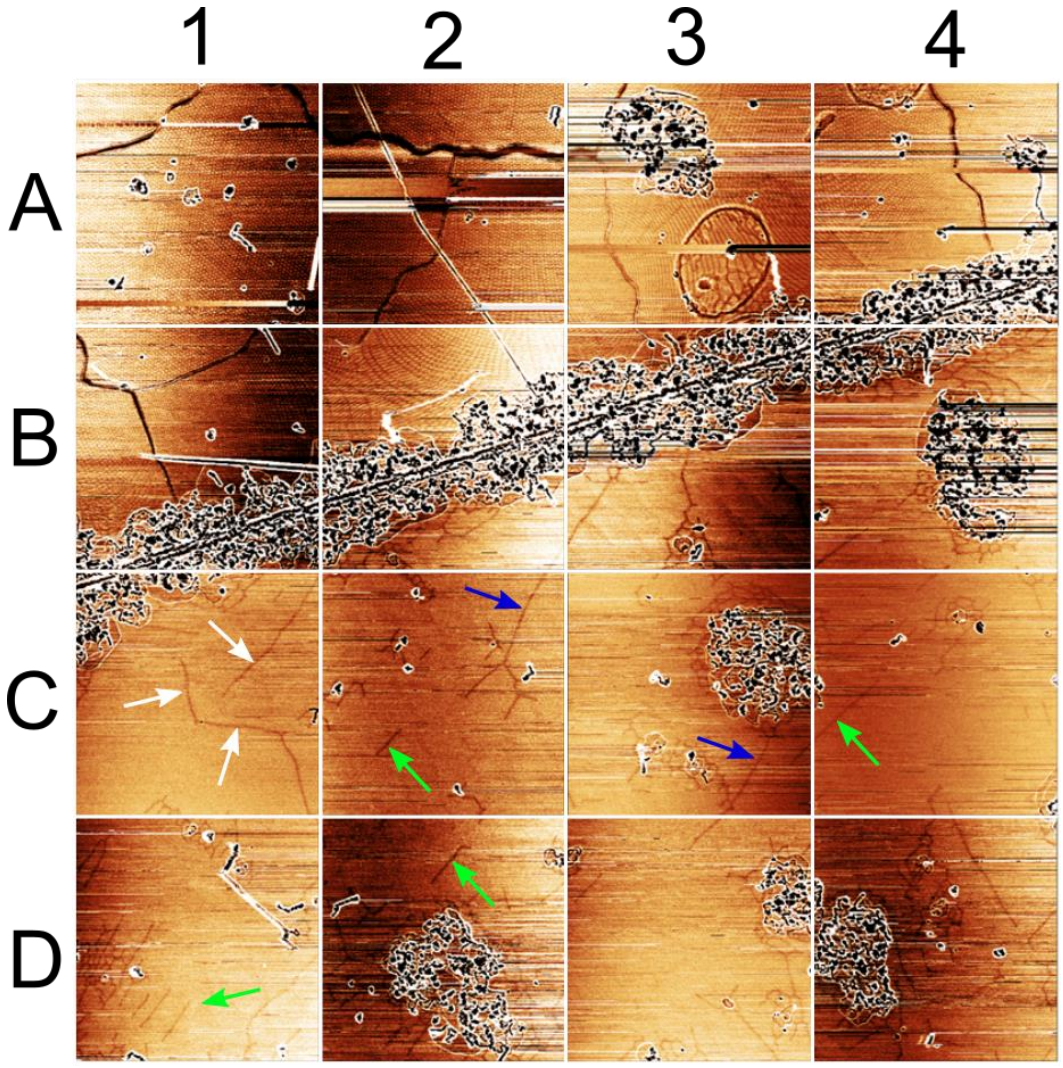

Figure 5.13: Mosaic formed from 1x1 μm^2 phase channel images. A hBN step edge covered in amorphous carbon divides two areas. Above the step, a graphene layer is cracked and relaxed exhibiting ~16 nm period Moiré patterns in most of the areas although there are also some distorted Moiré patterns as in the 2B quadrant. Below the hBN step, Moiré patterns only appear in small areas around carbon deposits and lines which presumably correspond to Frenkel-Kontorova domain walls are present leaving areas where the graphene layer is lattice matched. Interestingly, most of the domain walls form 120º angles (indicated with white arrows) but other walls run along other directions (indicated with blue arrows). In addition, domain walls that are not connected to Moiré patterns or carbon deposits appear in several areas (indicated with green arrows).

The graphene layer located above this step edge is cracked leaving isolated domains. Most of these domains show Moiré patterns with periodicities ~16 nm, similar to images 1A and 1B. There are also areas where the Moiré is distorted due to anisotropic strains, as on the 2B image, next to the step edge. The Moiré also appears quite distorted on top of a hBN bubble on 3A. These bubbles, which arise from debris trapped between the hBN flake and the sapphire substrate, have been observed previously and are not related to the growth of graphene. Below the step, the Moiré is absent except around in small areas around carbon deposits, and a series of lines that presumably correspond to Frenkel-Kontorova domain walls run along the surface. Their lengths in some cases are up to 1µm. In contrast to the domain walls observed on lattice matched graphene obtained through the use of a filament source, these do not always form 120º angles with other domain walls, which indicates that they do not necessarily run along principal axis of graphene. For example, the three domain walls located at 1C in Fig 5.13 meet at angles close to 120º with each other (indicated by white arrows) but the domain wall that runs from the carbon deposit at 3B and bifurcates at 2C (indicated by a blue arrow) does not run parallel to any of these walls. Another interesting feature, not observed in the lattice matched graphene grown using a filament source are domain walls that are not connected to any deposits or Moiré patterns, which leaves two ends (indicated by green arrows).

A profile taken in AC mode from one of the Frenkel-Kontorova domain walls (Fig 5.14) indicates that their height is ~40 pm, which agrees with the height of F-K domain walls on lattice matched areas on graphene grown by using a filament source.

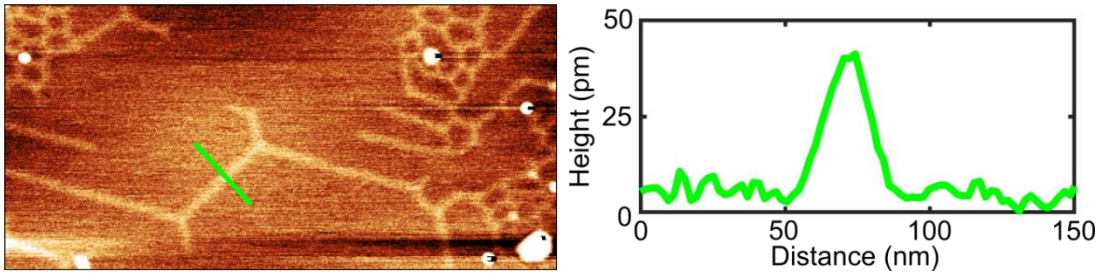

Figure 5.14: Profile taken across a Frenkel-Kontorova domain wall in AC mode shows a height ~40 pm. Path is indicated by green line in (a).

An area where F–K domain walls are present was scanned by James Thomas using conductive AFM. The sample was grown using an atomic carbon source. During the scan, the tip was kept in contact with the surface, with a constant applied force and at constant −50 mV sample bias. The image (Fig 5.15b), is a map of the current that flows

through the AFM tip as it scans the surface. A current profile in Fig 5.15e shows that the current flow is increased by a factor ~3 when the probe is above the F–K domain walls as compared with the neighbouring lattice-matched regions and even higher where the walls terminate at defects in the graphene lattice (the bright point like features in Figure 5.15). The path of this current profile is indicated by a blue line in Fig 5.15b. Note that the network of domain walls is also resolved in topographic contact mode images which are acquired simultaneously (Figure 5.15c). A topographic height profile extracted from a contact mode image (Figure 5.15d) shows that the cantilever probe is withdrawn by 47 ± 5 pm as it passes over the domain wall; this is close to the effective heights determined in F-K walls on lattice matched graphene grown using a filament source (Fig 4.6) as well as in the wall measured in this chapter in AC mode and provides evidence that the probe-sample separation is approximately constant during the electrical measurements. The increase in current must therefore be due to a variation in the intrinsic electronic properties of graphene in the nanoscale regions close to the domain walls. A higher current flow from the AFM probe to the surface when it is positioned above a F–K domain wall may be due to a higher density of states in these regions. The value of the energy gap which is formed in lattice-matched graphene/hBN has been predicted[71] to be ~50 meV, close to $2k_BT$ at room temperature. The lower currents measured above the lattice-matched regions are consistent with a lower density

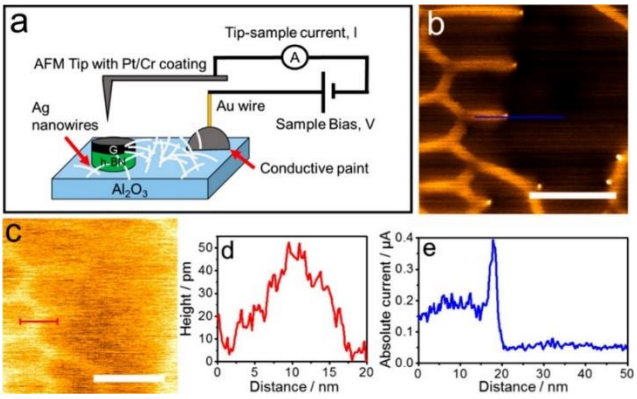

Figure 5.15: cAFM images showing differences in conductivity of lattice-matched graphene, F–K lines, and defects in the graphene lattice. a) Experimental setup used for measuring the graphene electrical properties. The hBN/graphene heterostructure is grown on a sapphire substrate and followed by Ag nanowire deposition. This provides a conducting pathway across the insulating sapphire surface to an electrical contact allowing the application of a sample bias and cAFM measurements to be recorded using a Pt/Cr coated tip. b) cAFM image recorded with a sample bias of −50 mV showing high current flow above F–K domain walls and very high current at bright pointlike features due to defects in the graphene lattice. c) Contact mode AFM height trace image recorded simultaneously with (b). The scale bar is 50 nm in (b-c). The colourmap contrast ranges from 0.03 μA to 0.41 μA in (b) and spans a range of 280 pm in (c). d) Height profile averaged along the line with a width of 20 pixels indicated in (c). e) A current profile measured along the line shown in (b). The current measured at the termination points is ~2.5 times the value recorded at the F–K boundaries, when measured relative to the current within the intermediate regions.

of states which might be expected in the presence of a band gap which is of order a few times k_BT. Interestingly, the lattice-matching is absent in the graphene folds which form the F–K domain walls and the band gap in these regions would be expected to be smaller or completely absent. Although there has been no detailed study of the quantum properties of F–K domain walls embedded in lattice-matched graphene, the one-dimensional symmetry is likely to promote analogies with conduction in carbon nanotubes.

We also observe enhanced current flow close to the topological defects which terminate the F–K lines; here the difference in conductance is much greater, six times, than over the lattice-matched regions. From a chemical perspective, there is at least one carbon atom which is not bonded to three neighbouring carbon atoms at these defect sites and it is possible that these unsatisfied bonds lead to a higher local density of states.

5.4 Summary

The results shown in this chapter demonstrate the viability of MBE growth of graphene/hBN heterostructures by using an atomic carbon source composed of a Ta tube filled with carbon powder.

At sub-monolayer stage, graphene islands present a different morphology compared to islands grown using a filament source. Small carbon deposits are distributed along the edges of the islands, in contrast to the deposits found on islands grown with a filament which are clustered around the centre. In some cases, the edges of the islands form narrow strips that emerge from the islands and terminate at a small carbon deposit.

Although the Moiré patterns on most of the islands have ~14 nm periods, larger periods (up to ~20 nm) are also present. These larger Moiré patterns, which indicate the presence of a positive overall strain, do not appear on islands grown with a carbon

filament. Perhaps the carbon deposits located at the edges of the islands play a role in the preservation of strain.

In addition, few islands present coalesced graphene domains with much different periods (for example 7 nm and 15 nm). The 7 nm period indicates that the graphene is not aligned with hBN.

At monolayer growth most graphene layers present regular Moiré patterns with periods ranging from ~14 nm to ~38 nm. Cracked and relaxed layers with ~14nm Moiré periods, similar to that grown with the filament source are also shown.

Lattice matched graphene is observed on samples grown at the highest temperatures. The Frenkel-Kontorova walls run mainly along principle crystallographic graphene axis. Nevertheless, distorted and curved walls are also present.

Conductive AFM measurements on lattice matched layers show an increase of the current flow at the Frenkel-Kontorova walls compared to the topographically lower areas. This is consistent with the formation of a small band gap ~50 meV which was already theoretically predicted.

The concentration of Ta sublimated from the source was investigated with XPS technique. The spectrum indicates a concentration of 0.2 ± 0.1 atomic %, but we cannot determine where the Ta is located in the sample or if the Ta is involved in the formation of deposits on the edges of graphene islands.

It is important to note that the growth with the atomic carbon source is not reproducible. The carbon flux depends on the amount of material inside the tube, which is spent during growth. For this reason, we find samples with different amounts of material, even if the conditions of growth were the same.

6. Graphene growth on hBN using an e-beam source

In this chapter we investigate the growth of graphene on hBN using a SUKO EBVV e-beam source. Electrons are generated by thermionic emission from a tungsten filament. Then they are accelerated by a potential difference of 5kV between the filament and the target and curved 270° by a perpendicular magnetic field provided by copper coils in order to be properly directed towards the target (Fig 6.1a). Through this process, electrons obtain a high kinetic energy which is transferred into the target raising its temperature. In order to prevent the melting of the copper holder, the piece is water cooled by a Ω-shaped water channel.

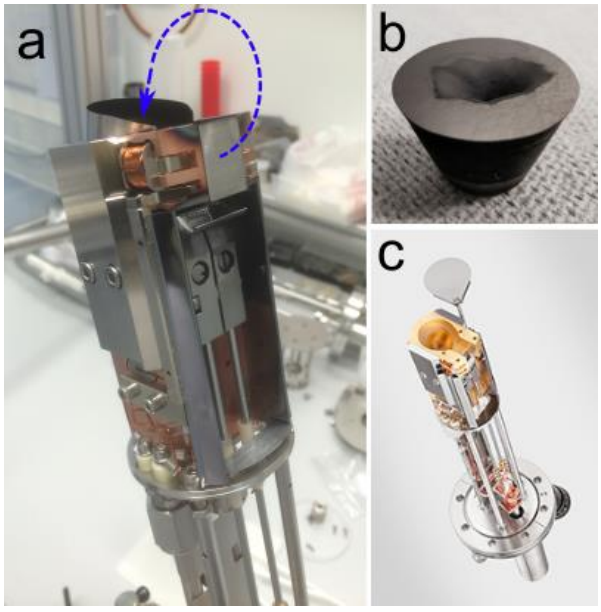

Figure 6.1: a) Photograph of the SUKO EBVV e-beam. Blue arrow indicates the path of the electrons into the crucible. b) Graphite block used as source. The surface appears eroded after use. c) Image of the flange extracted from the company webpage: https://www.mbe-komponenten.de.

The target consists of a block of pyrolytic carbon (Fig 6.1b) which rests the holder. Given that the carbon sublimes mainly around the point of impact of the e-beam, eroding the surface of the target, the beam needs to be spread around the exposed surface of the block.

This is done by continuously changing the magnetic field that governs the trajectory of the beam in a way that the point of impact describes Lissajous curves delimited by a rectangle in the surface of the target. In order to achieve a roughly consistent carbon flux, the current applied to the source was 200 mA when growing the first sample with a fresh target and increased by 50mA for each subsequent sample till the material in the target was spent.

6.1 Island growth

Graphene islands grown at the early stages with an e-beam source present a morphology similar to the islands grown using a filament source. Figure 6.2 shows images of a sample grown at a substrate temperature of 1400 °C for 30 minutes. On Fig 6.2a carbon deposits along hBN step edges and spaced small ~200 nm islands are present. The central carbon deposits of the islands and the deposits on the step edges have heights ~10 nm. A higher magnification image taken from the area indicated by a blue square shows two graphene islands in Fig 6.2b. The larger island has on the bottom left side a peculiar distribution of deposits forming a loop, not seen on islands grown with the other two sources. This island also has second and even a third layer which is indicated by a green arrow. Profiles showing monolayer and bilayer graphene heights are taken along the paths indicated in blue and green are shown respectively in Fig 6.2e and f. A higher magnification image taken from the area indicated by a yellow square is shown on Fig 6.2c. The edges of the island are round emerging few tenths of nm from the deposits. The Moiré pattern can be observed only on the right side of the island (Fig 6.2d).

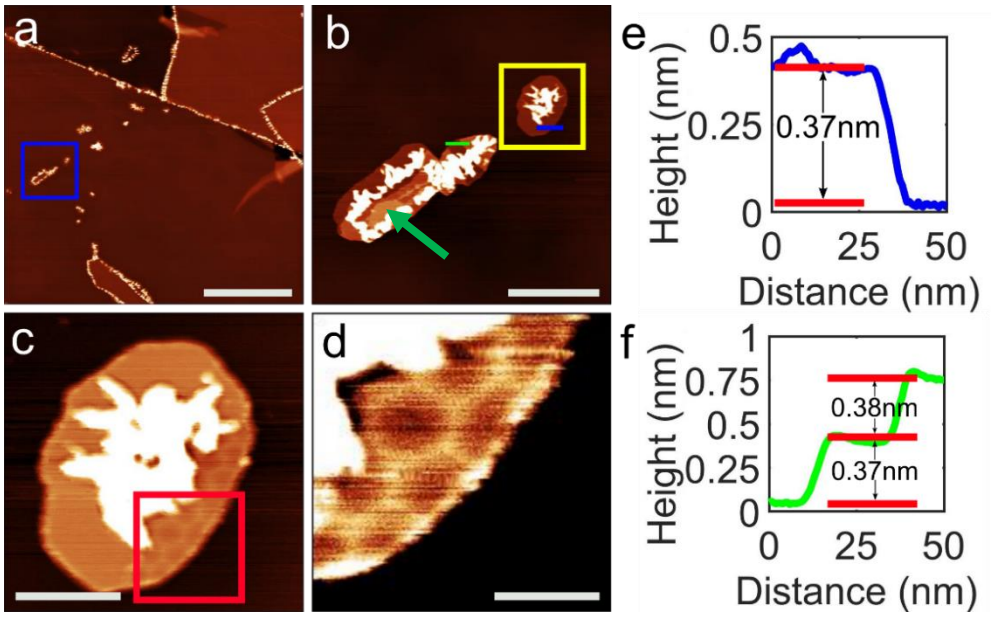

Figure 6.2: A series of increasing magnification images shows islands on an hBN flake after grown at 1400 °C for 30 minutes. The morphology of the islands is more similar to those growth using a filament source, with central carbon deposits with ~10 nm in height and graphene layers with 14 nm Moiré patterns. Second and third layers are also found. Scale bars: (a) 1 µm, (b) 100 nm, (c) 50 nm, (d) 20 nm.

Figure 6.3 shows images of another sample grown also at 1400 °C but for 4 hours, although the current supplied to the source was ~1/3 lower. The number of islands has increased considerably although their sizes are similar to those of the previous sample. Figure 6.3a shows the distribution of the deposits along the surface. The heights of the deposits on the step edges and in the islands is also in the order of 10 nm. Higher contrast lines in diagonal and in vertical close to the centre of the image correspond to the hBN buckling due to the thermal cycling.

Figure 6.3b taken from the area indicated by the blue square in Fig 6.3a shows the islands. Most of them present central deposits with a round graphene monolayer growing from them. On the top right corner of the image a terrace has been completely covered in graphene. Second layers are emerging from deposits in this area. The island marked with a green square is shown in Fig 6.3c It has a similar morphology as the large island in Fig 6.3b although in this case the deposits are distributed in 6 clusters. The island presents a ~14 nm Moiré pattern. Profile shown in Fig 6.3d measuring the height of the monolayer is indicated by a blue line. A nearby area in Fig 6.3e presents similar deposits. This image also indicates the location with a yellow square of the island in Fig 6.3f The deposit on its centre is much smaller ~0.4 nm. The ~14 nm Moiré pattern can be appreciated all along the surface of the island.

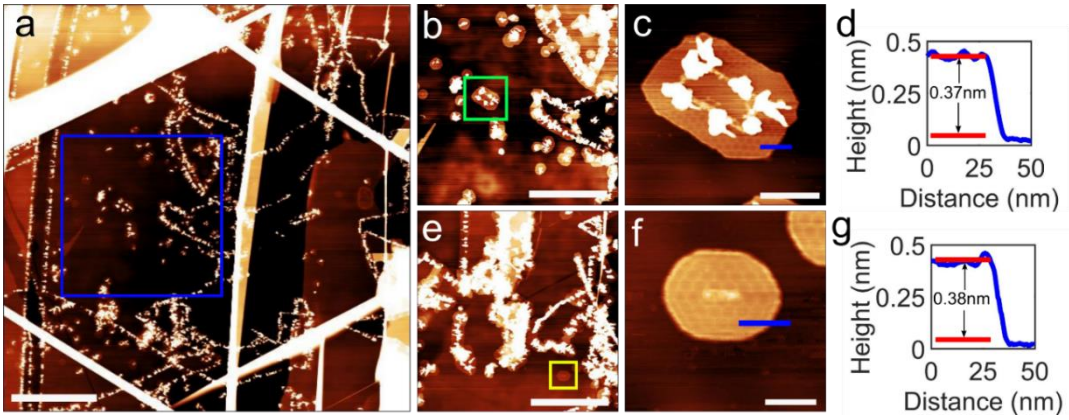

Figure 6.3: AFM images of a hBN flake grown at 1400 °C for 4 hours using an e-beam source. a) Small graphene islands emerge from deposits on step edges and defects. Image (b) is taken from the area indicated by a blue square in (a). Image (e) corresponds to an area just above the one shown in image (a). Images (c) and (f) extracted respectively from green and yellow squares in (b) and (e) show two islands with slightly different morphologies compared to the round and centred around a deposit, present in most of the islands. Scale bars (a) 1 µm, (b) 400 nm, (c) 100 nm, (e) 400 nm, (f) 50 nm.

6.2 Monolayer growth

When using the e-beam source, we started to obtain some flakes with a full monolayer coverage in samples grown at temperatures above 1560 ºC with a large amount of amorphous carbon deposits. When the substrate temperature was increased to 1640 ºC all samples presented consistently flakes with a coverage of at least one monolayer. In this section all the images shown correspond to samples grown at such temperature. Nevertheless, as mentioned in the introduction of the chapter, the current applied to the source was increased as the target was used in order to obtain a constant carbon flux.

A series of AFM images describe the surfaces of different flakes on a sample grown with a fresh target at I_{source}= 200 mA (Fig 6.4). Three out of ten flakes present large (from ~19 nm to ~35 nm) period Moiré patterns. The rest of the flakes scanned in this sample display ~14 nm regular Moiré patterns. Figure 6.4a is a 10×10 μm^2 topographic image of a flake containing a typical overall relaxed ~14 nm Moiré pattern. Lines corresponding to the buckling of the hBN flake due to thermal cycling can be observed as well as a large density of amorphous carbon deposits. The blue arrow indicates the area where the 250×250 nm^2 image in Fig 6.4b was taken. A profile taken along the path marked in green indicates that the height of the domain walls of the Moiré are ~30 pm while the period along this direction is ~14nm. In Fig 6.4c (taken from the centre of Fig 6.4b) we can observe the Moiré in more detail.

Figure 6.4d shows a cracked graphene layer located in a different flake. The Moiré patterns at opposite sides of the crack, both with periods ~15 nm are slightly rotated with respect to each other (see arrows) as we saw previously on samples grow with a carbon filament source. A third flake in this sample presents a larger ~33 nm Moiré. Figures 6.4e-g for a series of zoom-in images with the same scales respectively to Figs 6.4a- c. Large Moiré patterns were found on another two fake5.s (Figs 6.4h and 6.4i).

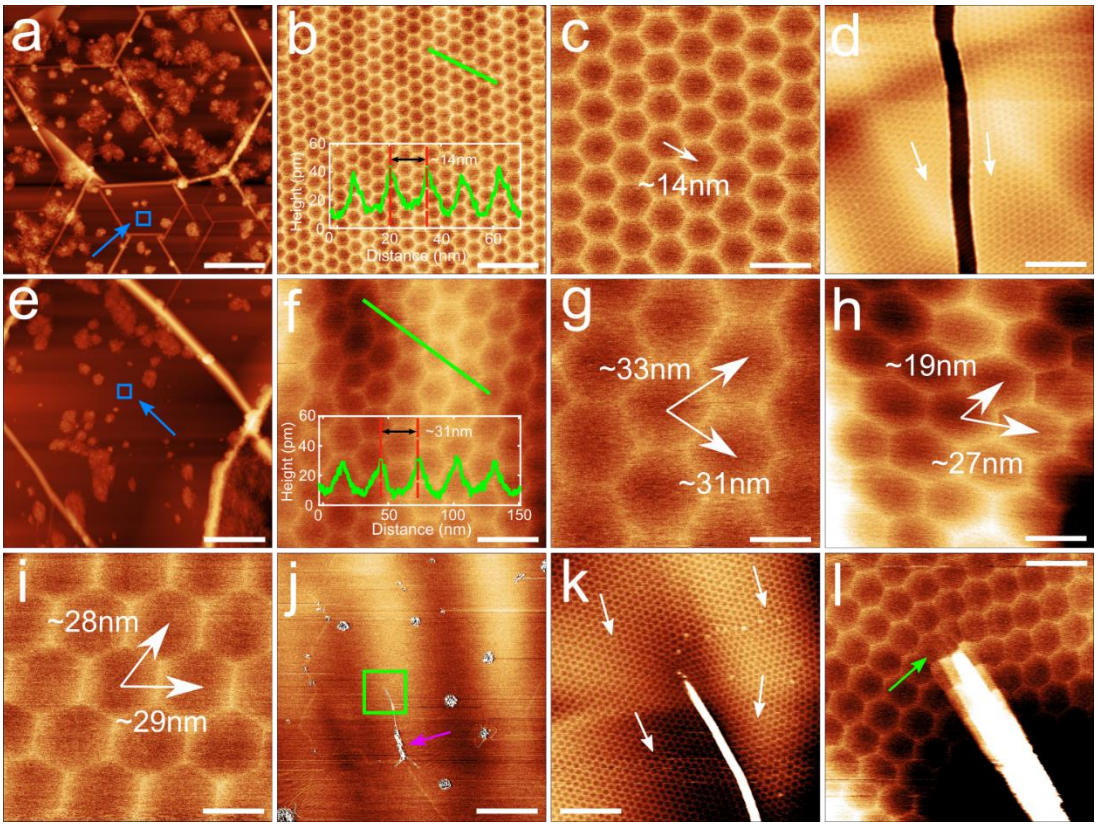

Figure 6.4: AFM images of hBN flakes on the same sample. a-c) Higher magnification sequence showing regular ~14 nm Moiré pattern. (b) was extracted from area indicated by blue box and arrow in (a). Profile in (b) indicates ~30 pm domain wall height. No defects are found in the area.(c) was extracted from central area in (b). d) Crack in a different flake. Moiré patterns are rotated at opposite sides from the crack. e-f) analogous to (a-c) with a ~30nm Moiré. h-i) Topographic images of other overall strained graphene layers. Images have the same scale as (c) and (g). j-k) Sequence showing a narrow carbon deposit with a spike. Phase channel image in (j) shows the whole deposit (magenta arrow) and the surroundings. Green box indicates location of (k), where the misalignment of the Moiré patterns at opposite sides of the deposit can be appreciated (white arrows). The Moiré on the right-hand side rotates abruptly along a frontier (up-right quadrant) leaving a series of topological defects. Deposits similar to this were observed in samples grow with an atomic source. Topological defect (green arrow) lies at the top of the spike in (l). Scale bars: (a) 2 µm, (b) 50 nm, (c) 20 nm, (d) 100 nm, (e) 2 µm, (f) 50 nm, (g) 20 nm, (h) 50 nm, (i) 50 nm, (j) 1µm, (k) 100 nm, (l) 20 nm.

An elongated carbon deposit with abrupt ends similar to those described in Fig 4.13 was also observed in this sample (magenta arrow in Fig 6.4j). Three ends or spikes emerge from the deposit. One at the top and two at the bottom. The former can be observed closely in Figure 6.4k, taken from the area in the green square. The slight rotation of the Moiré pattern at opposite sides of the spike is also present. The orientations of the Moiré patterns are highlighted with white arrows. Green arrow in Fig 6.4l points at a defect found right at the tip of the spike.

In the same sample, one of the flakes with ~14 nm Moiré patterns presents a series of topological defects that run along a meandering frontier. A blue arrow in the 10×10 μm^2 image in Fig 6.5b points at the location of such frontier. Figure 6.5b was elaborated from superimposed phase channel images. The frontier can be appreciated in brighter contrast running approximately horizontally. It connects several deposits laying close to the left-hand side area and keeps running away from them. Above this frontier the Moiré pattern has a constant orientation (black arrow points along one of the Moiré axis) but below it, it gradually shifts orientational angle (white arrows). Boxes indicate location of scans on Fig 6.5c (turquoise) and 6.5d (magenta).

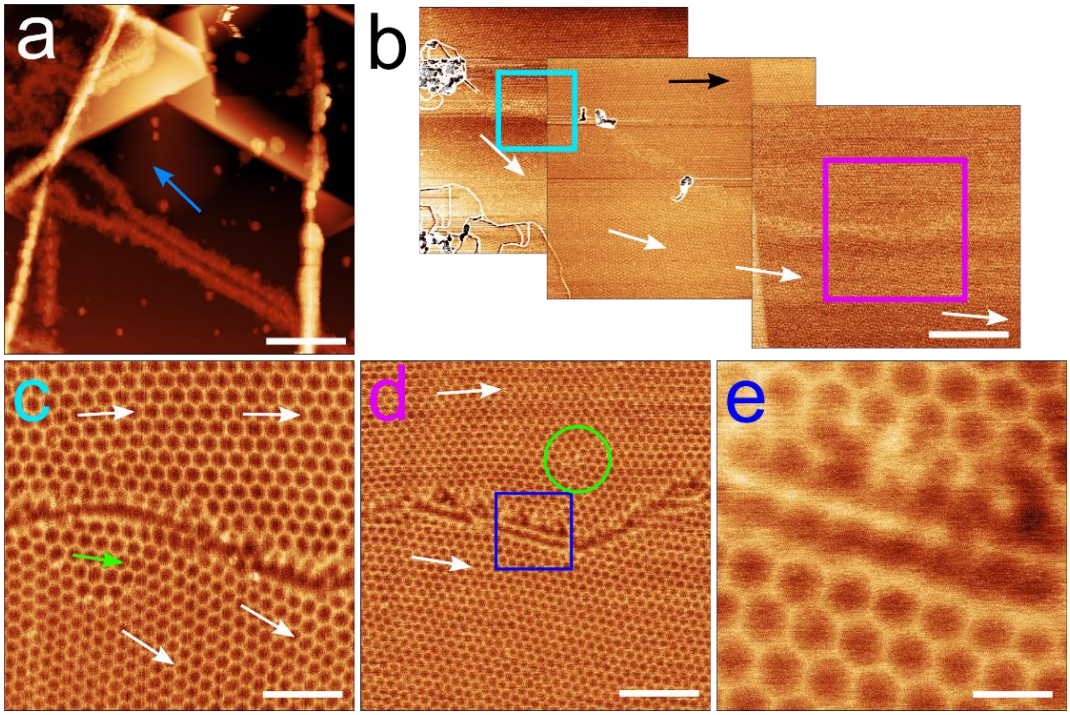

Figure 6.5: AFM images (all topographic except composition in (b)) on an area where a series of defects are arranged forming a structure similar to a frontier. a) Large size scan of the flake. Blue arrow indicates area where the images composed in (b) were extracted. b) The structure connects three carbon deposits and runs along a few micron-meters path. Arrows indicate orientation of the Moiré in the superior and inferior domains. In the inferior domain, the Moiré gradually shifts direction. Higher magnification areas are indicated by coloured boxes and figure indexes. Scale bars: (a) 2 µm, (b) 200 nm, (c) 50 nm, (d) 100 nm, (e) 20 nm.

In Fig 6.5c the frontier can be appreciated as a lower contrast line that oscillates around the middle of the image. A large number of topological defects lie on the area with small carbon deposits attached. On the area above the frontier, the orientation of the Moiré is considerably uniform, although there are two deposits that adsorb Moiré rows coming from the right (located on the top-left quadrant). In contrast, the Moiré below the frontier shifts orientation abruptly (compare green and white arrows), generating a larger number of defects in the area. On Fig 6.5d another section of the frontier divides

the two domains. In this area, the two Moiré patterns are almost aligned since the Moiré at the bottom has shifted orientation. A topological defect marked with a green circle allows the Moiré in the top domain to align even further with the bottom domain. Figure 6.5e taken from the area indicated with a blue square shows the frontier in more detail. In this area, the frontier is formed by two parallel strained regions with a domain wall that divides them.

The sample grown next, at a I_{source}= 250 mA presents features previously observed on samples grown using the two other carbon sources. Figure 6.6a is a large scan of a flake where two rotated Moiré patterns coalesce forming a series of punctual defects. A blue arrow points at the precise area, which is shown in Fig 6.6b. The topological defects (inside blue circles) are arranged almost periodically on a line. Figure 6.5c (extracted from the area in the green square) shows the area in higher detail. The patterns at opposite sides of the line are ~30º rotated with respect to each other. The green arrow in Fig 6.5d (image extracted from the centre of Fig 6.5c) points at a Moiré cell with 7 neighbours. Other cells with only 5 neighbours are in the area (purple arrows). Another flake in the same sample displays multiple layers emerging from carbon deposits formed on step edges. Figures 6.6e-g are a zoom-in sequence analogous to the previous. The Moiré pattern is slightly curved in the area above the horizontal line of deposits (in phase channel the deposit appears in darker contrast).

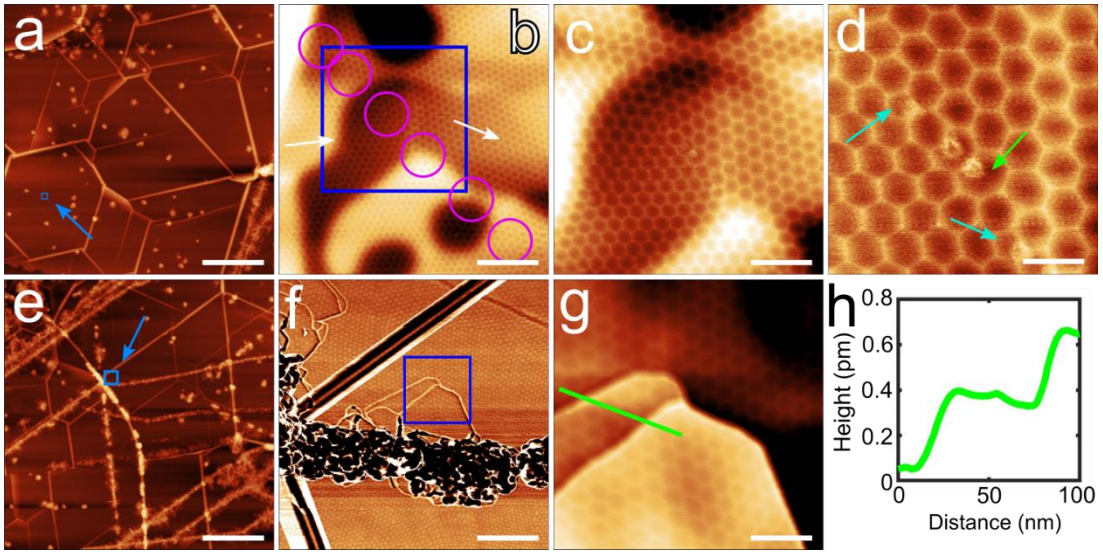

Figure 6.6: AFM images of flakes that present coalesced rotated graphene layers (a-d) and additional layers emerging from step edge carbon deposits (e-g). Blue arrows and blue boxes indicate scan areas of the subsequent images. Scale bars: (a) 2 µm, (b) 100 nm, (c) 50 nm, (d) 20 nm, (e) 2µm, (f) 200 nm, (g) 50 nm.

The additional layers are shown in the topographic channel in Fig 6.6g. The Moiré pattern observed on their surface has the same ~14 nm period and is roughly aligned (considering the slight curve in the area) with the pattern in the first layer. Profile in Fig 6.6h indicates the height of a second and third layers. The heights of the domain walls (relief of the Moiré pattern) in the first second and third layers are the same.

For the sample described in Fig 6.7 (being the fourth in the cycle) I_{source}= 350mV. Several flakes present additional layers that emerge from carbon deposits on step edges. Also, large (~300 nm across) islands lie away from the deposits (Fig 6.7a-d). Figure 6.7b corresponding to phase channel was taken from the area marked with a blue arrow in Fig 6.7a. Figure 6.7c, taken from a scan in the area shows one of the islands in detail. The island has an overall round shape although the bottom and left sides seem to be slightly faceted along the zig-zag direction. The height of the island corresponds to a monolayer and the Moiré on top of it is roughly aligned with the first layer Moiré. The island also presents a few small holes and a dent in the edge, which are features not observed before.

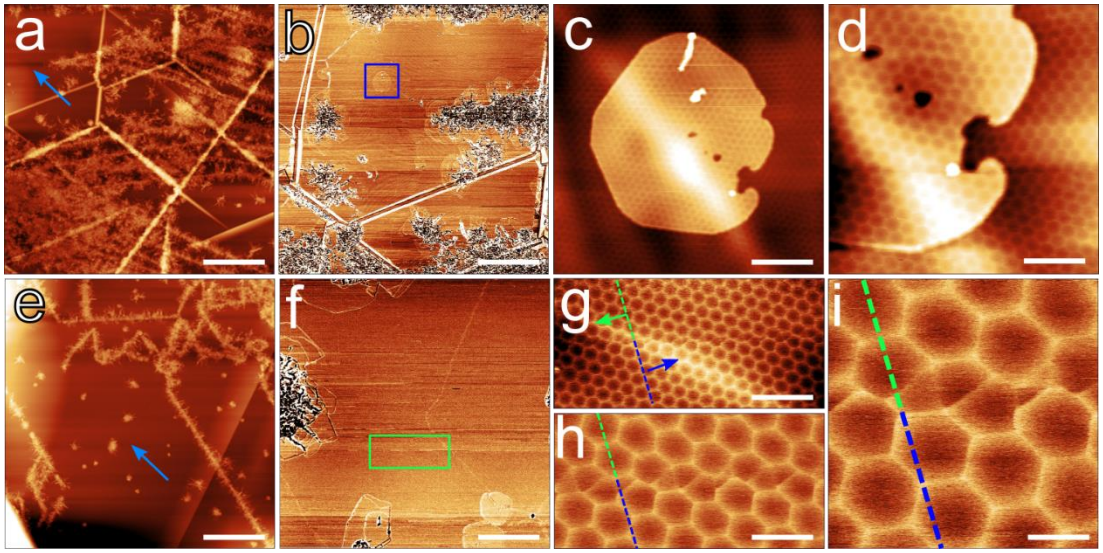

Figure 6.7: a-d) Higher magnification AFM images sequence showing a considerably large ~300nm across additional layer with slightly faceted edges, small holes and dents. The surface is almost free of carbon deposits. e-i) Another zoom-in sequence that shows another structure similar to a frontier. In this case the Moiré pattern at opposite sides is aligned but slightly displaced in perpendicular to the frontier. Note the line in green and blue in (g-i). The line goes through the centre of the Moiré cells in the domain above the frontier while touches the corners of the hexagons in the domain below the frontier. In (h) and (i) the Moiré cells at the frontier are shown with deformed, non-hexagonal shapes. Scale bars: (a) 2 µm, (b) 1 µm, (c) 100 nm, (d) 50 nm, (e) 2 µm, (f) 400 nm, (g) 100 nm, (h) 50 nm, (i) 10 nm.

Another flake in the same sample also presents an area where two Moiré patterns coalesce in a very particular way (Figs 6.7e-i). The patterns have the same period and are aligned but appear to be slightly shifted in perpendicular to their frontier. Green and blue dashed line in Fig 6.7g and h makes this shift more obvious. As a result the Moiré cells on the frontier have lost their hexagonal shape. Most of them form triangles but there are also other shapes.

The next sample of the cycle (I_{source}= 400 mA) presents flakes with many more graphene additional layers. Figure 6.8a shows in the topographic channel the surface of a flake with a central area considerably free of amorphous carbon deposits. In Fig 6.8b an amplitude channel image extracted from such area shows the edges of the additional layers very clearly. They display round edges in some cases while faceted along the zig-zag direction in others. Fig 6.8c was taken from the area marked with the

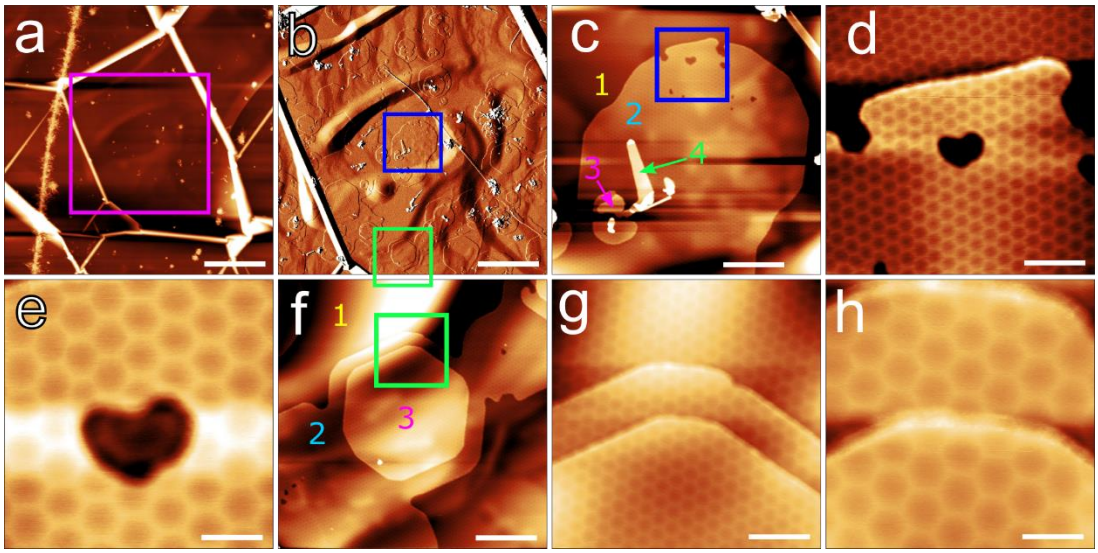

Figure 6.8: AFM images of larger area additional graphene layers (~500nm) covering most of the surface of a first layer (phase channel in (b)). Some islands have a round shape (c) or faceted edges (f). The Moiré pattern with the same morphology can be distinguished on top of these additional layers (d-e and g-h) and being commensurate with the first layer. Holes and dents in these layers are also present. Scale bars: (a) 2 µm, (b) 1 µm, (c) 200 nm, (d) 50 nm, (e) 20 nm, (f) 200 nm, (g) 50 nm, (h) 20 nm.

blue box. The image shows in higher magnification one of the bi-layers with round edges. On top of it there are a third and a fourth layer (indicated with arrows). A hole in the second layer and a dent can be seen in detail in Fig 6.8d. The topography of the Moiré pattern of the first layer is perceived through the hole (Fig 6.8e). Figure 6.8f taken from the area in the green square in Fig 6.8b shows one of the faceted islands. Again, numbers mark the order of the layers. Figures 6.8g and h show that the Moiré patterns are coherent up to at least the third layer.

Other flakes in the same sample present similar additional layers. Figure 6.9 displays a few of them (one on each row). Images in same column are of the same scale. Large area scan images in the first column correspond to amplitude channel, second column (taken from the areas marked with a green square) are phase and third topographic. First and second layers are indicated with numbers on the images in the second column.

Images in the first row zoom into an area where, given the shape of the borders we can infer that two second layers coalesce. Interestingly, there is no trace of defects in the area and the Moiré pattern keeps the same morphology as in the rest of the layer.

The second row of images zooms into a region on a flake with a large number of carbon deposits. Three second layers growing from the right, left and bottom of the image have left a fin shaped gap. A slight Moiré rotation is indicated by white arrows.

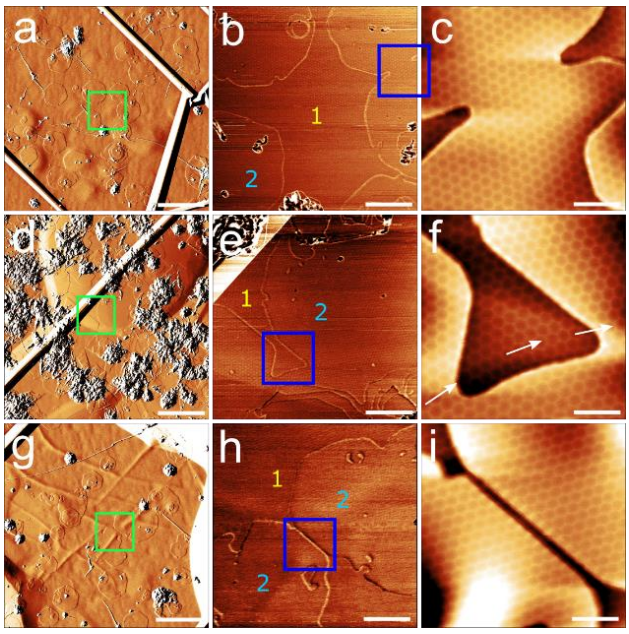

Figure 6.9: AFM images of flakes that present additional graphene layers. Each row forms a higher magnification sequence showing features involving secondary layers. Images on columns from left to right correspond respectively to the amplitude, phase and topographic channel. First row shows two coalesced secondary layers, second row a narrow gap between three secondary layers approaching from different directions and third row a narrow and elongated straight gap between layers. Scale bars: (a, d and g) 1 µm, (b, e and h) 100 nm, (c, f and i) 50 nm.

The third row zooms into a narrow gap formed by two secondary islands. The line of the gap is considerably straight and approximately perpendicular to the direction that separates the centres of the islands. The Moiré patterns on these bi-layers are aligned and have the same ~ 14 nm period as the first layer.

The additional layers on all the images are very clean and the Moiré pattern can be distinguished in their surface with the same morphology and relieve as the Moiré pattern in the first layer. Perhaps the growth of large surface few layer graphene on hBN can be controlled using an e-beam source.

A sample grown in another cycle, presents the Moiré patterns with the largest period ~46 nm. Sample was grown at I_{source} = 300 mV. The area was located on a flake with a high density of carbon deposits on step edges. Blue squares indicate the zoom-in areas in images from Fig 6.10a to Fig 6.10e. The Moiré pattern is highly distorted and presents several defects. Figure 6.10f taken from the area in the magenta square in Fig 6.10b shows Moiré cells with enlarged long domain walls (white arrows).

Green box in Fig 6.10a indicates the scan area of the amplitude channel image in Fig 6.10g. Additional layers emerge from carbon deposits in the area. A zoom-in image of the edge of the secondary layer in the centre of the image (Fig 6.10h) reveals domain

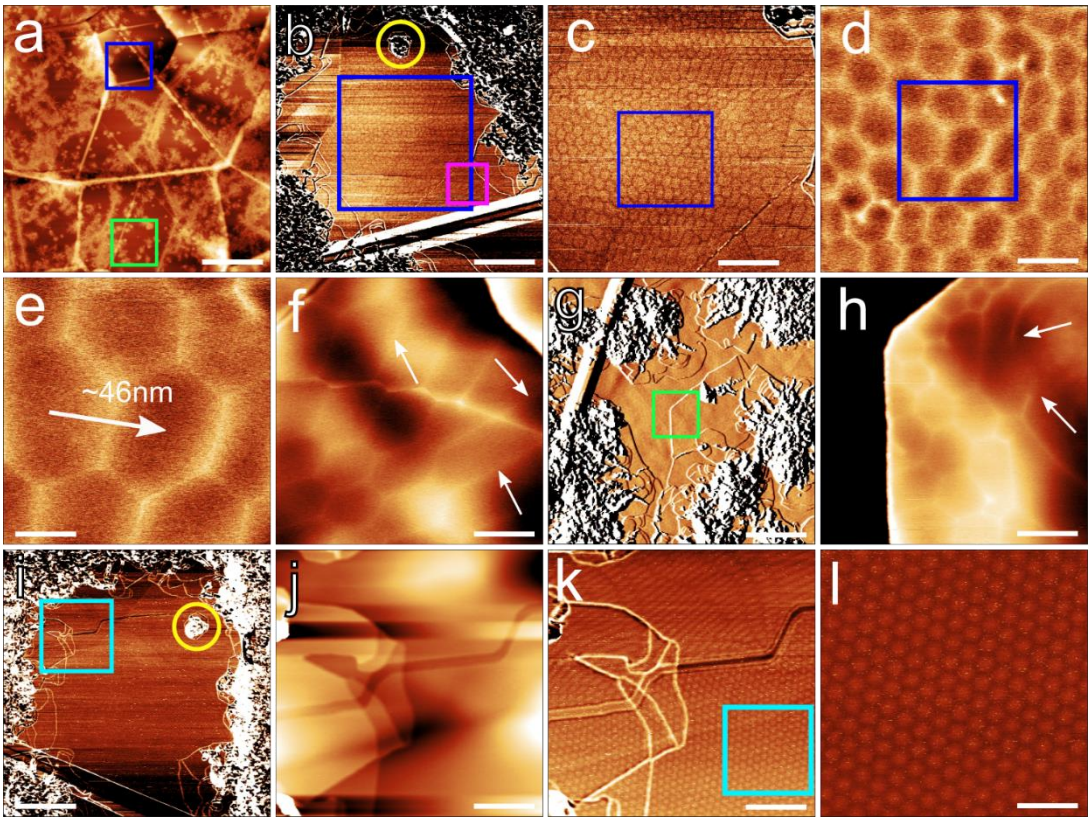

Figure 6.10: AFM images of a flake that presents the Moiré with the largest period (~46 nm) found on samples using an e-beam source. Images correspond to the topographic channel except (b), (c),(i), (k) and (l) and (g) which is an amplitude channel image. From (a) to (e) images show the location and aspect of the ~46 nm Moiré. f) Moiré in the bottom-right corner of image (b), indicated by a magenta square, presents elongated cells (white arrow) possibly due to a non-uniform strain distribution close to carbon deposits. g) Amplitude channel image extracted from area in green box in (a). A large second layer emerges from a carbon deposit in the centre of the image. h) domain walls that terminate abruptly as seen on lattice matched areas are found (white arrows). From (i) to (l) the region that previously displayed a ~46 nm Moiré (notice the deposit indicated by two yellow circles in (b) and (i)) has cracked and relaxed. Topographic image in (j) shows the crack running below additional layers (left). In (k) which corresponds to a scan of the same area in phase channel the Moiré patterns above (distorted) and below (regular ~14 nm) can be appreciated. Magenta square indicates scan area in (l) showing the regular ~14 nm Moiré. Scale bars: (a) 3 µm, (b) 400 nm, (c) 200 nm, (d)50 nm, (e)20 nm, (f) 50 nm, (g) 400 nm, (h) 50 nm, (i) 400 nm, (j) 100 nm, (k) 100 nm (l) 40 nm.

walls that terminate abruptly as the walls observed in samples with lattice matched graphene. Figures 6.10i corresponds to a scan of the same area in Fig 6.10b a few days after the ~46 nm Moiré images were obtained. The two images are slightly rotated with respect to each other. Notice the carbon deposit highlighted by a yellow circle in both figures. The layer now presents a crack, close to the deposit on the top. Figure 6.10j, extracted from the area in the turquois square in Fig 6.10i shows the crack in more detail running below additional layers that emerge from a deposit. Fig 6.10k corresponding to the phase channel allows to see the Moiré pattern above and below the crack. Above the pattern is significantly distorted. Below, the pattern has a regular ~14nm period. Turquois square indicates area of the phase channel image in Fig 6.10l. The Moiré pattern on the additional layers emerging from carbon deposits is also different at opposite side of the crack.

E-beam grown graphene layers that present domain walls with abrupt ends were found in various hBN flakes. The sample was grown (as the previous samples) at 1640ºC (read from the thermocouple behind the substrate holder). However, in this case a single polished side sapphire wafer was used in order to increase the substrate temperature. Also, the sample was grown with a fresh target with $I_{source} = 200$ mA.

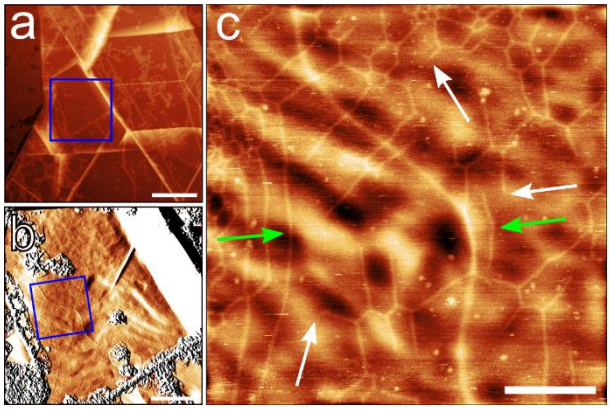

Figure 6.11: AFM images of a flake covered in graphene layers that display broken domain walls, a feature found in lattice matched graphene layers. Blue boxes indicate scan area of the next image. a) Large topographic image of flake. b) Amplitude channel shows carbon deposits surround the area in (c). c) Domain walls run in three main directions. Some of them are broken (white arrows) or curved (green arrows). Scale bars: (a) 4 µm, (b) 1 µm, (c) 300 nm.

Blue squares in Figs 6.11a-b indicate location of the area shown Fig 6.11c where the domain walls are observed. The thicker curve running from top to bottom of the image corresponds to a hBN fold. Domain walls run in the three principal crystal directions are broken (white arrows), leaving small ~200 nm lattice matched graphene areas. Curved domain walls (green arrows) not oriented in any of these directions are also present.

6.3 Summary

In this chapter we explored the growth of graphene on hBN by high substrate temperature MBE equipped with an e-beam source.

Islands have a similar morphology to the islands grown using filament source with round edges and carbon deposits clustered close to the centres of the islands.

As with the previous sources increased substrate temperature allows complete coverage in graphene of the hBN flakes.

A series of features previously observed in samples grown with the carbon filament are present. For example, coalesced rotated Moiré patterns, Moiré patterns with periods much larger than 14 nm, narrow carbon deposits that terminate at defects or cracked and relaxed layers that yield domains with different Moiré patterns.

We also observe significant differences between graphene grown with this source and the previous sources. For example, the large number and large surface area (~500 nm across) of additional layers. The Moiré patterns can be appreciated on them with the same period and orientation as the first layer, indicating that they are strained in the same manner. We have also observed coalesced graphene domains were the frontiers present morphologies different to those on layers grown with the filament source.

7. The adsorption of hexacontane on hexagonal boron nitride

The aim of this chapter is to investigate the adsorption of a long chain alkane, hexacontane ($C_{60}H_{122}$), on hBN using AFM. The adsorption of alkanes has been studied in depth, particularly on metals[117–119] and graphite[94–101,120], but on hBN has so far been studied only using diffraction techniques[121,122], with no direct determination of their real-space arrangement and potential to control supramolecular organization.

The alkane can be deposited either by sublimation or from solution. We find, using atomic force microscopy (AFM), that the alkanes lie flat on the surface with the molecular axis parallel the zig-zag direction of hBN, forming lamellar rows, similar to those formed by long-chain alkanes deposited on graphite. The molecules form rotational domains with sizes in the order of microns (in the case of deposition by sublimation) hundreds of manometers (in the case of deposition in solution). Upon deposition of more than one layer of hexacontane, additional layers are formed which propagate the row geometry, but are more disordered and weakly bound to the substrate and are thus more susceptible to heat- and tip-induced modifications.

7.1 Monolayer growth

An AFM image of the surface of an hBN flake acquired after the deposition, by sublimation, of 1 monolayer (ML) of hexacontane is shown in Fig 7.1a. We observe a series of rows running across the surface, and a height profile (inset) along a line perpendicular to them shows that their amplitude is ~20 pm and their separation (determined from a Fourier transform) is 7.9 ± 0.2 nm. Additional irregular contrast variations are observed due to the roughness of the underlying SiO_2 substrate on which the hBN flake is mounted. These background fluctuations have a peak-to-peak height variation of 50 pm, and a characteristic length scale of ~100 nm, and are not associated with the molecules.

The lines are very similar to those observed when alkanes adsorb on graphite and form lamellar rows in which the linear molecules are stacked perpendicular to the row axis. A higher magnification AFM image on Fig 2b, shows that the rows on hBN correspond to similar lamellae, in which the individual molecules can be resolved and, as expected, are perpendicular to the row direction. The distance between molecules in the same row is 0.44 ± 0.02 nm, very close to the value reported for alkanes on graphite. The inset shows a profile taken across 20 molecules as indicated by the path in blue. We typically observe domains with area 1 – 5 μm^2 in one of three orientations with an angular separation of 120°.

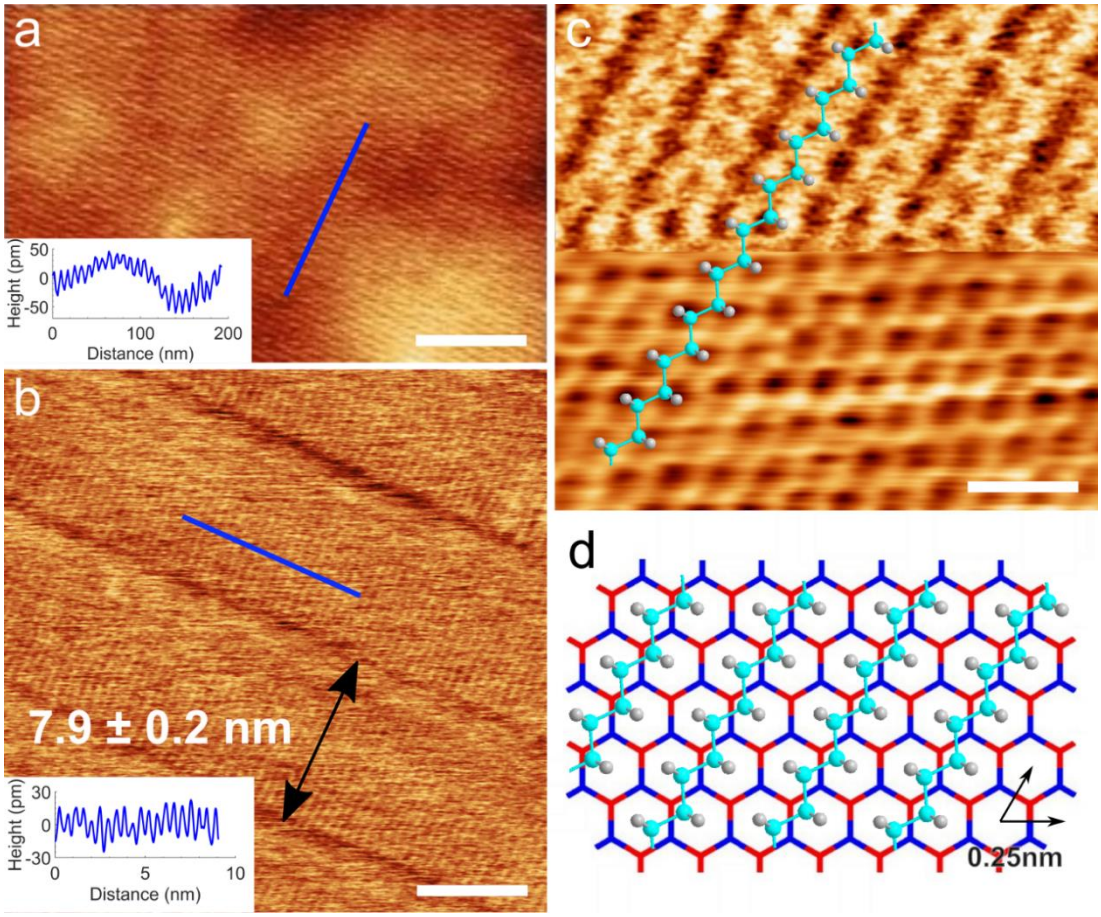

Figure 7.1: Topography AFM images of 1ML of hexacontane sublimed onto hBN. a) Large area image of hexacontane lamellar rows; inset - height profile along the trajectory marked in the image. b) High resolution topographic image showing the molecular arrangement within the lamellae; inset - height profile along the trajectory marked in image. c) High resolution AFM images showing individual hexacontane molecules on the hBN lattice (top half) and the bare hBN lattice on the same area after molecules were removed (bottom half). The top half corresponds to an image showing the molecules laying on the surface while the bottom one corresponds to an image of the same hBN surface once the molecules have been removed. d) Schematic showing the registry of hexacontane with respect to the hBN lattice. The arrows represent the lattice vectors. Scale bars: (a) 100 nm, (b) 5 nm, (c) 1 nm.

To determine the orientation of the molecules with respect to the underlying hBN substrate, we employed a protocol that was previously used in the study of supramolecular networks on black phosphorus[123]. By increasing the setpoint used in AFM imaging, it is possible to partially remove the alkane chains, allowing the local imaging of the underlying substrate. Figure 7.1c shows an overlay of two topographic images in which the top segment corresponds to the upper half of an image acquired at a low setpoint whereas the bottom segment is the lower half of an image of the same area acquired at a higher setpoint. The hBN surface shown in Figure 7.1c has a coverage of 1 ML, and the molecular chains can be identified in the upper half of the composite running from bottom-left to top-right. The bottom half of Fig 7.1c shows the exposed hBN lattice, which allows the identification of the orientation of the lattice vectors. A comparison between the images shows that the molecules run parallel to the lattice vector (the zigzag direction) of hBN, as shown schematically in the structural diagram in Fig 7.1d.

7.2 Multiple layer growth

Figure 7.2 shows images of hBN on which layers of hexacontane with different thicknesses have been sublimed. The layer thickness was determined using a quartz crystal thickness monitor, which was calibrated from the surface coverage of the dendritic structures formed by hexacontane on the SiO_2 surface[124]. For sub-monolayer coverages (Figs 6.2a-c) isolated islands are formed with typical lateral sizes of ~1 μm and a height which is comparable to the roughness of the hBN flake. The island at the centre of Fig 7.2a is shown at higher magnification (area highlighted in Fig 7.2a) in Fig 7.2b and from the accompanying height profile (along the red line) we determine a height of 0.4 ± 0.1 nm consistent with a partial monolayer of flat-lying molecules.

The direction of the lamellar rows is identified by the arrow; the rows run in a common direction for a given island indicating a single extended domain of molecular ordering. An even higher magnification image (area highlighted in Fig 7.2b) is shown in Fig 7.2c where the lamellar rows are resolved. The isolated hexacontane islands are rather unstable and after acquiring several images, their shape can be modified, or they can be removed completely; this tip-molecule interaction also accounts for the distortion

in the lamellar rows which is prevalent during small scale scans, especially at sub-monolayer coverages.

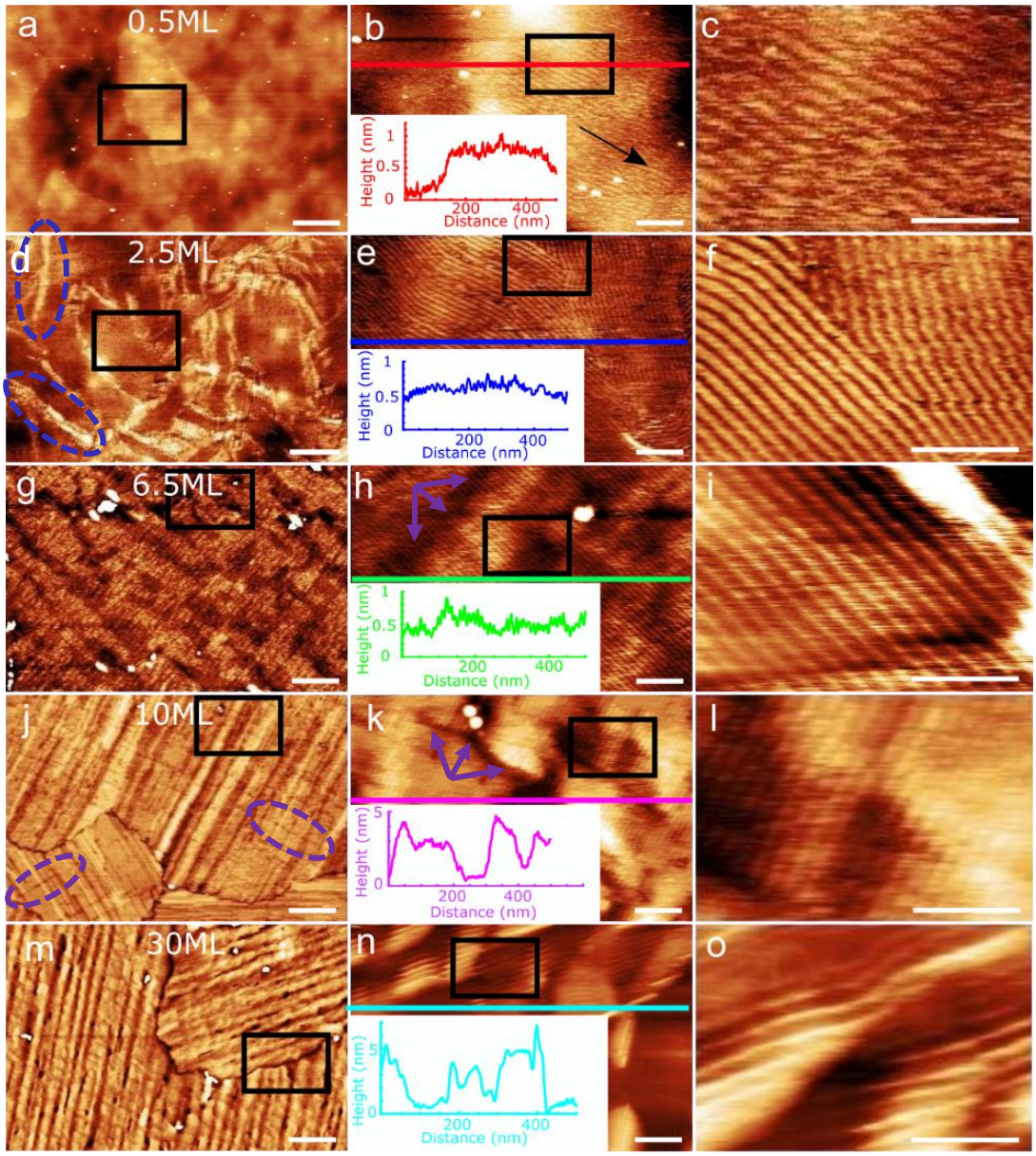

Figure 7.2: AFM images for different thicknesses of hexacontane. (a, b and c) 0.5ML; (d, e and f) 2.5ML; (g, h and i) 6.5ML; (j, k and l) 10ML; (m, n and o) 30ML. The boxes highlighted in black on the images in the left and centre columns show the areas where the zoomed images in respectively, the centre and right columns were acquired. In the centre column, profiles running along the paths indicated in different colours are overlaid on each image. The right column shows images in which the lamellar rows can be resolved for each thickness. Scale bars: Left column: 400 nm; middle column: 100 nm; Right column: 50 nm.

At a coverage of 2.5ML topographically flat regions co-exist with elongated features with higher apparent brightness (Figs 7.2d-f) see features highlighted by dashed blue ellipses in Fig 7.2d. These features are unstable under scanning and it is difficult to acquire higher resolution images to reveal additional details of their structure.

However, higher resolution images of the topographically flat areas can be acquired which reveal the lamellar rows on the surface; from the coverage we infer a thickness of 2-3ML in these regions. A comparison of such images with larger area images indicates that the topographically bright regions in, for example, Fig 7.2d, form at, or close to, the boundaries between neighbouring domains with different orientation. Higher resolution images (see Fig 7.2f) show that the lamellar rows can deviate from the preferred alignment and show discontinuities and even terminate abruptly in these boundary regions.

As the coverage is further increased to 6.5ML (Figs 7.2g-i) an additional superstructure appears in the form of topographically bright features which run perpendicular to the lamellar rows (in this set of figures the orientation of the lamellar rows is determined from the high resolution image in Fig 7.2i, which is a zoom of the highlighted region in Fig 7.2h).

Between these bright regions we observe ‘trenches’ which are topographically dark and also run approximately perpendicular to the lamellar rows (marked by purple arrows in Fig 7.2h). This implies that the lamellar rows terminate at positions which are spatially correlated. We speculate that this may be due to strain relief in the growing film.

The lamellar rows and trenches propagate through the growing layer. After the deposition of 10ML these features may still be resolved although the height profile shows that the surface becomes significantly roughened (ellipses in Fig 7.2j and arrows in k mark the position of trenches). We do not see further significant changes for thicker layers (Figs 7.2m-o show images acquired after the deposition of 30ML). Interestingly, the period of the lamellae is preserved for all coverages studied implying that the substrate directs growth even for these very thick layers.

7.3 Theoretical calculations

The energetics of alkane adsorption on hBN were investigated by Matteo Baldoni[1] using molecular mechanics employing LAMMPS simulation package. The hBN substrate was treated as a rigid monolayer with atoms fixed at their crystallographic positions. In particular, the dependence of the adsorption energy of a single alkane chain on the relative orientation of the molecular axis and the hBN lattice was calculated. First a single hexacontane molecule was optimized in vacuum; the calculated C-C-C spacing along the chain is 0.255 nm, close to the value taken for the lattice constant of hBN, 0.250 nm. The optimised hexacontane molecule was then placed at a height 0.35 nm above the model hBN surface, with the plane of the carbon atoms parallel to the substrate. The molecule is then moved as a rigid body along the *x* and *y* axes (defined in Fig 7.3a) in steps of 0.01 nm as in previous work[125]. At each step, the adsorption energy was calculated as $E(C_{60}H_{122}@hBN) - E(C_{60}H_{122}) - E(hBN)$.

The calculations show that, in agreement with experiment, the lowest energy corresponds to orientations where a hexacontane molecule is aligned with the hBN zigzag direction (as shown in Fig 7.3a); the adsorption energy in this configuration is favoured by approximately 0.09 eV/molecule (Fig 7.3b). The energies in Fig 7.3b are extracted as the minimum energies extracted from the PES profiles for each angle of rotation. Examples of the PES profile for alignment angles of 0º and 20º are shown in Figs 7.3c-d. After full relaxation of hexacontane molecules on hBN , the adsorption energy at 0º is -5.93 eV (the actual structure is shown in Fig 7.3a). The results have also been confirmed for multiple (eight) alkane chains adsorbed on the hBN surface. After the minimisation of the total energy all eight molecules are positioned in the same preferential adsorption sites as in the case of a single chain giving an intermolecular distance of 0.435 nm corresponding to a commensurate arrangement on the hBN layer. The interaction energy between the chains have been estimated as

[1] Istituto per lo Studio dei Materiali Nanostrutturati (ISMN), Consiglio Nazionale delle Ricerche (CNR), Via P. Gobetti 101, Bologna 40129, Italy

0.13 eV per each pair. The spacing and orientation of the alkanes are in excellent agreement with our experimental observations

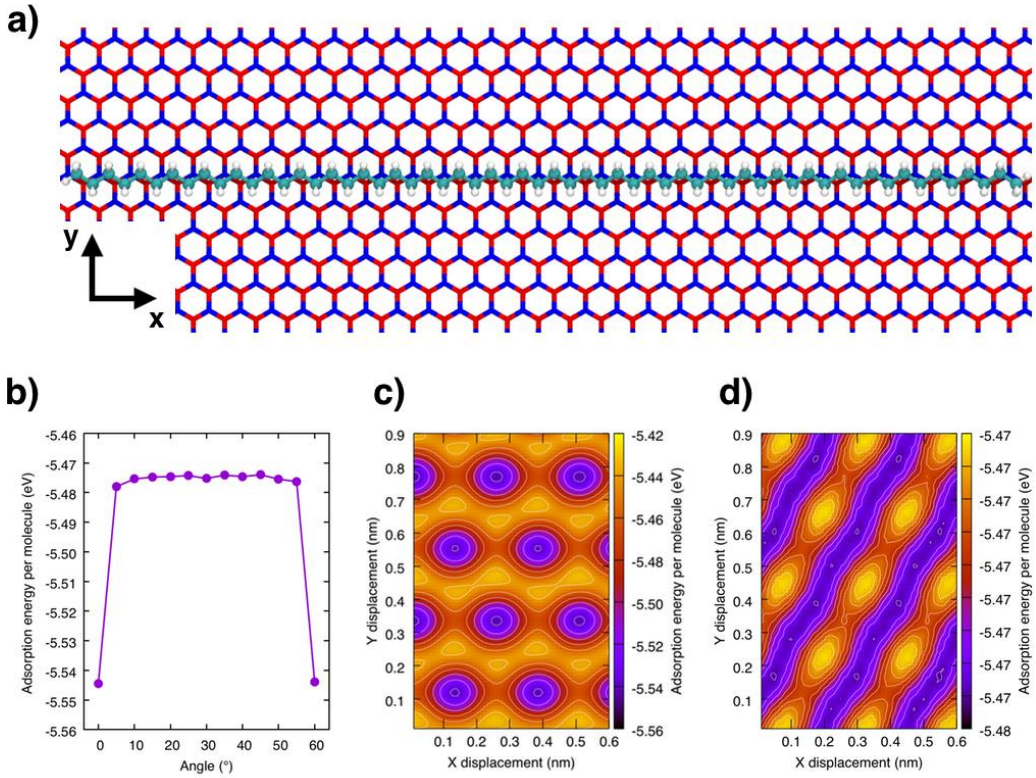

Figure 7.3: a) Optimised structure of a hexacontane molecule on hBN surface. b) Adsorption energy as a function of the angle between the principal axis of the hexacontane molecule and the zigzag direction of the hBN lattice. c) Potential energy surface at 0º rotation and (d) 20º.

7.4 Effect of heat applied on the sample

We have also investigated the effect of post-deposition annealing on the sample morphology. Figure 7.4a shows an area on a sample with a coverage of 6.5ML. The high contrast region in the centre of the image is due to a ~4nm thick hBN terrace and its structure is independent from the hexacontane deposition. Several different orientational domains are observed and the boundaries and local orientation of rows are indicated by the turquoise lines and arrows respectively.

Figure 7.4b shows the same area after the sample was annealed on a hot plate at 80 °C for 5 minutes (under ambient conditions). A series of facetted rectangular islands with heights in the range 6-8 nm are formed which are aligned with the orientation of rows prior to annealing. The lamellar rows are still present in the regions of the surface

between the islands. The formation of islands is attributed to the agglomeration of hexacontane molecules which are depleted from neighbouring multilayer areas in a ripening-type process which leaves a residual monolayer adsorbed on the hBN surface.

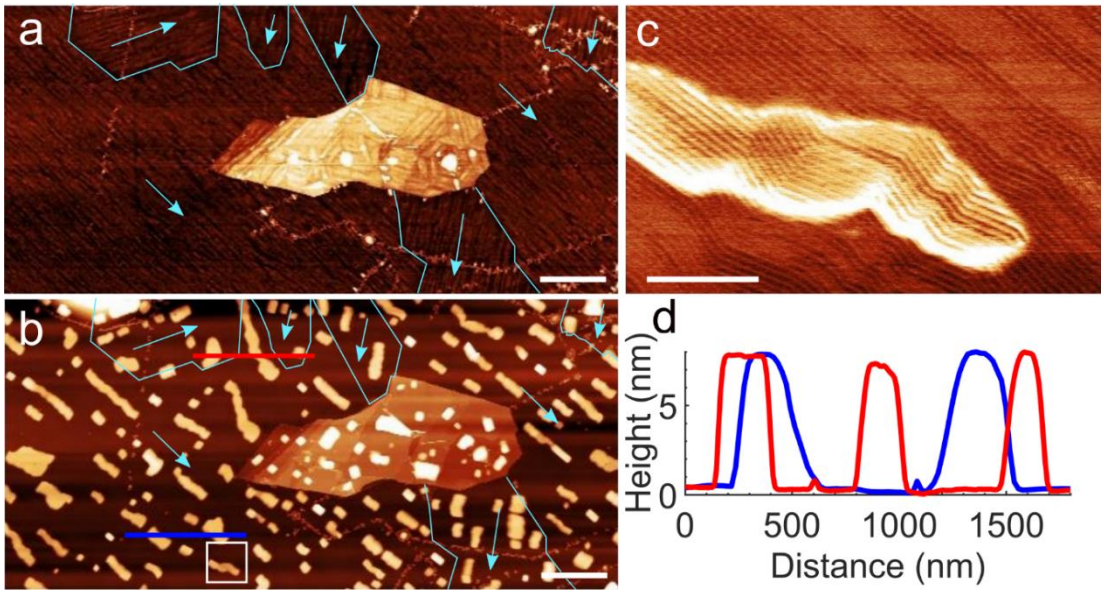

Figure 7.4: a and b) AFM topography images allow a comparison of an hBN area covered in hexacontane before (a) and after (b) heat is applied to the sample. Domain frontiers are indicated in turquois. c) AFM phase image showing closely one of the islands formed after heat was applied. The lamellar rows can be resolved on top of the island with the same orientation as in the background space. d) Profiles running across various islands with paths shown in (b). Scale bars: (a and b) 1 µm, (c) 100 nm.

Figure 7.4c shows an AFM phase image of an island (area marked with a white square on Fig 7.4b). The lamellar rows are present both on the monolayer-terminated regions between islands and also on the top surface of the islands. Although there is some disorder present, for example in the fluctuating orientation of the rows, the long axis of the island is approximately parallel to the row direction. Interestingly these images suggest that in these hexacontane crystallites the molecules lie parallel to the substrate and the macroscale arrangement consists of stacks of parallel lamellar rows. Furthermore, the orientation of the interfacial hexacontane molecules directly adsorbed on the hBN appears to propagate through the crystallite, to a first approximation, implying an epitaxial relationship.

7.5 Deposition from solution

AFM images of 1ML hexacontane domains grown in solution were also obtained. A sample was immersed in a 10 µg hexacontane/mL toluene solution for one minute then dried in a nitrogen stream. The molecules form three rotational domains of lamellar structures with an almost identical period 8.0 ± 0.2 nm, misaligned by 120º, as shown in Figure 7.5. The morphology of these films is very similar to the sublimed films but the size of the domains in this case is much smaller, of order 100 nm. The smaller size of these domains compared to the samples grown through sublimation is probably a consequence of the faster growth with a higher density of nucleation points compared to the growth by sublimation.

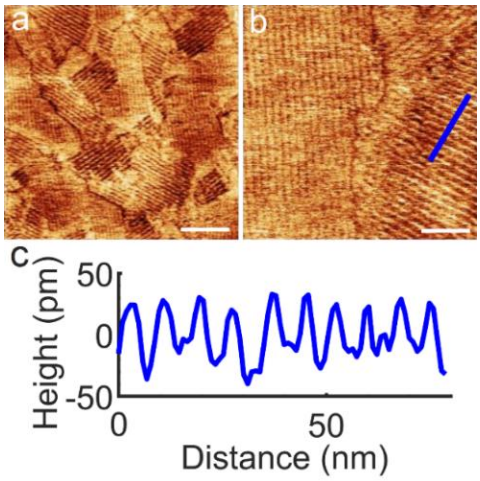

Figure 7.5: AFM images of hexacontane deposited on hBN from solution. a) Rotational domains of ~100nm cover the area. b) Higher magnification area shows three domains misaligned by 120º. c) Height profile along trajectory marked in (b). Scale bars: (a) 200 nm, (b) 100 nm.

7.6 AFM tip induced re-crystallization

Hexacontane molecules can also re-crystalize during AFM scan. Figure 7.6 shows images of a sample with >30ML hexacontane growth. The black arrows in Fig 7.6a indicate the orientation of the lamellar rows in each rotational domain. In the area indicated with a red square, a series of scans were taken. Topographic images in Fig 7.6b and Fig 7.6c show respectively the area before and after 25 scans. The molecules have piled up forming a series of hills with a higher aspect ratio in the direction of the lamellae. This also forms trenches on the spaces between hills, where the molecules have been depleted. Same image in phase channel in Fig 7.6d allows to see the lamellar rows more clearly, running in the same direction as before the series of scans were performed. Figures 7.6e-f show the previously scanned area in context with the surroundings. Profiles on Fig 7.6g (paths are indicated in Fig 7.6f) allow a comparison between the height of these hills and the roughness of the surface outside the scanned area, being the former approximately 5 times larger.

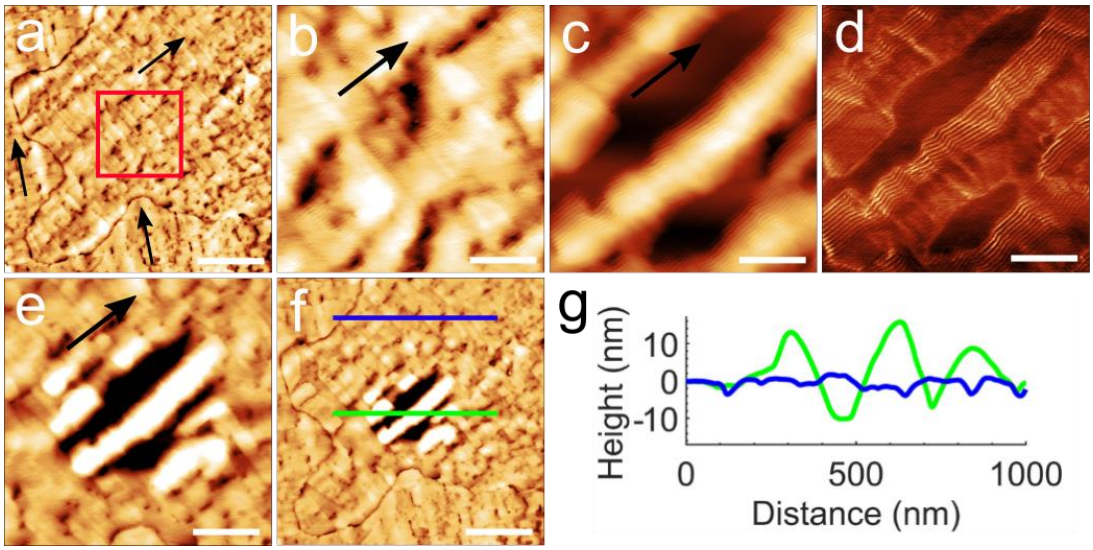

Figure 7.6: Molecules appear piled up after a series of 500×500 nm^2 scans were performed on a sample covered with >30ML. All images correspond to topographic channel except phase channel image in (d). Lamellar orientations are marked with black arrows. a) Large scan image showing a domain covering most of the area. The series of scans were taken from the area marked with a red square. b) First image of the series. c) Last image of the series. The relieve is considerably different. The molecules have piled-up forming trenches. e) Larger size scan shows the trace of the scan forming a square. f) Scan of the same area as (a) after the series of scans were performed. g) Profiles comparing the roughness between the closely scanned area and a neighbouring one. Their paths are indicated in the same colours in (f). Scale bars: a and f) 400 nm, b-d) 100 nm, e) 200 nm.

Another example of recrystalization is shown in Fig 7.7. A sample with 2.5ML hexacontane growth with three different orientational domains can be distinguished: One small domain in the centre of the image surrounded by other bigger two domains (Fig 7.7b extracted from blue square in Fig 7.7a). Figure 7.7c shows the same area after a few scans were performed. The domain at the bottom of the image has merged with the central one, namely, the molecules in this central domain are now oriented in the same way as the ones in the bottom domain. Also, the frontier between the larger

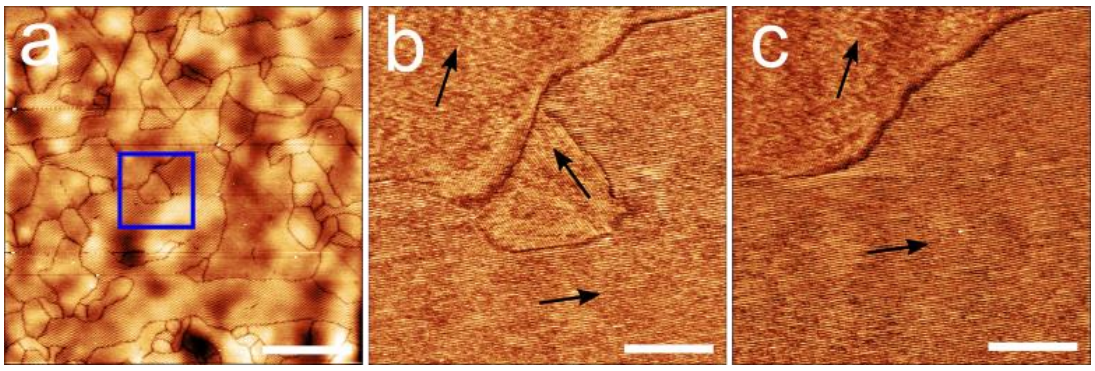

Figure 7.7: a) Large area scan of a 2.5ML hexacontane growth sample. Blue square indicates scan area of (b). b) A small rotational domain surrounded by other two domains. Arrows indicate the lamellar orientations of the three domains. c) Image of the same area after a series of scans have taken place. The domain in the centre of the image has been taken over by the one around its bottom side. Scale bars: (a) 1 µm, (b-c) 200 nm.

domains has been slightly displaced. These images prove that hexacontane molecules in a domain have the capacity to switch orientation and merge with those in their neighbouring domains when stimulated by an AFM tip.

7.7 Summary

Lamellar rows of alkanes are formed on hBN with an internal structure very similar to that observed on a graphite substrate, as confirmed by AFM and molecular mechanics simulations, and in agreement with previous diffraction studies. The molecules can be deposited either by sublimation or from solution. At higher coverage, the period of the lamellar rows persists and is readily resolved on the surface of multilayers, although some disorder is also evident, for example, in the form of meandering lamellar rows. This implies that growth of the subsequent layers is directed by the substrate.

We have also investigated the effect of postdeposition annealing on the sample morphology and AFM tip induced re-crystallization including the formation of hills by piling up molecules or reorientation of molecules in a domain.

8. Conclusions

The growth of graphene discussed in chapters 4,5 and 6 demonstrate that high temperature-MBE is a viable approach to the growth of high-quality epitaxial graphene on hBN by using three different carbon sources: a carbon filament source, an atomic carbon source and an e-beam source.

The large Moiré patterns observed with AFM and the red-shifted Raman peaks clearly demonstrate the possibility of introducing strain on graphene. Moreover, at the highest substrate temperatures, the magnitude of the strain can be large enough to allow graphene to lattice match to hBN. Under such conditions, the difference in chemical environment between the two atoms in the graphene unit cell, provided by the hBN substrate, allows the opening of a small bandgap. Conductive AFM measurements

performed using these lattice matched graphene layers show evidence of this induced bandgap.

High resolution AFM images show that the Frenkel-Kontorova walls between lattice matching graphene run along principal axis and contain an extra row of carbon atoms which terminate at defects.

A series of secondary phenomena such as additional layers, coalesced rotated domains or islands with different morphologies depending on the type of source used are also described.

The electronic properties of this material are yet to be measured. In particular, it is desirable to perform transport measurements on lattice matched graphene. Nevertheless, transferring graphene/hBN onto an insulating substrate such as SiO_2 is a complex process which involves the use of adhesive tape and its associated contamination. Also, highly strained graphene is a delicate material which can crack and relax during the transfer process. Therefore, a reliable method that allows transferring of these heterostructures need further investigation.

The deposition of hexacontane on hBN discussed in chapter 7 shows lamellar rows similar to those observed on graphite. High resolution images and molecular simulations indicate that the molecules are oriented in parallel to the zig-zag direction with their molecular axis parallel to the surface.

The hexacontane monolayer provides a very simple example of two-dimensional supramolecular organization. Our results therefore strongly suggest that chain−chain interactions can direct the formation of self-assembled molecular arrays on hBN in a manner analogous to the highly successful approach to supramolecular organization of complex structures on graphite.

The possible use of hBN raises the possibility of exploring optical properties of such structures that are difficult to access on conducting surfaces, and we believe that this combination of an insulating substrate and van der Waals mediated molecular organization represents a promising route for the future investigation of the science and technology of surface-stabilized supramolecular arrays.

9. References

1. Novoselov, K. S. *et al.* Electric Field Effect in Atomically Thin Carbon Films. *Science (80-.).* **306**, 666–669 (2004).
2. Castro Neto, A. H., Guinea, F., Peres, N. M. R., Novoselov, K. S. & Geim, A. K. The electronic properties of graphene. *Rev. Mod. Phys.* **81**, 109–162 (2009).
3. Novoselov, K. S. *et al.* A roadmap for graphene. *Nature* **490**, 192–200 (2012).
4. Novoselov, K. S. *et al.* Room-Temperature Quantum Hall Effect in Graphene. *Science (80-.).* **315**, 1379–1379 (2007).
5. Zhang, Y., Tan, Y.-W., Stormer, H. L. & Kim, P. Experimental observation of the quantum Hall effect and Berry's phase in graphene. *Nature* **438**, 201–204 (2005).
6. Katsnelson, M. I., Novoselov, K. S. & Geim, A. K. Chiral tunnelling and the Klein paradox in graphene. *Nat. Phys.* **2**, 620–625 (2006).
7. Schedin, F. *et al.* Detection of individual gas molecules adsorbed on graphene. *Nat. Mater.* **6**, 652–655 (2007).
8. Yuan, W. & Shi, G. Graphene-based gas sensors. *J. Mater. Chem. A* **1**, 10078 (2013).
9. Nagashima, A., Tejima, N. & Oshima, C. Electronic states of the pristine and alkali-metal-intercalated monolayer graphite/Ni(111) systems. *Phys. Rev. B* **50**, 17487–17495 (1994).
10. Geim, A. K. & Grigorieva, I. V. Van der Waals heterostructures. *Nature* **499**, 419–25 (2013).
11. Landau, L. D. Zur Theorie der phasenumwandlungen II. *Phys. Z. Sowjetunion* **11**, 26–35 (1937).
12. R. E. Peierls. Quelques proprietes typiques des corpses solides. *Ann. l'Institut Henri Poincaré* **5,** 177–222 (1935).
13. Shams, S. S., Zhang, R. & Zhu, J. Graphene synthesis: A Review. *Mater. Sci. Pol.* **33**, 566–578 (2015).
14. Kairi, M. I. *et al.* Toward high production of graphene flakes-a review on recent developments in their synthesis methods and scalability. *J. Mater. Chem. A* **6**, 15010–15026 (2018).
15. Blake, P. *et al.* Making graphene visible. *Appl. Phys. Lett.* **91**, (2007).
16. Chen, J., Duan, M. & Chen, G. Continuous mechanical exfoliation of graphene sheets via three-roll mill. *J. Mater. Chem.* **22**, 19625 (2012).
17. Knieke, C. *et al.* Scalable production of graphene sheets by mechanical delamination. *Carbon N. Y.* **48**, 3196–3204 (2010).
18. Zhao, W. *et al.* Preparation of graphene by exfoliation of graphite using wet ball milling. *J. Mater. Chem.* **20**, 5817 (2010).
19. Parvez, K. *et al.* Electrochemically Exfoliated Graphene as Solution-Processable, Highly Conductive Electrodes for Organic Electronics. *ACS Nano* **7**, 3598–3606 (2013).
20. Hummers, W. S. & Offeman, R. E. Preparation of Graphitic Oxide. *J. Am. Chem. Soc.* **80**, 1339–1339 (1958).
21. He, H., Riedl, T., Lerf, A. & Klinowski, J. Solid-State NMR Studies of the Structure of Graphite Oxide. *J. Phys. Chem.* **100**, 19954–19958 (1996).
22. Park, S. & Ruoff, R. S. Chemical methods for the production of graphenes. *Nat. Nanotechnol.* **4**, 217–224 (2009).

23. Chua, C. K. & Pumera, M. Chemical reduction of graphene oxide: a synthetic chemistry viewpoint. *Chem. Soc. Rev.* **43**, 291–312 (2014).
24. Mattevi, C. *et al.* Evolution of Electrical, Chemical, and Structural Properties of Transparent and Conducting Chemically Derived Graphene Thin Films. *Adv. Funct. Mater.* **19**, 2577–2583 (2009).
25. Riedl, C., Coletti, C. & Starke, U. Structural and electronic properties of epitaxial graphene on SiC(0 0 0 1): a review of growth, characterization, transfer doping and hydrogen intercalation. *J. Phys. D. Appl. Phys.* **43**, 374009 (2010).
26. Riedl, C., Zakharov, A. A. & Starke, U. Precise in situ thickness analysis of epitaxial graphene layers on SiC(0001) using low-energy electron diffraction and angle resolved ultraviolet photoelectron spectroscopy. *Appl. Phys. Lett.* **93**, 033106 (2008).
27. Riedl, C., Starke, U., Bernhardt, J., Franke, M. & Heinz, K. Structural properties of the graphene-SiC(0001) interface as a key for the preparation of homogeneous large-terrace graphene surfaces. *Phys. Rev. B* **76**, 245406 (2007).
28. Ohta, T., Bostwick, A., Seyller, T., Horn, K. & Rotenberg, E. Controlling the Electronic Structure of Bilayer Graphene. *Science (80-.).* **313**, 951–954 (2006).
29. Riedl, C., Zakharov, A. A. & Starke, U. Precise in situ thickness analysis of epitaxial graphene layers on SiC(0001) using low-energy electron diffraction and angle resolved ultraviolet photoelectron spectroscopy. *Appl. Phys. Lett.* **93**, 033106 (2008).
30. Riedl, C., Coletti, C., Iwasaki, T., Zakharov, A. A. & Starke, U. Quasi-Free-Standing Epitaxial Graphene on SiC Obtained by Hydrogen Intercalation. *Phys. Rev. Lett.* **103**, 246804 (2009).
31. Riedl, C., Coletti, C., Iwasaki, T., Zakharov, A. A. & Starke, U. Quasi-free-standing epitaxial graphene on SiC obtained by hydrogen intercalation. *Phys. Rev. Lett.* **103**, 1–4 (2009).
32. Amini, S., Garay, J., Liu, G., Balandin, A. A. & Abbaschian, R. Growth of large-area graphene films from metal-carbon melts. *J. Appl. Phys.* **108**, 094321 (2010).
33. Yan, P., Jeong, Y. J., Islam, M. F. & Pistorius, P. C. Real time and in situ observation of graphene growth on liquid metal surfaces via a carbon segregation method using high-temperature confocal laser scanning microscopy. *RSC Adv.* **6**, 101235–101241 (2016).
34. Qingkai Yu *et al.* Graphene segregated on Ni surfaces and transferred to insulators. *Appl. Phys. Lett.* **93**, 113103 (2008).
35. Reina, A. *et al.* Large Area, Few-Layer Graphene Films on Arbitrary Substrates by Chemical Vapor Deposition. *Nano Lett.* **9**, 30–35 (2009).
36. Kim, K. S. *et al.* Large-scale pattern growth of graphene films for stretchable transparent electrodes. *Nature* **457**, 706–710 (2009).
37. Li, X. *et al.* Large-Area Synthesis of High-Quality and Uniform Graphene Films on Copper Foils. *Science (80-.).* **324**, 1312–1314 (2009).
38. De Arco, L. G., Yi Zhang, Kumar, A. & Chongwu Zhou. Synthesis, Transfer, and Devices of Single- and Few-Layer Graphene by Chemical Vapor Deposition. *IEEE Trans. Nanotechnol.* **8**, 135–138 (2009).
39. Sutter, P. W., Flege, J. I. & Sutter, E. A. Epitaxial graphene on ruthenium. *Nat. Mater.* **7**, 406–411 (2008).
40. Sutter, P., Sadowski, J. T. & Sutter, E. Graphene on Pt(111): Growth and substrate interaction. *Phys. Rev. B* **80**, 245411 (2009).
41. Coraux, J., N'Diaye, A. T., Busse, C. & Michely, T. Structural Coherency of

Graphene on Ir(111). *Nano Lett.* **8**, 565–570 (2008).
42. Varykhalov, A. & Rader, O. Graphene grown on Co(0001) films and islands: Electronic structure and its precise magnetization dependence. *Phys. Rev. B* **80**, 035437 (2009).
43. Kwon, S.-Y. *et al.* Growth of Semiconducting Graphene on Palladium. *Nano Lett.* **9**, 3985–3990 (2009).
44. Wintterlin, J. & Bocquet, M. L. Graphene on metal surfaces. *Surf. Sci.* **603**, 1841–1852 (2009).
45. Lee, C., Wei, X., Kysar, J. W. & Hone, J. Measurement of the Elastic Properties and Intrinsic Strength of Monolayer Graphene. *Science (80-.).* **321**, 385–388 (2008).
46. Wallace, P. R. The Band Theory of Graphite. *Phys. Rev.* **71**, 622–634 (1947).
47. Varlet, A. *et al.* Band gap and broken chirality in single-layer and bilayer graphene. *Phys. status solidi - Rapid Res. Lett.* **10**, 46–57 (2016).
48. Watanabe, K., Taniguchi, T. & Kanda, H. Direct-bandgap properties and evidence for ultraviolet lasing of hexagonal boron nitride single crystal. *Nat. Mater.* **3**, 404–409 (2004).
49. Liu, L., Feng, Y. P. & Shen, Z. X. Structural and electronic properties of h -BN. *Phys. Rev. B* **68**, 104102 (2003).
50. Dean, C. R. *et al.* Boron nitride substrates for high-quality graphene electronics. *Nat. Nanotechnol.* **5**, 722–6 (2010).
51. Xue, J. *et al.* Scanning tunnelling microscopy and spectroscopy of ultra-flat graphene on hexagonal boron nitride. *Nat. Mater.* **10**, 282–285 (2011).
52. Decker, R. *et al.* Local electronic properties of graphene on a BN substrate via scanning tunneling microscopy. *Nano Lett.* **11**, 2291–2295 (2011).
53. Sichel, E. K., Miller, R. E., Abrahams, M. S. & Buiocchi, C. J. Heat capacity and thermal conductivity of hexagonal pyrolytic boron nitride. *Phys. Rev. B* **13**, 4607–4611 (1976).
54. Laturia, A., Van de Put, M. L. & Vandenberghe, W. G. Dielectric properties of hexagonal boron nitride and transition metal dichalcogenides: from monolayer to bulk. *npj 2D Mater. Appl.* **2**, 6 (2018).
55. Novoselov, K. S. *et al.* Two-dimensional gas of massless Dirac fermions in graphene. *Nature* **438**, 197–200 (2005).
56. Yankowitz, M. *et al.* Emergence of superlattice Dirac points in graphene on hexagonal boron nitride. *Nat. Phys.* **8**, 382–386 (2012).
57. Kuwabara, M., Clarke, D. R. & Smith, D. A. Anomalous superperiodicity in scanning tunneling microscope images of graphite. *Appl. Phys. Lett.* **56**, 2396–2398 (1990).
58. Huang, L. *et al.* Effects of moiré lattice structure on electronic properties of graphene. *Phys. Rev. B* **96**, 035411 (2017).
59. Meng, L. *et al.* Multi-oriented moiré superstructures of graphene on Ir(111): Experimental observations and theoretical models. *J. Phys. Condens. Matter* **24**, (2012).
60. Pan, Y. *et al.* Highly Ordered, Millimeter-Scale, Continuous, Single-Crystalline Graphene Monolayer Formed on Ru (0001). *Adv. Mater.* **21**, n/a-n/a (2009).
61. Hofstadter, D. R. Energy levels and wave functions of Bloch electrons in rational and irrational magnetic fields. *Phys. Rev. B* **14**, 2239–2249 (1976).
62. Dean, C. R. *et al.* Hofstadter's butterfly and the fractal quantum Hall effect in moiré superlattices. *Nature* **497**, 598–602 (2013).
63. Woods, C. R. *et al.* Commensurate-incommensurate transition in graphene on

hexagonal boron nitride. *Nat. Phys.* **10**, 451–456 (2014).
64. Summerfield, A. *et al.* Strain-Engineered Graphene Grown on Hexagonal Boron Nitride by Molecular Beam Epitaxy. *Sci. Rep.* **6**, 1–10 (2016).
65. Linas, S. *et al.* Interplay between Raman shift and thermal expansion in graphene: Temperature-dependent measurements and analysis of substrate corrections. *Phys. Rev. B - Condens. Matter Mater. Phys.* **91**, 1–5 (2015).
66. Yates, B., Overy, M. J. & Pirgon, O. The anisotropic thermal expansion of boron nitride. *Philos. Mag.* **32**, 847–857 (1975).
67. Ferralis, N., Maboudian, R. & Carraro, C. Evidence of structural strain in epitaxial graphene layers on 6H-SiC(0001). *Phys. Rev. Lett.* **101**, 1–4 (2008).
68. Guinea, F., Katsnelson, M. I. & Geim, A. K. Energy gaps and a zero-field quantum hall effect in graphene by strain engineering. *Nat. Phys.* **6**, 30–33 (2010).
69. San-Jose, P., Gutiérrez-Rubio, A., Sturla, M. & Guinea, F. Spontaneous strains and gap in graphene on boron nitride. *Phys. Rev. B - Condens. Matter Mater. Phys.* **90**, 1–8 (2014).
70. Neek-Amal, M. & Peeters, F. M. Graphene on hexagonal lattice substrate: Stress and pseudo-magnetic field. *Appl. Phys. Lett.* **104**, (2014).
71. Giovannetti, G., Khomyakov, P. A., Brocks, G., Kelly, P. J. & Van Den Brink, J. Substrate-induced band gap in graphene on hexagonal boron nitride: Ab initio density functional calculations. *Phys. Rev. B - Condens. Matter Mater. Phys.* **76**, 2–5 (2007).
72. Zhou, S. Y. *et al.* Substrate-induced bandgap opening in epitaxial graphene. *Nat. Mater.* **6**, 770–775 (2007).
73. Nevius, M. S. *et al.* Semiconducting Graphene from Highly Ordered Substrate Interactions. *Phys. Rev. Lett.* **115**, 1–5 (2015).
74. Suk, J. W. *et al.* Transfer of CVD-grown monolayer graphene onto arbitrary substrates. *ACS Nano* **5**, 6916–6924 (2011).
75. Tang, S. *et al.* Precisely aligned graphene grown on hexagonal boron nitride by catalyst free chemical vapor deposition. *Sci. Rep.* **3**, 1–7 (2013).
76. Tang, S. *et al.* Silane-catalysed fast growth of large single-crystalline graphene on hexagonal boron nitride. *Nat. Commun.* **6**, 6499 (2015).
77. Yang, W. *et al.* Epitaxial growth of single-domain graphene on hexagonal boron nitride. *Nat. Mater.* **12**, 792–797 (2013).
78. Cho, A. Y. Film Deposition by Molecular-Beam Techniques. *J. Vac. Sci. Technol.* **8**, S31–S38 (2002).
79. Dabrowski, J., Lippert, G., Schroeder, T. & Lupina, G. Role of defects in the process of graphene growth on hexagonal boron nitride from atomic carbon. *Appl. Phys. Lett.* **105**, (2014).
80. Garcia, J. M. *et al.* Graphene growth on h-BN by molecular beam epitaxy. *Solid State Commun.* **152**, 975–978 (2012).
81. Ferrari, A. C. *et al.* Raman Spectrum of Graphene and Graphene Layers. *Phys. Rev. Lett.* **97**, 187401 (2006).
82. Wang, Y. ying *et al.* Raman Studies of Monolayer Graphene: The Substrate Effect. *J. Phys. Chem. C* **112**, 10637–10640 (2008).
83. Mohiuddin, T. M. G. *et al.* Uniaxial strain in graphene by Raman spectroscopy: G peak splitting, Grüneisen parameters, and sample orientation. *Phys. Rev. B - Condens. Matter Mater. Phys.* **79**, 1–8 (2009).
84. Shin, Y. *et al.* Raman spectroscopy of highly pressurized graphene membranes. *Appl. Phys. Lett.* **108**, 1–5 (2016).

85. Piscanec, S., Lazzeri, M., Mauri, F., Ferrari, A. C. & Robertson, J. Kohn Anomalies and Electron-Phonon Interactions in Graphite. *Phys. Rev. Lett.* **93**, 185503 (2004).
86. Malard, L. M., Pimenta, M. A., Dresselhaus, G. & Dresselhaus, M. S. Raman spectroscopy in graphene. *Phys. Rep.* **473**, 51–87 (2009).
87. Yoon, D., Son, Y.-W. & Cheong, H. Strain-Dependent Splitting of the Double-Resonance Raman Scattering Band in Graphene. *Phys. Rev. Lett.* **106**, 155502 (2011).
88. Huang, M., Yan, H., Heinz, T. F. & Hone, J. Probing Strain-Induced Electronic Structure Change in Graphene by Raman Spectroscopy. *Nano Lett.* **10**, 4074–4079 (2010).
89. Everett, D. H. & Findenegg, G. H. Calorimetric evidence for the structure of films adsorbed at the solid/liquid interface: The heats of wetting of 'Graphon' by some n-Alkanes. *Nature* **223**, 52–53 (1969).
90. Groszek, A. J. Selective Adsorption at Graphite/Hydrocarbon Interfaces. *Proc. R. Soc. A Math. Phys. Eng. Sci.* **314**, 473–498 (1970).
91. McGonigal, G. C., Bernhardt, R. H. & Thomson, D. J. Imaging alkane layers at the liquid/graphite interface with the scanning tunneling microscope. *Appl. Phys. Lett.* **57**, 28–30 (1990).
92. Abrahamsson, S., Larsson, G. & von Sydow, E. The crystal structure of the monoclinic form of n -hexadecanol. *Acta Crystallogr.* **13**, 770–774 (1960).
93. Rabe, J. P. & Buchholz, S. Commensurability and mobility in two-dimensional molecular patterns on graphite. *Science (80-.).* **253**, 424–427 (1991).
94. Flynn, G. W., Berne, B. J., Florio, G. M., Ilan, B. & Hybertsen, M. S. Scanning Tunneling Microscopy Images of Alkane Derivatives on Graphite: Role of Electronic Effects. *Nano Lett.* **8**, 3160–3165 (2008).
95. Liang, W., Whangbo, M.-H., Wawkuschewski, A., Cantow, H.-J. & Magonov, S. N. Electronic origin of scanning tunneling microscopy images and carbon skeleton orientations of normal alkanes adsorbed on graphite. *Adv. Mater.* **5**, 817–821 (1993).
96. Faglioni, F., Claypool, C. L., Lewis, N. S. & Goddard, W. A. Theoretical Description of the STM Images of Alkanes and Substituted Alkanes Adsorbed on Graphite. *J. Phys. Chem. B* **101**, 5996–6020 (2002).
97. Yang, T., Berber, S., Liu, J. F., Miller, G. P. & Tománek, D. Self-assembly of long chain alkanes and their derivatives on graphite. *J. Chem. Phys.* **128**, (2008).
98. Krishnan, M., Balasubramanian, S. & Clarke, S. Structure of solid monolayers and multilayers ofn-hexane on graphite. *J. Chem. Sci.* **115**, 663–677 (2007).
99. Yin, S., Wang, C., Qiu, X., Bo, X. & Bai, C. Theoretical study of the effects of intermolecular interactions in self-assembled long-chain alkanes adsorbed on graphite surface. *Surf. Interface Anal.* **32**, 248–252 (2001).
100. Tománek, D. *et al.* Theory and observation of highly asymmetric atomic structure in scanning-tunneling-microscopy images of graphite. *Phys. Rev. B* **35**, 7790–7793 (1987).
101. Hibino, M. Adsorption Behaviors of Mixed Monolayers of n -Alkanes at the Liquid–Solid Interface. *Langmuir* **32**, 4705–4709 (2016).
102. Xie, Z. X., Xu, X., Mao, B. W. & Tanaka, K. Self-Assembled Binary Monolayers of n -Alkanes on Reconstructed Au(111) and HOPG Surfaces. *Langmuir* **18**, 3113–3116 (2002).
103. Castro, M. A., Clarke, S. M., Inaba, A., Thomas, R. K. & Arnold, T. Preferential Adsorption from Binary Mixtures of Short Chain n -Alkanes; The

Octane−Decane System. *J. Phys. Chem. B* **105**, 8577–8582 (2001).
104. Alba, M. D. *et al.* Preferential Adsorption from Binary Mixtures on Graphite: The n -Decane− n -Heptan-1-ol System. *J. Phys. Chem. C* **113**, 3176–3180 (2009).
105. Masnadi, M. & Urquhart, S. G. Effect of substrate temperature on the epitaxial growth of oriented n-alkane thin films on graphite. *Langmuir* **28**, 12493–12501 (2012).
106. Gosvami, N. N. & O'Shea, S. J. Nanoscale Trapping and Squeeze-Out of Confined Alkane Monolayers. *Langmuir* **31**, 12960–12967 (2015).
107. Magonov, S. N. & Yerina, N. A. High-temperature atomic force microscopy of normal alkane C60H122 films on graphite. *Langmuir* **19**, 500–504 (2003).
108. Taniguchi, T. & Watanabe, K. Synthesis of high-purity boron nitride single crystals under high pressure by using Ba-BN solvent. *J. Cryst. Growth* **303**, 525–529 (2007).
109. Cheng, T. S. *et al.* High temperature MBE of graphene on sapphire and hexagonal boron nitride flakes on sapphire. *J. Vac. Sci. Technol. B, Nanotechnol. Microelectron. Mater. Process. Meas. Phenom.* **34**, 02L101 (2016).
110. Binnig, G., Rohrer, H., Gerber, C. & Weibel, E. Surface Studies by Scanning Tunneling Microscopy. *Phys. Rev. Lett.* **49**, 57–61 (1982).
111. Binnig, G., Rohrer, H., Gerber, C. & Weibel, E. 7 × 7 Reconstruction on Si(111) Resolved in Real Space. *Phys. Rev. Lett.* **50**, 120–123 (1983).
112. Bardeen, J. Tunnelling from a Many-Particle Point of View. *Phys. Rev. Lett.* **6**, 57–59 (1961).
113. Tersoff, J. & Hamann, D. R. Theory of the scanning tunneling microscope. *Phys. Rev. B* **31**, 805–813 (1985).
114. Binnig, G., Quate, C. F. & Gerber, C. Atomic Force Microscope. *Phys. Rev. Lett.* **56**, 930–933 (1986).
115. Krasnokutski, S. A. & Huisken, F. A simple and clean source of low-energy atomic carbon. *Appl. Phys. Lett.* **105**, (2014).
116. Cosma, D. A., Wallbank, J. R., Cheianov, V. & Falko, V. I. Moiré pattern as a magnifying glass for strain and dislocations in van der Waals heterostructures. *Faraday Discuss.* **173**, 137–143 (2014).
117. Sattler, J. J. H. B., Ruiz-Martinez, J., Santillan-Jimenez, E. & Weckhuysen, B. M. Catalytic Dehydrogenation of Light Alkanes on Metals and Metal Oxides. *Chem. Rev.* **114**, 10613–10653 (2014).
118. Morikawa, Y., Ishii, H. & Seki, K. Theoretical study of n -alkane adsorption on metal surfaces. *Phys. Rev. B* **69**, 041403 (2004).
119. Weaver, J. The adsorption and reaction of low molecular weight alkanes on metallic single crystal surfaces. *Surf. Sci. Rep.* **50**, 107–199 (2003).
120. Cyr, D. M., Venkataraman, B. & Flynn, G. W. STM Investigations of Organic Molecules Physisorbed at the Liquid−Solid Interface. *Chem. Mater.* **8**, 1600–1615 (1996).
121. Arnold, T., Forster, M., Athanasiou Fragkoulis, A. & Parker, J. E. Structure of normal-alkanes adsorbed on hexagonal-boron nitride. *J. Phys. Chem. C* **118**, 2418–2428 (2014).
122. Forster, M. *et al.* The Mixing Behavior of Alkanes Adsorbed on Hexagonal Boron Nitride. *J. Phys. Chem. C* **120**, 25796–25805 (2016).
123. Korolkov, V. V. *et al.* Supramolecular networks stabilise and functionalise black phosphorus. *Nat. Commun.* **8**, 1–8 (2017).

124. Holzwarth, A., Leporatti, S. & Riegler, H. Molecular ordering and domain morphology of molecularly thin triacontane films at SiO 2 /air interfaces. *Europhys. Lett.* **52**, 653–659 (2000).
125. Korolkov, V. V. *et al.* Supramolecular heterostructures formed by sequential epitaxial deposition of two-dimensional hydrogen-bonded arrays. *Nat. Chem.* **9**, 1191–1197 (2017).